Monthly Scientific-Technical and Production Journal

The Paton WELDING JOURNAL

August 2002 # 8

English translation of the monthly «Avtomaticheskaya Svarka» journal published in Russian since 1948

Founders: *The National Academy of Sciences of Ukraine, The E.O. Paton Electric Welding Institute of the NAS of Ukraine, International Association «Welding»*
Publisher: *International Association «Welding»*

Editorial and advertising offices:
E.O. Paton Electric Welding Institute,
International Association «Welding»,
11, Bozhenko str., 03680, Kyiv, Ukraine
Tel.: (38044) 227 67 57
Fax: (38044) 268 04 86
E-mail: journal@paton.kiev.ua
http://www.nas.gov.ua/pwj

State Registration Certificate
KV 4790 of 09.01.2001

Subscriptions:
$460, 12 issues per year,
postage and packaging included.
Back issues available

CONTENTS

COMPUTER PROGRAM «WELDING OF TUBES TO TUBE SHEETS OF HEAT EXCHANGERS»

V.I. MAKHNENKO[1], E.A. VELIKOIVANENKO[1], O.V. MAKHNENKO[1], G.F. ROZYNKA[1], N.I. PIVTORAK[1], P. SEYFFARTH[2] and K. BAUTZMANN[3]
[1]The E.O. Paton Electric Welding Institute, NASU, Kyiv, Ukraine
[2]SLV M/V GmbH
[3]INFRACOR, Germany

The computer program is described, and its capabilities are shown in terms of estimation of both local phenomena related to welding of individual tubes (cooling rate, microstructural changes, residual stresses) and total distortions of the tube sheet depending upon properties of materials, geometric sizes, type of a joint and sequence of welding tubes to the tube sheet.

Key words: *computer program, mathematical modelling, calculation algorithms, electric arc welding, tubes, tube sheet, heat exchanger, data bank, temperature fields, chemical composition, microstructure, TTT diagram, Schaeffler diagram, HAZ, process quality, kinetics of distortions, residual stresses, cold cracks*

Welded assemblies of the type of «tubes to tube sheet» are characteristic of the up-to-date designs of heat exchangers. Tubes and tube sheets are very often made from different steel grades, which leads to certain difficulties in production of a quality joint. There are cases where welding of tubes may involve problems related to distortion of tube sheets. Normally these problems are solved by experimental methods which are costly and time-consuming. This leads to the necessity to use mathematical modelling with modern computer facilities to partially solve the above problems, which allows the scope of expensive experimental studies needed to optimise the technology to be reduced. Cooperation between the E.O. Paton Electric Welding Institute of the HAS of Ukraine, SLV (Mecklenburg) and INFRACOR (Germany) resulted in the development of a computer program based on the calculation algorithms of mathematical modelling of basic physical phenomena which accompany the process of electric arc welding of tubes to a tube sheet, combined with the data bank of main calculated characteristics (thermal-physical properties, characteristics of microstructural transformations, mechanical properties) for typical materials of tubes and tube sheets used in heat exchangers. This article is dedicated to brief description of this program and demonstration of its capabilities.

Table 1. Designations of steels the calculation characteristics of which are contained in the data bank

Tube sheet and tube materials according to EN (national analogues)	*Filler material according to DIN 8557 (national analogues)*
10CrMo9-10 (14Kh3M)	SG2 (09G2)
11CrMo9-10 (15Kh3M)	SCMo (09GM)
13CrMo4-5 (18KhM)	SGCrMo1 (10KhGM)
16Mo3 (St.20 with 0.3 % Mo)	SGCrMo2 (10KhGM2)
P235GH (16GFT)	SG-X5CrNiMoNb 19 12 (08Kh19N12M)
P235G2TH (16G2FT)	SG-X5CrNiNb 19 9 (08Kh18N10T)
P265GH (20GFT)	SG-X15CrNiMn 18 8 (15Kh20N9G6)
P295GH (20G2FT)	FLUXOFIL M 8 (06GS)
P355GH (20G2FT)	FLUXOFIL M 10 (06GS)
X2CrNiMoN22-5-3 (08Kh22N5M3)	
X5CrNi18-10 (08Kh18N10T)	
X6CrNiMoTi17-12-2 (10Kh17N12M2T)	
X6CrNiTi18-10 (08Kh18N10T)	

Brief description of the computer program. The friendly interface allows on-line utilisation of the program by technology developers, avoiding the search for additional data outside the scope of the technological information.

Figure 1 shows picture of the screen to enter the source data, including the material selected, geometric sizes, conditions and parameters of welding. By assigning materials, the user may read the list of materials designations from the data bank, as well as see the specific contents of the information on a given material (Tables 1 and 2). To select geometric parameters of a welded joint, it is necessary to preliminarily choose the type of a joint (one out of five shown in Figure 2) and set geometric sizes a and x. The user sets the basic design geometric sizes (Figure 1), including coordinates of position of tube centres on the tube sheet.

A special subprogram is available to perform the last operation. Using this subprogram, the computer first automatically locates tubes according to the preset pitch, t = const, between the tube centres, and then the user makes certain corrections based on a

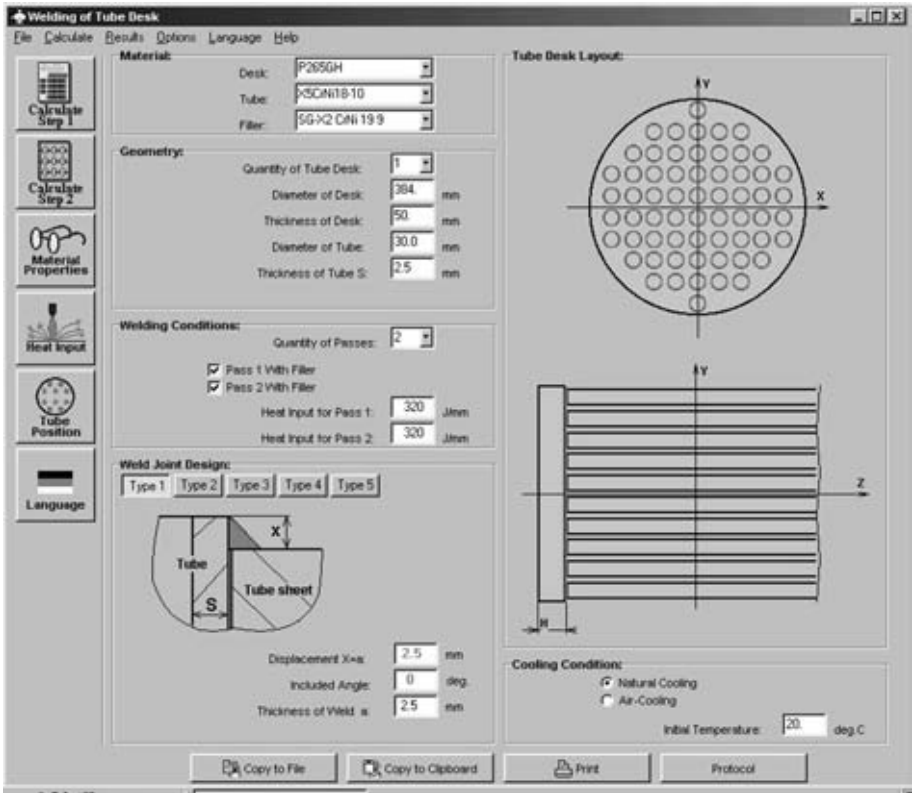

Figure 1. Picture of the screen to enter source data

drawing. If necessary, the user can solve some specific problems using the «help» function. At the user's option, the program can work in one of the three languages: Russian, English or German.

Two characteristic types of a heat exchanger are provided for: with one tube sheet, when the tube inlet and outlet are located in one sheet, and with two tube sheets and straight tubes, allowing for the fact that welding of the ends of all the tubes is performed simultaneously. The ends are welded to the tube sheet by the TIG method (with or without filler metal) at a pulsed welding current. Parameters of the current pulsation, as well as the welding head rotation speed, are set from the source data.

Temperature fields are calculated for such a welding [1, 2]. Size and shape of the zone of penetration of the tube, tube sheet and previous layer (in two-layer welding) are defined. Average chemical composition of the molten zone is estimated from these data, this serving as the basis for further calculations of its microstructural state. The latter is calculated using the Schaeffler diagram for high-alloy steel, or the TTT diagrams for low-alloy ferritic steels [3, 4]. The TTT diagrams are used also for the HAZ of the tube sheet. Corresponding characteristics for parametric equations, relating the amount of an expected phase in microstructure to cooling time $t_{8/5}$ within a range of 800–500 °C can be taken from the data bank (Table 2). Temperature T^j_b and T^j_e, determining the beginning and end of formation of a corresponding phase in the j-microstructure at $t_{8/5}$ characteristic of this welding process (low heat input) can also be taken from the data bank. Knowledge of the temperature fields and volumetric changes related to temperature expansion and microstructural transformations allows evolution of plastic strains to be traced up to reaching a residual state [5].

The value and distribution of residual stresses, combined with the data on microstructural state of the weld and HAZ, are characteristics of the quality of a technological process in terms, e.g., of cold (hydrogen) cracking.

In addition, the local data on curvature of the tube sheet are then used in an approximate method of the «shrinkage function» (inherent strain method) [6, 7] to generate data on the kinetics of bending strains of the tube sheet induced by successive welding of all the tubes.

Application examples. Consider some examples of application of the program described for generation

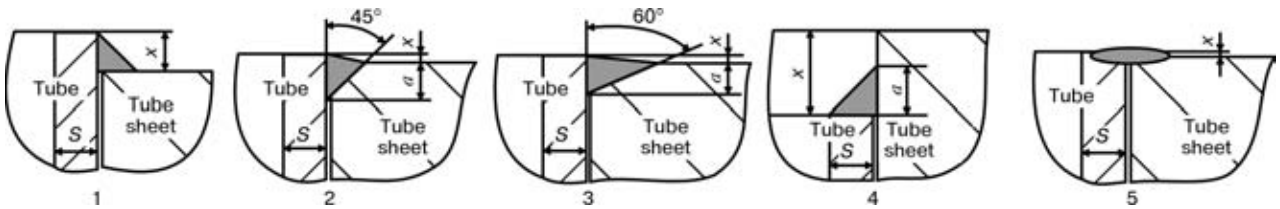

Figure 2. Types of geometry of tube to tube sheet combinations provided for in the program

Table 2. Print out of the data bank information on calculation characteristics of steel P265GH

Type of steel (1 — austenitic, 2 — ferritic-pearlitic)
2

P265GH

Yield stress σ_y (20 °C), MPa, at 20 °C, depending upon thickness D:

D_{min}, mm	D_{max}, mm	σ_y (20 °C), MPa
0	16	265
16	40	255
40	60	245
60	100	215
100	150	200

T, °C	E, MPa	$\frac{\sigma_y(T)}{\sigma_y(20\ °C)}$	α, 1/°C	λ, J/cm·s·°C	$c\gamma_3$, J/cm^3·°C
20	198000	1.000	.0000122	.515	3.79
100	184000	.918	.0000130	.510	3.85
200	176000	.867	.0000144	.485	4.12
300	167000	.836	.0000158	.444	4.41
400	158000	.775	.0000168	.427	4.77
500	134000	.704	.0000168	.393	5.32
600	115000	.551	.0000163	.356	6.01
700	105000	.285	.0000158	.319	6.59
800	92000	.132	.0000158	.259	6.57
900	70000	–	–	–	5.06
1000	52000	–	–	–	5.06
1100	24000	–	–	–	5.09
1200	7000	–	–	–	5.26

Chemical composition:

C	Si	Mn	P	S	Al	Cr	Cu	Mo	Nb	Ni	Ti	V
0.2	0.4	1.4	0.03	0.025	0.02	0.3	0.3	0.08	0.01	0.3	0.03	0.02

$T_{liquidus}$ (°C): 1450
$T_{solidus}$ (°C): 1480

Latent melting heat (J/mm^3):
2.10

Martensite		Bainite		Ferrite-pearlite		
T_b	T_e	T_b	T_e	T_b	T_e	(°C)
415	250	650	415	750	650	

dt — time of cooling from 800 to 500 °C, corresponding to 85 % and 50 % transformation to martensite (m) and ferrite-pearlite (fp)

dt (m85)	dt (m50)	dt (fp85)	dt (fp50)	(s)
2	3	250	235	

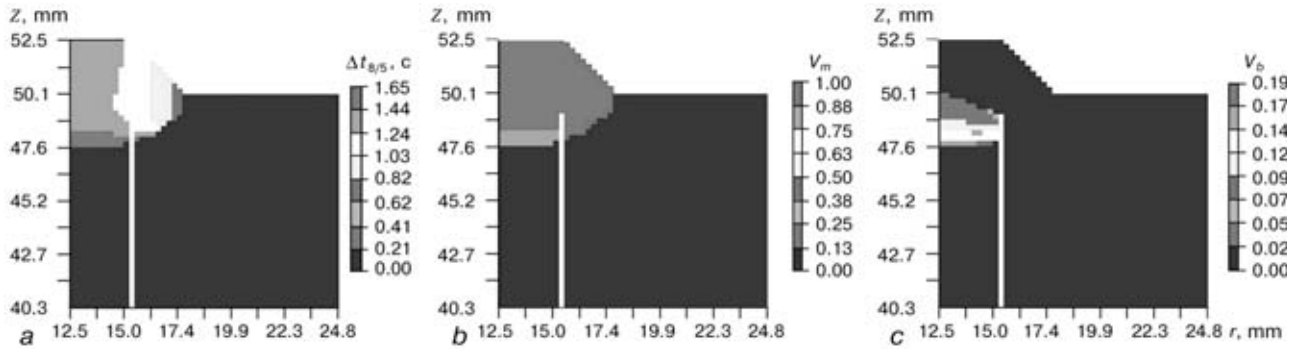

Figure 3. Cooling time $\Delta t_{8/5}$ (*a*) and results of calculation of the martensite (*b*) and bainite (*c*) contents of the weld zone for the joint of type 1 (first series)

Table 3. Chemical composition of materials used in calculations

Material	Content of elements, wt.%												
	C	*Si*	*Mn*	*P*	*S*	*Al*	*Cr*	*Cu*	*Mo*	*Nb*	*Ni*	*Ti*	*V*
P265GH (tube sheet)	0.20	0.40	1.40	0.030	0.025	0.02	0.30	0.30	0.08	0.01	0.30	0.03	0.02
P235G2TH (tubes)	0.17	0.35	0.60	0.040	0.040	–	–	–	–	–	–	–	–
SG2 (filler metal)	0.080	0.85	1.50	0.025	0.025	–	–	–	–	–	–	–	–
X5CrNi18-10 (tubes)	0.060	0.45	1.58	0.023	0.019	–	18.02	–	–	–	9.8	–	–
SG-X2CrNi 19 9 (filler metal)	0.025	0.90	1.70	0.023	0.020	–	–	–	–	–	–	–	–

of the information required for assessment of alternative technologies. Considered was the assembly of a heat exchanger of a tube sheet (see Figure 1) with a diameter of 384 mm, made from ferritic steel P265GH according to EN 10028-2–1992 and having 58 holes for the ends of the tubes with a diameter of 30 mm (wall thickness 2.5 mm). In the first series of calculations the tube material was assumed to be steel P235G2TH according to EN 100281-2. In the second series the tube material was austenitic steel X5CrNi18-10 according to DIN 8556. In the first series material SG2 and in the second — material SGX2CrNi 19 9 were used as the filler metals.

Chemical compositions of the base and filler metals are given in Table 3. Welding was performed in two passes by the TIG method using pulsed current. The mean heat input along the length of the circumferential weld in each pass was $q_h \cong 320$ J/mm. Considered was the variant of the heat exchanger with one tube sheet and different types of the joints (see Figure 2), as well as the variant with two tube sheets and different length of the tubes, L, welded simultaneously from both ends.

Figures 3–5 show results of calculations for the first series of experiments, where the tubes were made

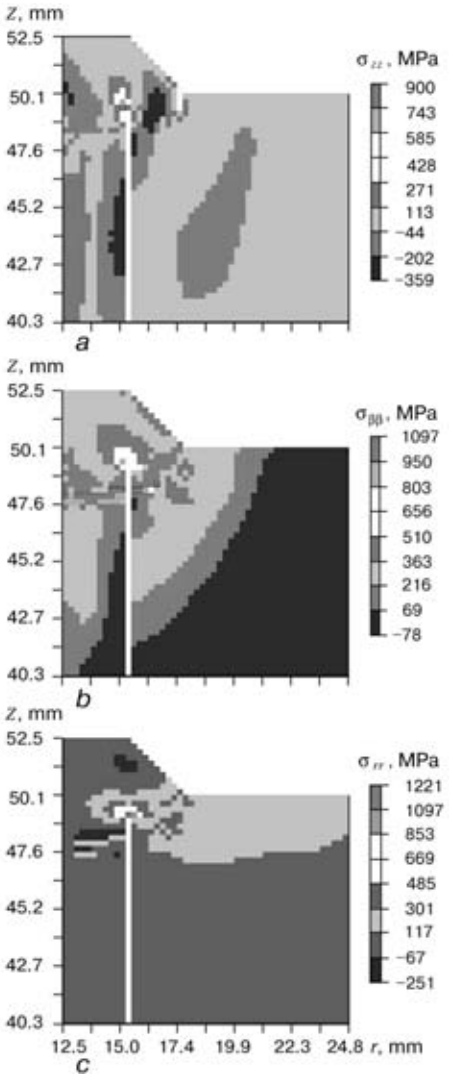

Figure 4. Results of calculations of residual stresses in the weld zone σ_{zz} (*a*), $\sigma_{\beta\beta}$ (*b*) and σ_{rr} (*c*) for the joint of type 1 (first series)

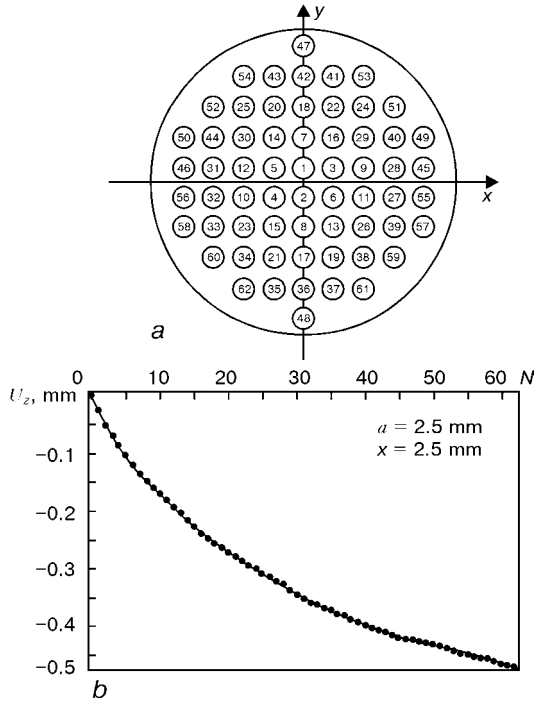

Figure 5. Sequence of welding of tubes (*a*) and kinetics of variation in deflection of the central part of the tube sheet after welding the next tube (*b*) for the joint of type 1 (first series) (N — number of the tube welded)

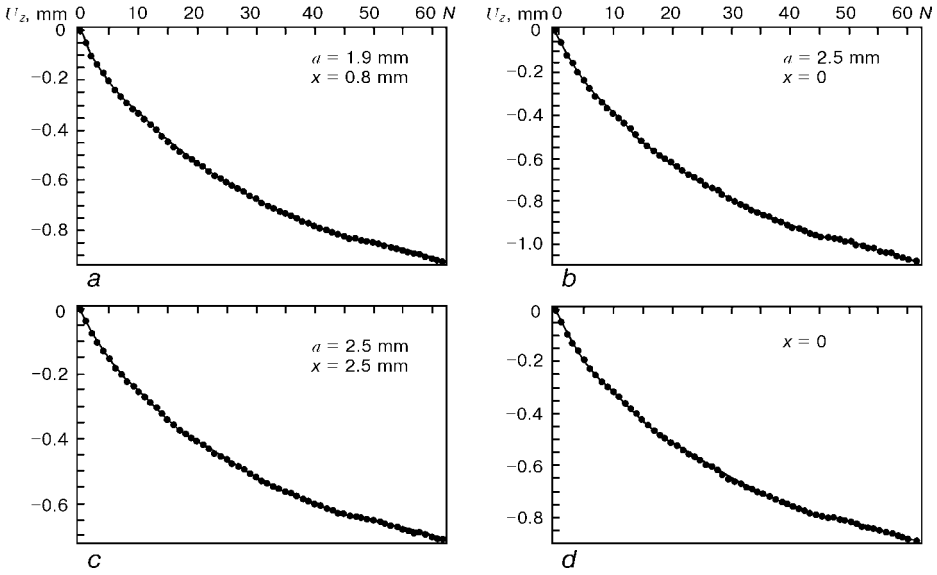

Figure 6. Kinetics of variations in deflection of central part of the tube sheet after welding the next N^{th} tube for joints of types 2–5 (*a–d*), respectively

from ferritic-pearlitic steel P235G2TH and the welded joint corresponded to type 1 in Figure 2. Welding was performed without preheating.

Of note is a large amount of quenching microstructures (martensite) in the weld zone, which was caused by rapid cooling of this zone, $\Delta t_{8/5} \approx 1.5–1.6$ s (Figure 3, *a*) and relatively high carbon and manganese contents.

The presence of hard microstructures in the welded joint zone leads to formation of very high peaks of residual stresses (Figure 4). However, the zones with high residual stresses are rather small in size, they are just small embedments. Such stresses may be favourable for cold cracks, although their length will not be large. Nevertheless, we have to allow for such a risk.

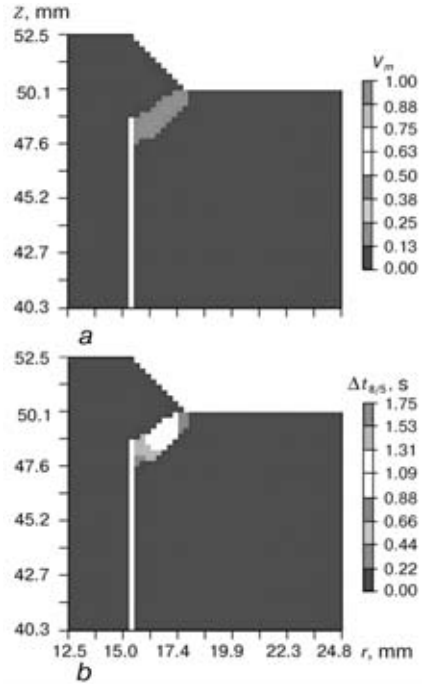

Figure 7. Results of calculations of the martensite content V_m (*a*) and cooling time $\Delta t_{8/5}$ (*b*) for the joint of type 1 (second series)

Data in Figure 5, *b* show kinetics of variations in deflection of the central part of the tube sheet as the tubes are welded to it (sequence of welding is shown in Figure 5, *a*). These data apply to the first series for the welded joint of type 1 with one tube sheet. It can be seen that the maximum deflection at the end of welding all the tubes is equal to about 0.47 mm. It should be noted that this result is in good agreement with the experimental data for such a variant of combination of geometric sizes, materials and welding conditions.

Similar data were obtained also for other types of the welded joints shown in Figure 2. Having no possibility to dwell in detail on peculiarities of each type of the welded joints, note just their effect on distortions of the tube sheet. Data in Figure 6 demonstrate this effect. Comparing them with the data in Figure 5, *b*, we can see that the best from the above standpoint is the joint of type 1 shown in Figure 2.

The second series of variants of the calculations for tubes of austenitic steel X5CrNi18-10 with filler metal SG-X2CrNi 19 9 is represented by individual results shown in Figures 7–10.

Data in Figures 7–9 correspond to type 1 of the welded joint according to Figure 2. Comparing them with the data in Figures 3–5, we can see that the presence of quenching structures for this variant is observed only in the HAZ of the tube sheet, containing small embedments of high tensile stresses σ_{rr}, which should also be allowed for in terms of the risk of cold cracking.

However, while for the first series the HAZ in a tube with high peaks (~ 1000 MPa) of stresses $\sigma_{\beta\beta}$ is most dangerous (Figure 4, *b*), in this case the risk zone is the HAZ of the tube sheet with high peaks (~ 700 MPa) of stresses σ_{rr}.

Comparing distortions in the tube sheet shown in Figure 5, *b* and Figure 9, *a*, it can be seen that in the second series the distortions are approximately 15 % lower for the joints of type 1. For other types of the

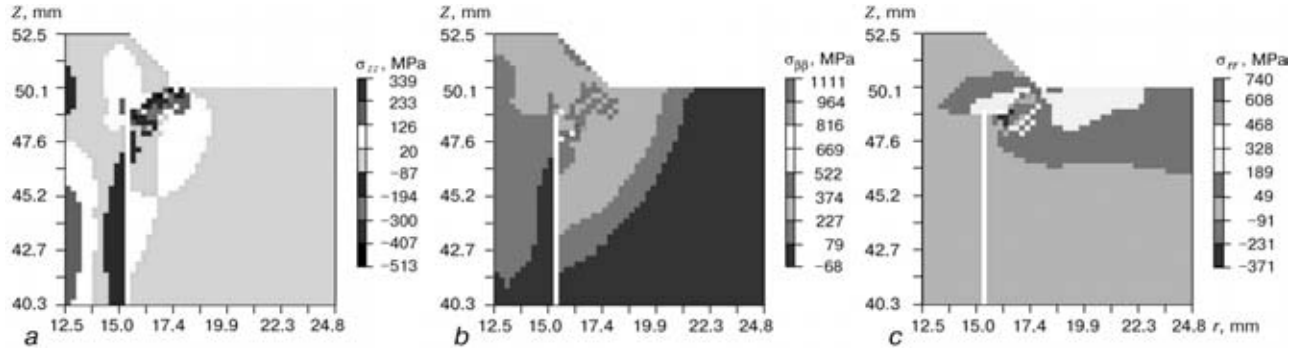

Figure 8. Results of calculations of residual stresses in the weld zone σ_{zz} (*a*), $\sigma_{\beta\beta}$ (*b*) and σ_{rr} (*c*) for the joints of type 1 (second series)

joints (see Figures 6 and 10) this difference is even larger: for types 2 and 3 it is 40 %, for type 4 — 35 % and for type 5 — 16 %. The above decrease in total distortions of the tube sheet is caused by the fact that in the second series the shrinkage phenomena during welding of the tubes take place to a considerable degree in the austenitic zone (tube and penetration zone), where the material is characterised by an increased compliance, resulting in a lower level of residual stresses and strains of the tube sheet. This phenomenon is most pronounced for the joints of types 2 and 3 (see Figure 2), where the substantial portion of the active shrinkage zone comprises austenitic metal, which is attributable to grooving.

The effect of the tube length L on deflections and a level of stresses in the tubes in the case where the heat exchanger design provides for the use of two tube sheets is shown by an example of the joint of type 1 of the second series. Sequence of welding of the tubes is the same. Figure 11 shows data on the effect of length L on deflection of the central part of the tube sheet and axial stresses in the tubes. It can be seen that at $L > 4000$ mm the mutual effect of the tube sheets is insignificant, whereas at $L < 1000$ mm the distortions markedly decrease, but axial stresses

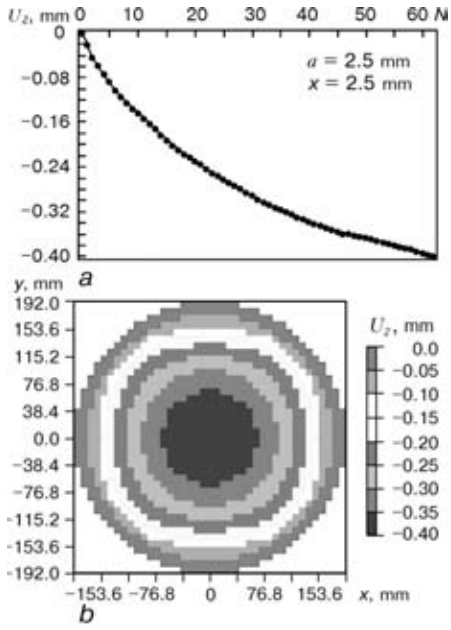

Figure 9. Results of calculations of kinetics of variations in deflection of the central part of the tube sheet during welding of tubes (*a*) and distribution of residual deflections at different points of the tube sheet (*b*) for the welded joint of type 1 (second series) (sequence of welding of tubes according to Figure 5, *a*)

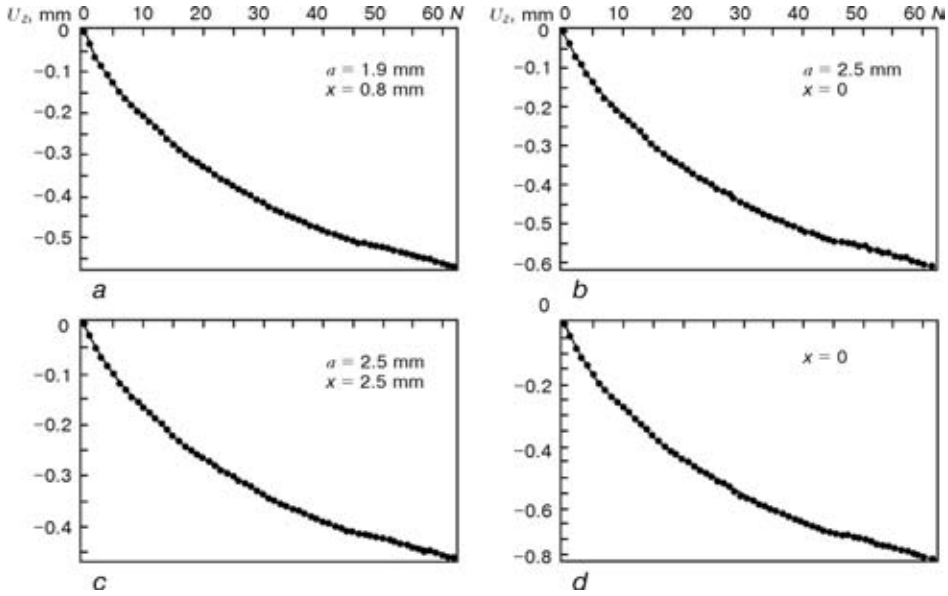

Figure 10. Kinetics of variations in deflection of the central part of the tube sheet for the joints of types *2–5* (*a–d*) (second series), respectively

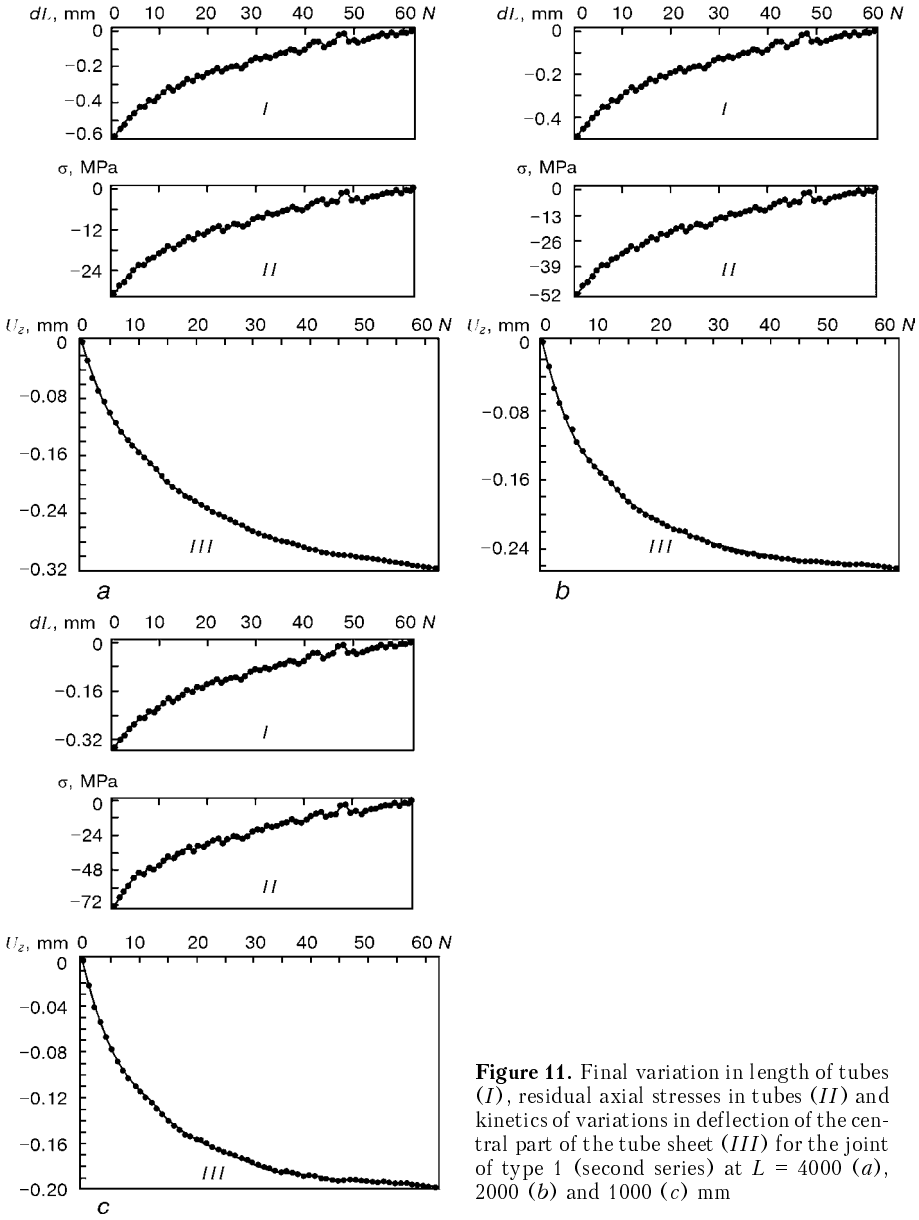

Figure 11. Final variation in length of tubes (*I*), residual axial stresses in tubes (*II*) and kinetics of variations in deflection of the central part of the tube sheet (*III*) for the joint of type 1 (second series) at L = 4000 (*a*), 2000 (*b*) and 1000 (*c*) mm

in the tubes increase. The distribution of stresses between the tubes in this case greatly depends upon the sequence of their welding to the tube sheet (Figure 12).

With this sequence of welding the maximum axial compressive stresses are induced (see Figure 5, *a*) in the central tubes which were the first to weld. This is effective in terms of decreasing distortions in the tube sheet, although this leads to a substantial axial load on the central tubes, which may cause loss in stability. In fact, a critical load for an ideally straight tube with the rigidly restrained ends can be determined from the following relationship:

$$\sigma_{cr} = -\frac{4\pi^2 E}{\lambda^2},$$

where λ is the longitudinal rigidity equal to $\lambda = L/i$; and i is the radius of the inertia moment of the tube section; in the given case i = 3.88 mm.

According to the calculations, the σ_{cr} value for tubes 1000, 2000 and 4000 mm long is equal to −118.5, −29.6 and −7.4, respectively. Comparing data of Figure 11, we can see that with the sequence of welding the tubes shown in Figure 5, *a*, at L = 2000 mm and more the risk of loss in stability of the central tubes is very high.

CONCLUSIONS

The developed computer program allows sizes of the penetration zone, its average chemical composition and microstructure, changes in microstructure of the HAZ of the base metal, residual local stresses in the welded joint zone, total distortions in the tube sheet and residual axial forces in the tubes to be predicted in welding of a characteristic assembly of heat exchangers (tube sheet to tubes).

The program is fitted with a data base on thermal-physical, mechanical and metallophysical (characteristics of TTT and Schaeffler diagrams) properties

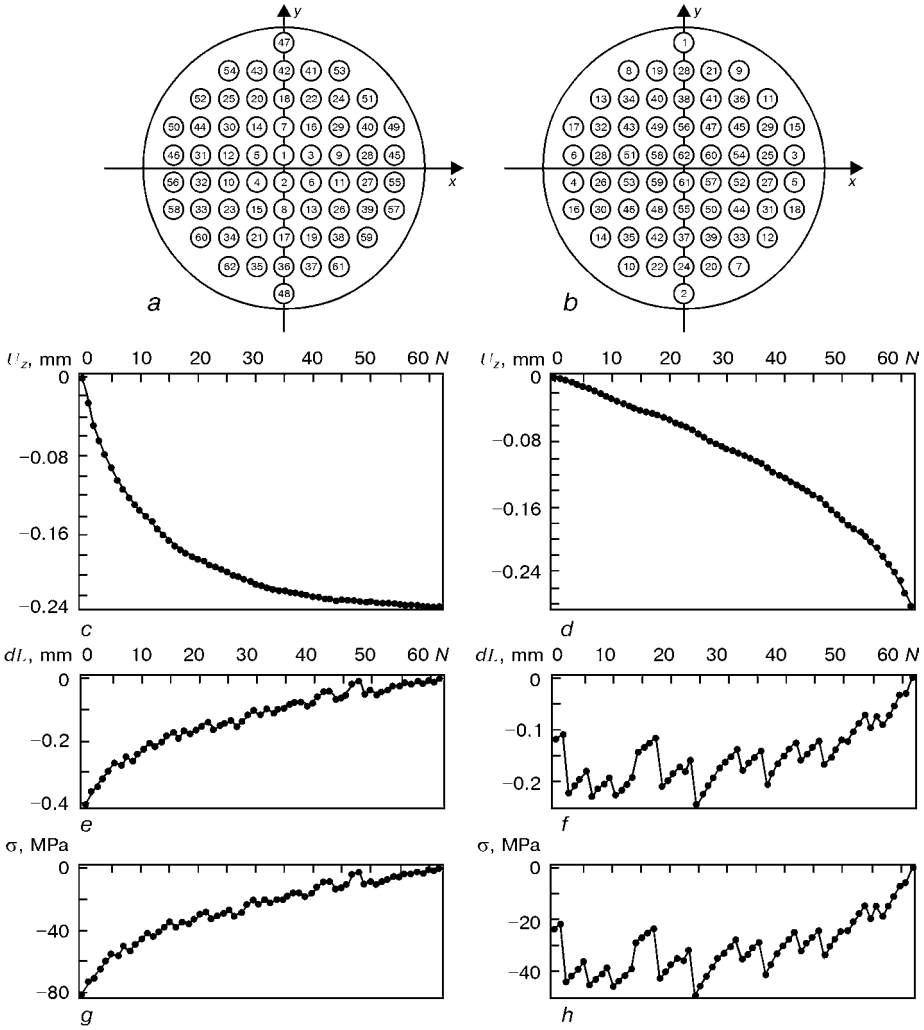

Figure 12. Distortions in the tube sheet and tubes in the case of type 1 of the welded joint for two tube sheets (tubes 1 m long) and for two variants of the welding sequence: *a* — first variant (from the centre to the ends); *b* — second variant (from the ends to the centre); *c*, *d* — kinetics of deflection of the central part of the tube sheet as the tubes are welded to it for the first and second variants, respectively; *e*–*h* — variations in length of the tubes and stresses in them after welding of all the tubes for the first and second variants (first series), respectively

of typical materials for the assemblies under consideration, and has a user-friendly interface.

Results of testing the program on a specific combination of geometric sizes, mechanical properties and welding conditions taken from experiments show the following:

- calculated and experimental data are in satisfactory agreement as to the most complicated prediction indicator, i.e. distortions of the tube sheet;
- other conditions being equal, type 1 of the welded joint exhibits the lowest distortions among five types of the tube sheet to tube joints considered (see Figure 2);
- use of austenitic steel for tubes and filler metal allows lower residual local stresses to be produced in the welded joint zone, compared with the variant of ferritic steel, the risk of cold cracking to be reduced, and residual total distortions in the tube sheet to be decreased;
- in the case of designs providing for two tube sheets and short tubes, simultaneous welding of a certain sequence of the tube ends can lead to a substantial decrease in distortions of the tube sheets, especially if the latter have a limited thickness; however, in this case it is necessary to take into account the risk of loss in stability during axial compression of the tubes which are the first to weld.

1. Makhnenko, V.I., Velikoivanenko, E.A., Makhnenko, O.V. et al. (1999) Computer-aided modeling of welded processes as the mean of prediction of defects in welded joints. *Avtomatich. Svarka*, **12**, 10–19.
2. Makhnenko, V.I., Velikoivanenko, E.A., Kravtsov, T.G. et al. (2001) Numerical studies of thermomechanical processes in surfacing of shafts of ship mechanisms. *The Paton Welding J.*, **1**, 2–10.
3. Seyffarth, P., Kasatkin, O.G. (1982) Calculation of structural transformations of the welding process. *Doc. IIW-1228–82*.
4. (1991) *Atlas of time-temperature diagrams for irons and steels*. Ed. by C.V. Vander Voort. ASM.
5. Makhnenko, V.I. (1975) *Computational methods of investigation of welded stress and strain kinetics*. Kyiv: Naukova Dumka.
6. Ueda, Y., Murakawa, H., Nakacho, K. at al. (1995) Establishment of computational welding mechanics. *Transact. of JWRI*, **2**, 73–86.
7. Makhnenko, V.I., Lobanov, L.M., Makhnenko, O.V. (1991) Prediction of total deformations of welded assemblies on the base of data bank on transverse and longitudinal shrinkage and angular deformations of appropriate specimens. *Avtomatich. Svarka*, **10**, 1–5.

SIMULATION OF THERMAL AND SOLIDIFICATION PROCESSES IN LASER WELDING OF ALUMINIUM PLATES

V.A. KARKHIN[1], **V.V. PLOSHIKHIN**[2] and **Kh.V. BERGMAN**[3]
[1]St.-Petersburg State Technical University, St.-Petersburg, Russia
[2]Bairout GmbH, Germany
[3]Bairout University, Germany

The paper deals with the method of solving an inverse quasi-stationary problem of heat conductivity to determine the parameters of laser welding mode by measured (specified) characteristics of the weld. The objective function is taken to be the sum of weighted squares of the differences of calculated and assigned characteristics of the weld and magnitudes of the sought parameters, as well as regularisation terms. Effective (input) energy is determined by the measured weld width and angle of crystallographic orientation of weld metal grains in laser welding of an aluminium alloy. Influence of welding mode on weld pool shape and weld metal microstructure is demonstrated.

Key words: *simulation, inverse problem of heat conductivity, thermal processes, solidification, laser welding, aluminium alloy*

Practical welding often raises problems, related to finding such parameters of the welding mode, which yield the desired results (necessary parameters of the weld, required properties of weld and HAZ metal, etc.), or inverse problems, when more parameters are to be reconstructed, in particular, the power of the heat source is to be determined from the available experimental data (weld shape parameters, kind of microstructure of the weld metal and HAZ). The latter pertains to the class of inverse problems, i.e. finding from consequential results the causes for their achievement [1–3].

It is much more difficult to derive the solution of the inverse problem of heat conductivity (IPHC), than that of a direct problem, as the first is highly sensitive to measurement errors. Lowering of sensitivity is only possible through regularisation [1, 2]. Methods, based on solving IPHC, are extensively used in investigation and retrofitting of thermal modes of various systems in aircraft, aerospace and power engineering. Methods to solve IPHC in relation to welding processes have been developed over the last years [4–7].

The aim of this study is development of the method to solve the inverse quasi-stationary problem of heat conductivity for the case of butt laser welding of plates (Figure 1, *b*). This example corresponds to butt welding with edges flanging, edge surfacing, etc.

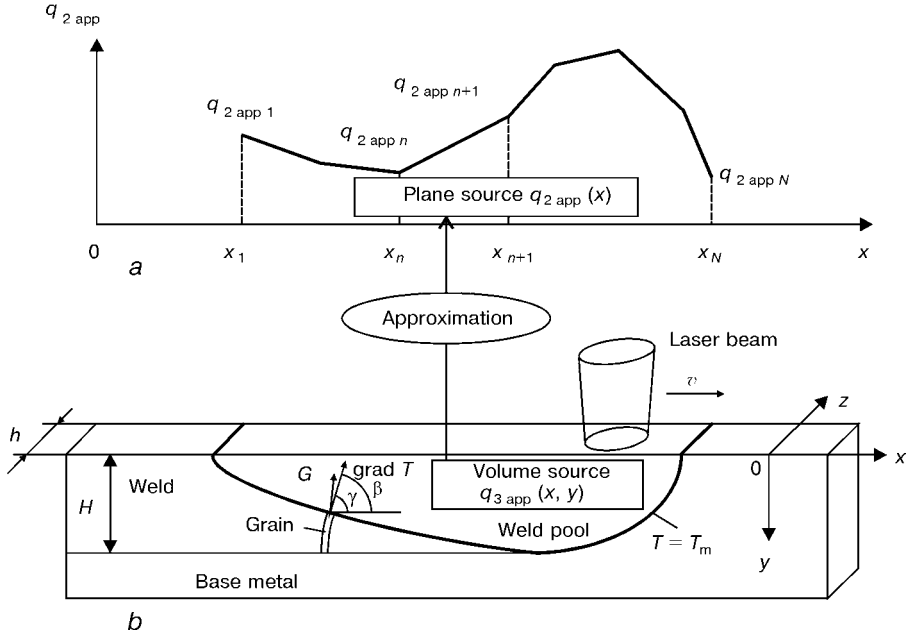

Figure 1. Presentation of an equivalent volume source in a weld pool in the form of an equivalent plane source on plate edge: *a* — piecewise-linear distribution of density of an equivalent plane source on plate edge; *b* — schematic of laser welding

Solution of the direct problem of heat conductivity. Algorithm of solution of IPHC is based on solution of the appropriate direct problem. Let a heat source (laser beam) move in a straight line along axis x at a constant speed v (see Figure 1, *b*). Then, the quasistationary linear equation of heat conductivity in a mobile system of co-ordinates x, y, z becomes

$$\lambda\nabla^2 T + c\rho v\frac{\partial T}{\partial x} + q_{3\,\text{app}} = 0, \qquad (1)$$

where

$$q_{3\,\text{app}} = q_{3\,\text{net}} - c\rho\left(w_x\frac{\partial T}{\partial x} + w_y\frac{\partial T}{\partial y} + w_z\frac{\partial T}{\partial z}\right) + q_{3L}.$$

Here λ is the heat conductivity; $c\rho$ is the volumetric heat capacity; $q_{3\,\text{app}}$ is the power density of an equivalent volume source; w_x, w_y and w_z are the components of convective speed of the liquid. Equivalent source allows for the actual source, i.e. laser beam, $q_{3\,\text{net}}$, convection of liquid in the weld pool (summand in brackets), heat of melting and solidification, q_{3L}.

Let us assume that the plate is relatively thin (there is no temperature gradient across the thickness, $dT/dz = 0$). If the weld pool is relatively long (has an elongated shape), the volume source may be approximated by a plane one, active on the plate edge (see Figure 1). Distribution of power density of an equivalent plane source $q_{2\,\text{app}}(x)$ is represented with sufficient accuracy in the form of a piecewise-linear function (see Figure 1, *a*). Then the solution of equation (1) for a uniform plate is given by the following expression:

$$T(x, y) = \frac{1}{\pi\lambda}\sum_{n=1}^{N-1}\int_{x_n}^{x_{n+1}}\times$$
$$\times\left[q_{2\,\text{app}\,n} + \frac{q_{2\,\text{app}\,n+1} - q_{2\,\text{app}\,n}}{x_{n+1} - x_n}(\xi - x_n)\right]\times$$
$$\times\exp\left[-\frac{v(x-\xi)}{2a}\right]K_0\left(\frac{vr}{2a}\sqrt{1+\frac{4ab}{v^2}}\right)d\xi + T_0; \qquad (2)$$

$$r = \sqrt{(x-\xi)^2 + y^2};\quad b = 2\alpha/(c\rho h),$$

where a is the temperature conductivity; K_0 is the modified zeroth order Bessel function of the second kind; α is the coefficient of surface heat removal; T_0 is the initial temperature; h is the plate thickness; N is the number of points to assign curve $q_{2\,\text{app}}(x)$ (see Figure 1, *a*). In reality the values of power density $q_{2\,\text{app}\,n}$ in individual points $x_n (n = 1, \ldots, N)$ are not known, being the solution of an inverse problem.

Equation (2) allows calculation of all the characteristics of the temperature field (maximal temperature, temperature gradient and its direction, etc.).

Solution of a direct problem of solidification. If the angles of crystallographic orientation of weld metal grains are taken as the experimental data during solution of IPHC, it is necessary to solve a solidification problem, relating these angles to the temperature field. This problem was solved by the method of calculation of grain boundaries evolution, based on the following physical assumptions [8]:

- solidification front is assigned by melting isotherm T_m;
- distribution of the size and crystallographic orientation of individual grains in the base metal are known;
- crystallographic axes [100] and [010] of all the grains are in the plate plane, and the axis, which deviates from y axis by not less than 45°, is taken to be [100]. The [001] axis is normal to the plate plane. Thus, the solidification problem is a two-dimensional one, which is valid for the case of welding thin plates;
- at solidification the new boundary $0A$ between the adjacent grains *1* and *2* is formed, depending on the crystallographic orientations of grains G_1 and G_2 and directions of local temperature gradient grad T at the solidification front $T = T_m$ (Figure 2).

Let at current moment t, the grain boundary on the solidification front be in point 0. Then the growth of the boundary in a short time interval Δt (point A at the solidification front at moment $t + \Delta t$) can be determined, proceeding from the following criterion of grain selection: the grain with the crystallographic orientation, closer to that of the temperature gradient, has a growth advantage over the adjacent grain (Figure 2, *a*–*c*). If the directions of grain growth diverge, the new boundary coincides with the local temperature gradient (see Figure 2, *d*). The latter assumption is based on experimental observations, which indicate that in grain *1*, in which the deviation in direction of

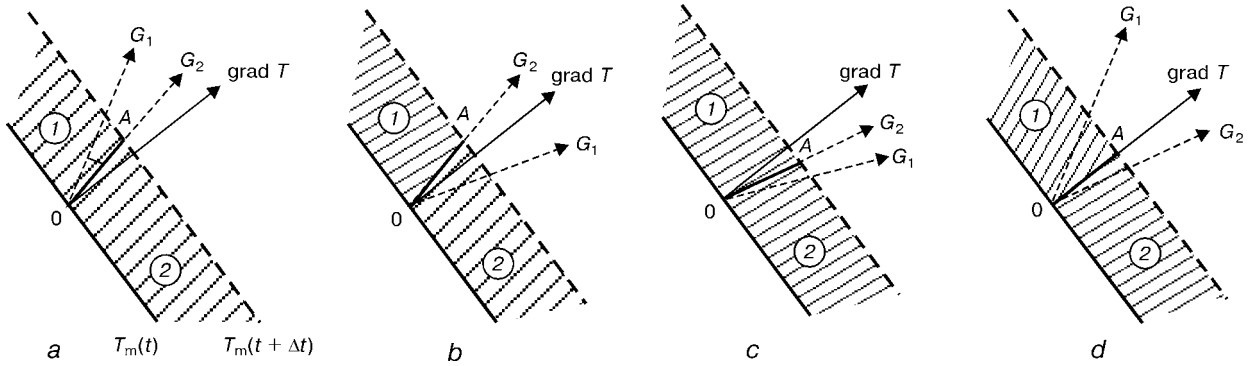

Figure 2. Schematic of formation of $0A$ boundary between the growing adjacent grains *1* and *2* on the solidification front in a short time interval Δt (G_1 and G_2 — directions of crystallographic orientation of grains *1* and *2*)

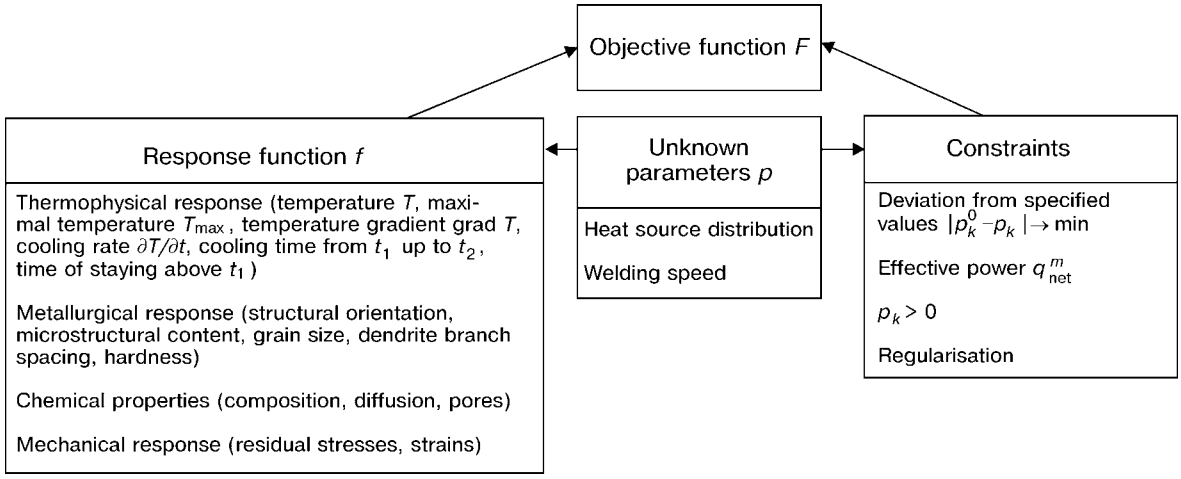

Figure 3. Components of objective function

growth of G_1 primary branches from the direction of temperature gradient grad T is greater than for adjacent grain *2*, secondary branches are developing more intensively, compared to secondary branches of adjacent grain [8].

Solution of crystallogrpahic problem is the set of boundaries between all the grains, i.e. calculated macrosection of the weld in the plate plane, statistical processing of which yields the distribution of grain size and angle of [100] directions of crystallographic orientation of grains γ (mathematical expectation, dispersion, etc.) at any distance from the weld boundary.

Accepted model is experimentally confirmed for the case of laser welding, when due to high temperature gradients and high solidification rates, the weld microstructure has a cellular-dendritic morphology, i.e. predominantly consists of primary and ternary dendrite axes with a pronounced directivity, corresponding to crystallographic orientation [8].

Solution of inverse problem. The following objective function is the criterion of accuracy of solving the inverse problem:

$$F(\mathbf{p}) = \sum_{j=1}^{J} w_j^f \left[f_j^m - f_j(\mathbf{p})\right]^2 + \sum_{k=1}^{K} w_k^p \left[p_k^0 - p_k\right]^2 + w^q [q_{net}^m - q_{net}(\mathbf{p})]^2 + w_0 \sum_{n=1}^{N} [p_n]^2 + w_1 \sum_{n=1}^{N-1} [p_{n+1} - p_n]^2 + w_2 \sum_{n=1}^{N-2} [p_{n+2} - 2p_{n+1} + p_n]^2,$$

where J is the number of measurements; K is the number of sought parameters ($K \geq N$); q_{net}^m, q_{net} is the assigned and calculated value of effective power of the laser beam

$$q_{net} = q_{app} = \frac{1}{2} h \sum_{n=1}^{N} p_n (x_{n+1} - x_{n-1}), \qquad (3)$$

where q_{app} is the equivalent source power; $p_n = q_{2\,app}(x_n)$; $x_0 = x_1$ and $x_{N+1} = x_N$. Equality $q_{net} = q_{app}$ in equation (3) follows from the condition of heat balance.

Let us clarify the physical meaning of the given function F of the vector of sought parameters $\mathbf{p}$, $\mathbf{p} = \{p_1, p_2, \ldots, p_k\}$. In the general case, the sought parameter p_k can be the power density in a specified point, welding speed, etc. Response function f (experimental and calculated values in j-th point, f_j^m and f_j) is a thermophysical, metallurgical, chemical or mechanical characteristic (Figure 3). Constraints may contain specified a priori value of k-th parameter p_k^0, constraints by its sign and value, effective power q_{net}, etc. (Figure 3). Weighting coefficients w_j^f and w^q depend on measurement error f_j^m and q_{net}^m, and weighting coefficient w_k^p on admissible change of parameter p_k relative to specified p_k^0 value. If effective (input) power q_{net}^m is unknown, $w^q = 0$ is assumed. Regularisation of zeroth, first and second order (coefficients w_0, w_1, w_2) allows smoothing the function of power distribution and assigning its form. Thus, objective function F allows taking prior knowledge of the object into account in a flexible manner.

Solution of the inverse problem by definition is absolute minimum of objective function F. Function F was minimised, using Gauss–Newton iteration method [7]. Direct problems of heat conductivity and solidification were sequentially solved in each iteration. It should be noted that without regularisation the solution of inverse problem might be unstable.

Experiment. Edges of a plate 1.15 mm thick were remelted by the laser beam of 0.6 mm diameter. Material was aluminium alloy AS 120 (1.05–1.20 % Si and 0.36–0.44 % Mg). Measured were weld width (penetration depth) H on transverse macrosections and angle of [100] directions of crystallographic orientations of weld metal grains using the method of X-ray diffractometry [9].

Thus, taken as experimental values of response function f^m were maximal temperature T_{max}, equal to melting temperature T_m, at $y = H$ and average values of the angle of orientation of grains γ at assigned coordinates y. Maximal temperature T_{max} at $y = H$

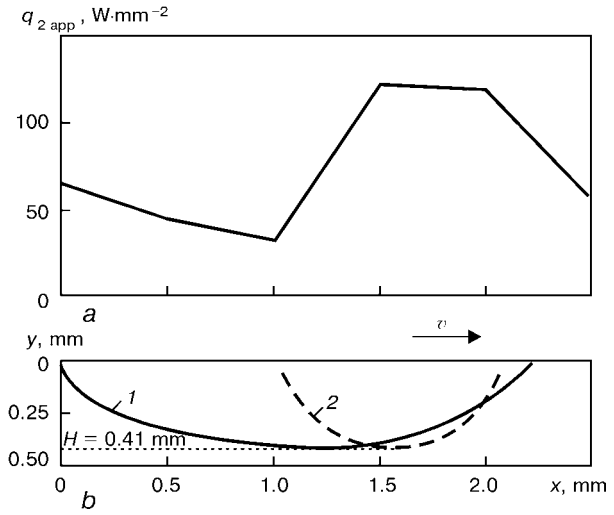

Figure 4. Distribution of power density of an equivalent plane source on plate edge (*a*) and weld pool shape (*b*) at laser beam power of 1700 W and welding speed of 50 mm·s^{-1}: *1* — plane source, equation (*2*); *2* — linear source, equation (*4*)

and values of the most probable angle γ were taken as the calculated values of response function *f*.

Result analysis. Problems were solved with the following initial data: laser beam power q_{gross} = = 1700 W; a = 76.3 mm^2·s^{-1}; λ = 0.175 W·mm^{-1}·K^{-1}; T_m = 890.5 K; T_0 = 293 K; α = 0.00005 W·mm^{-2}·K^{-1}; w_j^f = 10 K^{-2}, if $f_j = T_{max}$; w_j^f = 1 K^{-2}, if $f_j = \gamma_j$; w_k^p = = 0; w^q = 0; w_0 = 0.0001–0.1; w_1 = 0–0.01; w_2 = = 0–0.01 W^{-2}·mm^4. Welding speed was varied in the range of 16.7–50 mm·s^{-1}. When solidification was simulated, it was assumed that the distribution of the size and crystallographic orientation of base metal grains are random and uniform, with the initial grain diameter being in the range of 20–30 μm. Solution of the inverse problem are the values of power density $q_{2\,app\,n}$ in fixed points x_n (n = 1, ... , N; N = K).

Figure 4, *a* shows power distribution $q_{2\,app}$ at the welding speed v = 50 mm·s^{-1}. Maximum in the pool front part corresponds to the position of the laser beam, and a certain rise in the tail part — to the effect of solidification heat. Effective efficiency of plate heating with the laser beam is equal to 12.8 %, which is close to value (η = 12 %), measured at a stationary beam with wave length of 1.06 μm [10]. Pool front part is determined in an approximate manner, as no constraints are applied to its shape or dimensions (Figure 4, *b*).

Calculation schematics of simple idealised heat sources are popular in practical welding work. If an equivalent source is further simplified and taken to be concentrated on $x = x_0$ line, we obtain a known schematic of a linear source on plate edge [11]:

$$T(x, y) = \frac{q_{app}/h}{\pi\lambda} \exp\left[-\frac{v(x - x_0)}{2a}\right] \times \times K_0\left(\frac{vr}{2a}\sqrt{1 + \frac{4ab}{v^2}}\right) + T_0. \quad (4)$$

It should be noted that application of a linear source schematic leads to a calculation formula of the

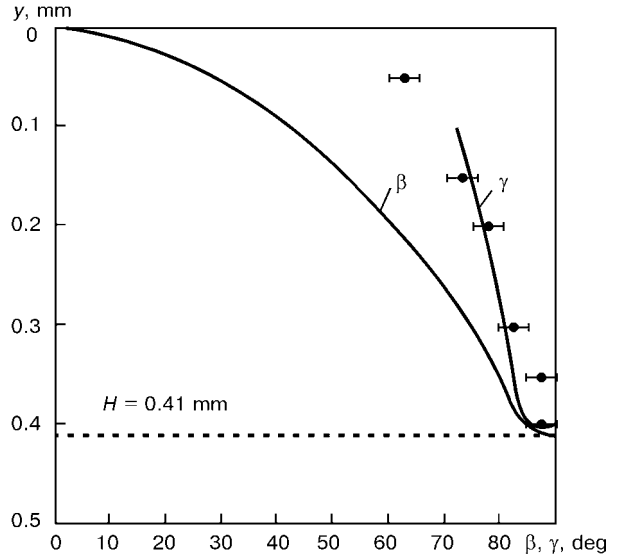

Figure 5. Distribution of angles of temperature gradient β and the most probable [100] direction of crystallographic orientation of grains γ across weld width (solid line — calculation, dots — experiment)

weld, close to a half-sphere (Figure 4, *b*). In this case, the only unknown is the value of power q_{app}, and, therefore, it is in principle impossible to simultaneously simplify experimental conditions, either by penetration depth, or by the angle of grain orientation.

The most probable value of angle γ of [100] crystallographic orientation of the grains, depending on y coordinate (Figure 5) was calculated. It is seen that angle γ is relatively close to the angle of temperature gradient β through the entire depth of the weld, except for a small zone near the plate edge. The latter is attributable to the fact that change of temperature gradient direction resulted in grain selection proceeding mainly between [010] directions and not [100] directions of the crystallographic orientation. In other words, if at «vertical» position of temperature gradient in the lower part of the weld pool (β ≈ 90°) grain

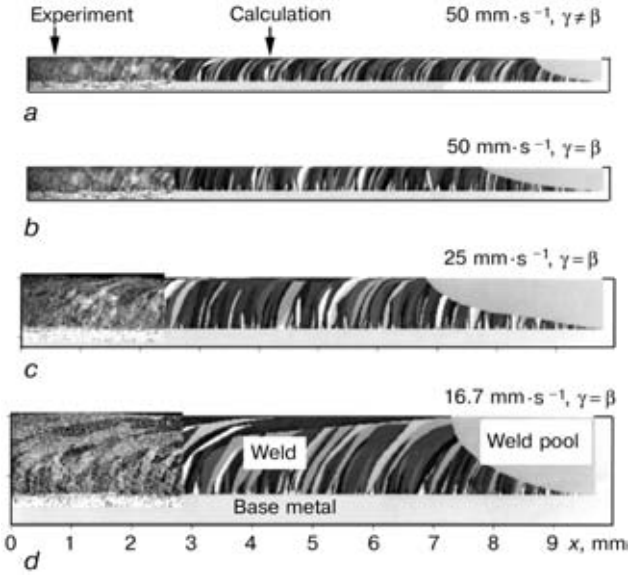

Figure 6. Experimental and calculated longitudinal macrosections at different welding speed (just the tail part of weld pool shown)

growth proceeds due to the initial dendrites of [100] orientation, in the weld pool upper part at a horizontal position of temperature gradient ($\beta \approx 0°$) growth of the same grain is due to secondary dendrite branches, having [010] orientation, respectively.

At welding speed v = 50 mm·s^{-1} pulses of 50 Hz frequency were applied, this leading to visible inhomogeneity bands on longitudinal macrosections (Figure 6, *a*). It is seen, that the calculated boundary of weld pool tail part is close in shape to dark bands on the macrosection. If the influence of convection of weld pool liquid metal and heat of melting and solidification is ignored (schematic of a linear source in Figure 4, *b*), the calculated shape of the weld is markedly different from the experimental shape.

If the direction of temperature gradient grad T on the solidification front is taken to be the grain orientation G ($\beta = \gamma$, Figure 1), solution of the inverse problem is simplified (solidification problem need not be solved). In this case, however, the calculated weld pool is too long (Figure 6, *a, b*).

Welding mode significantly influences the shape of weld pool and weld metal texture (Figure 6, *b–d*). Weld pool shape determines the predominant crystallographic orientation of grains (most probable value of angle γ). The more elongated is the shape, the greater angle γ. The wider the weld pool relative to the size of base metal grains, the more intensive is grain selection, this leading to a difference in the texture, and, therefore, in the properties between the weld and base metal. The difference becomes greater with greater distance from the weld.

On the whole, the calculated microstructure of weld metal correlates in a satisfactory manner with the experimental one (Figure 6).

It should be noted that the above procedure might be used also in other methods of fusion welding.

CONCLUSIONS

1. Developed method to solve the inverse problem of heat conductivity allows determination of laser welding mode by the measured characteristics of the weld.

2. Proposed objective function allows taking into account preliminary knowledge of the welding process.

3. Laser welding mode has a strong influence on the calculated texture of weld metal, which depends on the weld pool shape and ratio of base metal grain size to weld width.

1. Tikhonov, A.N., Arsenin, V.Ya. (1979) *Methods of solving ill-defined problems*. Moscow: Nauka.
2. Beck, J.V., Blackwell, B., Saint-Clair, Ch. (1989) *Ill-defined inverse problems of thermal conductivity*. Moscow: Mir.
3. Kurpisz, K., Nowak, A.J. (1995) *Inverse thermal problems*. Southampton, Boston: Comput. Mech. Publ.
4. Beck, J.V. (1991) Inverse problems in heat transfer with application to solidification and welding. In: *Modelling of casting, welding and advanced solidification processes*. Ed. by M. Rappaz, M.R. Ozgu, K.W. Mahin.
5. Zabaras, N. (1991) Inverse modelling of solidification and welding processes. *Ibid*.
6. Al-Khalidy, N. (1996) Two-dimensional inverse phase change problem. In: *Advanced computational methods in heat transfer*. Ed. by L.C. Wrobel, G. Comini, C.A. Brebbia, A.J. Nowak. Southampton, Boston: Comput. Mech. Publ.
7. Karkhin, V.A., Ilyin, A.S., Plochikhine, V.V. et al. (2001) Inverse modelling of the heat input distribution during deep penetration laser and electron beam welding. In: *Proc. of 8th Conf. on Laser Mater. Processing in the Nordic Countries*. Copenhagen, Aug. 13–15, 2001.
8. Ploshikhin, V.V., Bergmann, H.W. (1998) Simulation of grain structures in laser beam welds undergoing the planar solidification mode. In: *Mathematical modelling of weld phenomena*. Ed. by H. Cerjak. Vol. 4. London: The Inst. of Mater.
9. Bergmann, H.W., Mayer, S., Mueller, K. et al. (1998) Texture evolution in laser beam welds undergoing the planar solidification mode. *Ibid*.
10. Dausinger, F. (1995) *Strahlwerkzeug Laser: Energeeinkopplung und Processeffektivitaet*. Stuttgart: Teubner.
11. Boulton, N.S., Lance Martin, H.E. (1936) Residual stresses in arc-welded plates. In: *Proc. Inst. Mech. Eng*. Vol. 133. London.

EFFECT OF GAP ON SIZES OF BUTT WELD IN CONSUMABLE ELECTRODE ARC WELDING IN Ar + 25 % CO_2 MIXTURE

I.F. KORINETS and **JI CHENG CHUNG**
National Technical University of Ukraine «KPI», Kyiv, Ukraine

Dependence of weld shape on gap value in consumable electrode arc welding in Ar + 25 % CO_2 mixture of a square butt joint was established and a deterministic-statistical model of weld shape with allowance for a gap effect was developed. The developed model is recommended for use in the design of software of the system of adaptive control of arc welding of butt joints with a non-stable gap.

Key words: *arc welding, consumable electrode, shielding mixture, square butt joint, gap, weld sizes, mathematical model*

The arc welding in CO_2 and Ar + CO_2 mixture finds a wide application in welding structures from low-carbon and low-alloy steels. In welding metal of small and medium thicknesses the single-pass fillet and butt welds are most widely spread. As a rule, the semi-finished products are used in this case without edge bevel, but they are assembled in butt joints with an obligatory gap. It is known that in butt joints of sheet and tubes the gap influences greatly the sizes and quality of weld formation both in welding without and with a backing. It is almost impossible to provide a stable gap in butt even at high-precision edge preparation and assembly, as the edge distortions are inevitable in the process of fusion welding. In these conditions the gap is one of main technological factors influencing the butt weld formation.

The first regularities about gap influence on the weld formation were obtained under the submerged-arc welding conditions [1–3]. These results are still valuable from the scientific and practical point of view. However, to use them directly for the consumable electrode shielded-gas arc welding is not possible. Some researchers took into account the effect of gap on weld shape together with other factors in the development of mathematical models of the weld formation, creation of calculation methods of determination and optimizing conditions of the CO_2 arc welding [4–6]. Other data about the gap influence on weld shape under consumable electrode shielded-gas arc welding conditions were not found. However, at present the research works concerning the effect of a gap on weld formation are still actual due to creation of adaptive systems of arc welding control, which should react in real time on random deviations in edge preparation, including also those in the butt gap.

Therefore, the aim of the work is to study a gap effect on the weld formation in consumable electrode arc welding in Ar + 25 % CO_2 mixture and to design a mathematical model of weld shape with a butt gap.

Design of deterministic-statistical model of weld shape. Mathematical model of the weld shape should establish the dependence of sizes of butt weld (depth of penetration h, weld width e, height of weld convexity g) (Figure 1, *a*) and its shape (penetration shape coefficient ψ_p, bead shape coefficient ψ_b) on parameters of welding conditions (electrode wire diameter d, welding current I, welding speed v, electrode wire feed speed v_f, welding voltage U, electrode wire stickout L, consumption and composition of shielding gas q) and gap value b.

It is known that welding parameters influence sizes and weld shape to a different degree. Consumption of shielding gas and electrode wire stickout, which is kept constant and equal to $L = 10d$, have the least influence on the weld sizes. Welding current and electrode wire feed speed are interdependent parameters and, therefore, one of them can be excluded, for example, electrode wire feed speed. If to take into account such circumstance that electrode wires of 1.0 and 1.2 mm diameter are used mainly in world practice, then it is possible to exclude the consideration of effect of electrode wire diameter on weld shape at the first stage of investigation. Welding voltage influences greatly the weld width. However, the optimum value of voltage is associated with welding current and not changed within the wide limits. If to assume that the optimum voltage depends on welding current, then its influence on the weld shape will be

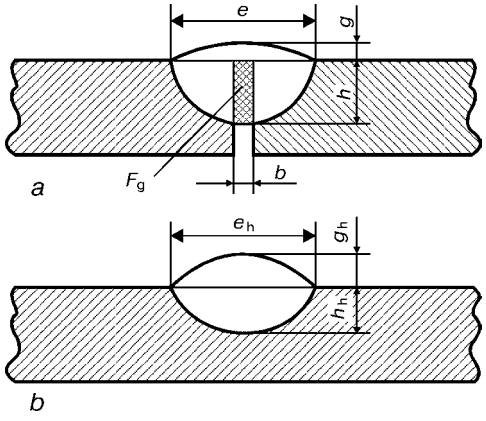

Figure 1. Sizes of butt weld (*a*) and deposited bead (*b*)

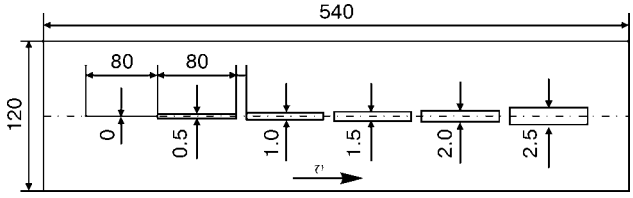

Figure 2. Sample-simulator of butt weld with a variable gap

taken into account automatically in a model by welding current. This analysis makes it possible to decrease the number of welding condition parameters in the model which effect on the weld formation, i.e. welding current and welding speed are taken into account first of all.

To solve the problem, we used a method of deterministic-statistical modelling, suggested in [7], in which the dependence of weld sizes on welding parameters and gap value is presented in the form of a product of power functions, and the coefficients are determined as a result of statistical processing of the experimental data.

The investigations enable us to offer several variants of models which are differed by representation of relationship between the weld size and gap. In the first variant of the model the dependence of weld sizes on gap has a form of a power function:

$$h = 0.595\frac{I^{0.531}}{v^{0.486}}b^{0.176}, \quad (1)$$

$$e = 0.069\frac{I^{1.051}}{v^{0.324}}, \quad (2)$$

$$g = 1.465\frac{I^{0.295}}{v^{0.679}}\frac{1}{b^{0.129}}. \quad (3)$$

However, in case of a zero gap in the butt and during hardfacing the depth of penetration and convexity height are equal to zero, that contradicts the real process. Expression (2) attracts attention as it shows that the weld width does not depend on the gap.

In the second model there is no drawback of the first variant of the model:

$$h = 0.042\frac{I^{0.950}}{v^{0.496}}(1+b)^{0.658}, \quad (4)$$

$$g = 1.047\frac{I^{0.413}}{v^{0.638}}\frac{1}{(1+b)^{0.453}}. \quad (5)$$

The third variant of the model is also possible, in which the dependence of weld sizes on gap is presented in the form of an exponential function:

$$h = 0.020\frac{I^{1.094}}{v^{0.409}}1.284^{b}, \quad (6)$$

$$g = 1.062\frac{I^{0.469}}{v^{0.778}}0.692^{b}. \quad (7)$$

Verification of adequacy of models. Determination of coefficients in equations (1)–(7) and verification of adequacy of models were made in welding of series of samples-simulators of butt joint with a gap (Figure 2). The samples-simulators of steel VSt.3 (killed) represented 5 mm thick plates, in which the slots were made by a cutter at a stepped change in a gap. Small length of the slots and the presence of bridges between them guarantee the gap stability. The arc welding in mixture Ar + 25 % CO_2 was performed with 1.2 mm diameter Cu-plated wire Sv-08G2S. The welding condition was changed within the following ranges: I = 140, 180 and 220 A, U = = 24, 26 and 27 V, v = 5.7, 7.6, 10.2, 12.8, 15.0 and 17.6 mm/s, q = 10–12 l/min. Welding was made on a copper backing. At 2.5 mm gap under all the conditions the arc was submerged into a gap and the quality formation of the weld was not obtained. After welding the transverse templets were cut, etched and the welds were measured. The results of calculation and experimental data of the third model are presented in Figure 3.

The comparison of experimental and calculation data showed that the mean relative error in determination of the penetration depth was 10, 7.2 and 6.9 %, respectively, in the 1st, 2nd and 3rd model, weld convexity — 6.9, 5.9 and 5.7 %, respectively, and weld width — 8 % for all the models. The 3rd model provided the highest accuracy.

Discussion of results. Under the welding conditions considered three variants of formation of joints can be distinguished: with a convex weld, with a concave weld and with welds having lack of penetration of edges. In the first case a stable process is observed with an arc which is submerged partially into the parent metal. In the second case a stable process is also observed but with an arc which is submerged completely into the parent metal. Gap is not filled with a deposited metal. In the third case the arc is submerged completely into the parent metal, the welding process is instable, the arc is chaotically moved across the metal thickness upwards-downwards and displaced from one edge to another. There is no weld formation.

The results of investigations confirm the significant effect of gap on the penetration depth. Thus, the penetration depth at 2 mm gap can 2 times exceed the penetration depth in hardfacing (close butt) (Figure 3). With increase of gap the weld convexity is decreased and at large gaps the convexity transfers into concavity. The weld width does not almost depend on the gap until the complete arc submersion into the parent metal is occurred. In case of arc submersion into the parent metal, the arc wanderings are limited, the cold metal constricts it and the weld width is decreased. The ratio between the arc length and gap values influences, evidently, the arc submersion into the gap, that should be a subject of further investigations.

In the development of the calculation methods of determination of welding conditions, the relationship between the weld sizes in welding the butt with a gap and bead sizes in hardfacing is of an interest (see Figure 1, *b*). Thus, the relationships between the actual sizes of weld h and g with allowance for gap b and bead sizes in hardfacing h_h and g_h have a form

$$h = h_h + 0.8b^{1.024}, \quad (8)$$

$$g = g_h - 0.5b^{0.9}, \quad (9)$$

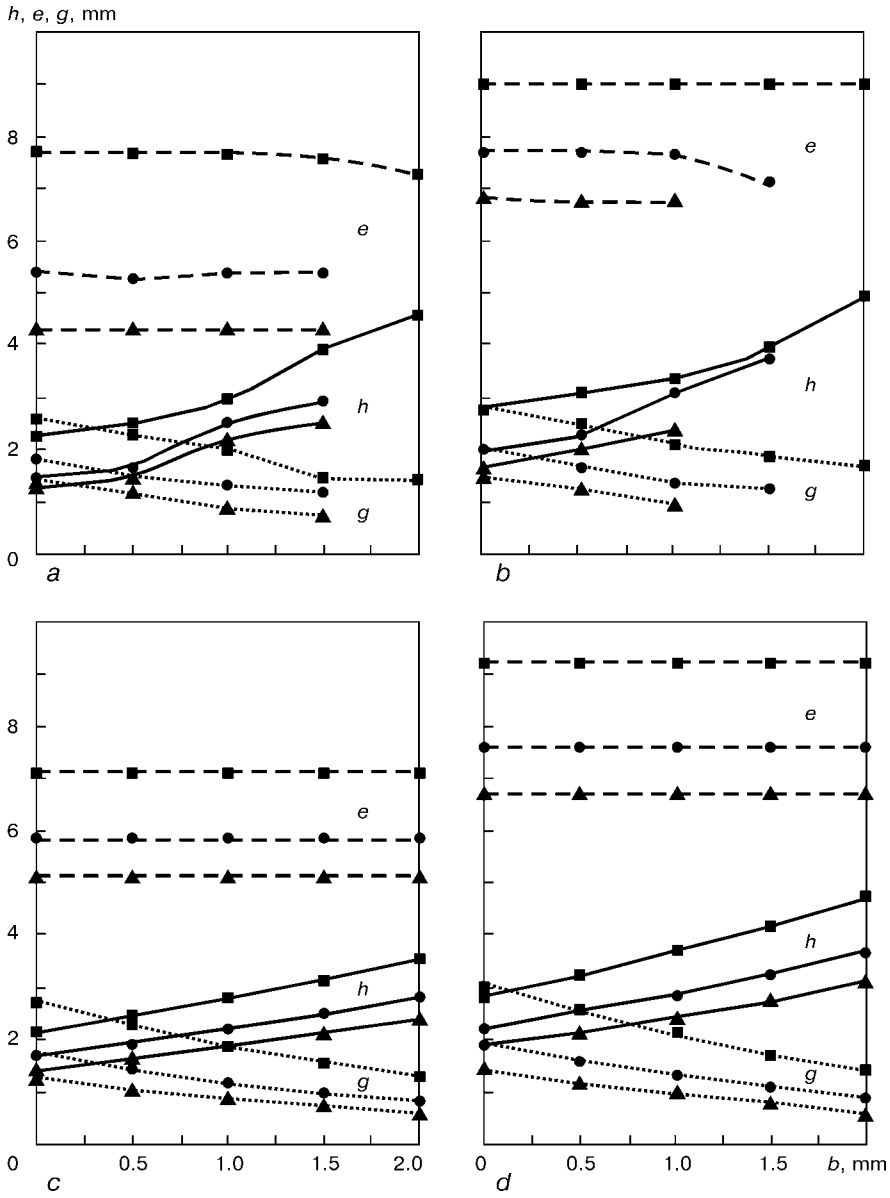

Figure 3. Effect of gap and condition of arc welding in Ar + 25 % CO_2 on weld size: *a*, *b* — experimental data at I = 140 and 180 A; *c*, *d* — calculated data at I = 140 and 180 A; ■ — v = 5.7; ● — v = 10.2; ▲ — v = 15.0 mm/s

or with allowance for area of filling the gap F_g with deposited metal (see Figure 1):

$$h = h_h + 0.4(bh)^{0.844}, \quad (10)$$

$$g = g_h - 0.382(bh)^{0.486}. \quad (11)$$

CONCLUSIONS

1. In shielded-gas consumable electrode arc welding a gap is one of the most significant technological factors influencing the depth of penetration and height of convexity (concavity) of the butt weld. The weld width does not depend on the gap value at a partial arc submersion into the parent metal.

2. Mathematical model of a shape of the square butt weld with allowance for the gap value has been developed. The expediency of accounting for two main welding parameters in the model, such as welding current and welding speed, is shown.

3. The model developed can be used in design of a software of the system of adaptive control of arc welding butt joints with a non-stable gap.

4. It is rational to continue investigations of arc behaviour in a gap and to find the optimum ratio between the arc length and voltage and the butt gap value.

1. Ostrovskaya, S.A. (1950) Square butt welding with obligatory gap. *Avtomatich. Svarka*, **2**, 2–8.
2. Donchenko, V.F. (1964) Influence of joint gap on sizes of butt weld cross-section sizes in automatic submerged-arc welding. *Svarochn. Proizvodstvo*, **9**, 24–27.
3. Donchenko, V.F. (1965) Validation of parameters of automatic submerged-arc groove welding of butt joints. *Ibid.*, **5**, 25–28.
4. Dubovetsky, S.V., Sergatsky, G.I., Kasatkin, O.G. (1980) Optimisation of CO_2 welding condition. *Avtomatich. Svarka*, **12**, 30–34.
5. Babkin, A.S., Krivosheya, V.E. (1985) Development of algorithm of microcomputer-aided calculation of CO_2 welding parameters. *Svarochn. Proizvodstvo*, **4**, 3–5.
6. Popkov, A.M. (1986) Calculation of weld parameters in CO_2 welding of butt square joints. *Ibid.*, **9**, 21–22.
7. Korinets, I.F., Ji Cheng Chung (2001) Deterministic-statistical model of weld shape in arc welding. *The Paton Welding J.*, **10**, 39–44.

CALCULATION OF PENETRATION DEPTH OF WORKPIECES IN CO_2 WELDING

E.N. VARUKHA and **A.A. MOROZOV**
Leading Attestation Center of South Region of Russian Federation

Non-linear model of penetration of a workpiece, describing the dependence of depth of penetration on parameters of process of mechanized welding and surfacing in CO_2 at reverse polarity current is presented.

Key words: *arc welding or surfacing, mathematical modelling, penetration depth, welding condition parameters, shielding gas, reverse polarity*

Until the present time there are no sufficiently exact and simple methods of calculation and registration of penetration depth of the workpiece during welding. This is stipulated by numerous factors influencing on it and difficulty in their accounting. Development of these methods could simplify the procedures of calculation of welding conditions and creation of system of an adaptive control of penetration depth for welding equipment.

To perform calculations of welding condition parameters it is necessary to preset the weld geometric sizes. Here, the relationship between the depth of penetration and weld width and main characteristics of the process (current and welding speed, arc voltage, diameter and stickout of electrode) should be known.

Until now there were many works devoted to establishing relation between the welding process parameters and geometric sizes of the weld. In the solution of this problem three main approaches can be distinguished:

- determination of relation between welding conditions and weld sizes using experimental data [1];
- making of empiric equations connecting welding condition and weld sizes using a method of a formal [2] and criterial interpolation [3];

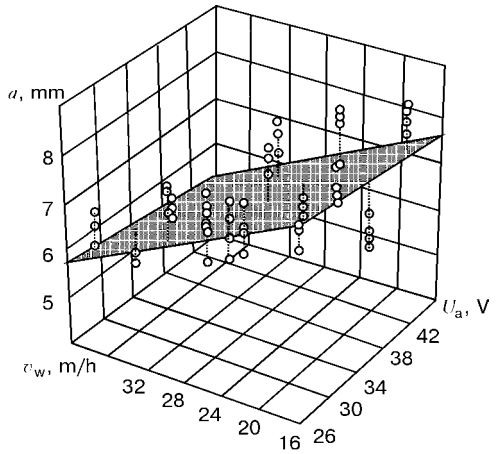

Figure 1. Dependence of penetration depth a on arc voltage U_a and welding speed v_w at d_e = 1.6 mm and v_f = 554 m/h

- development of systems of analytical equations obtained from the theory of heat transfer [4].

Each of them has drawbacks: a high labour intensity in obtaining experimental data, not high accuracy of empiric models and difficulty in accounting for all the factors influencing the distribution of temperature in the product. The rapid development of a computer engineering, the presence of powerful applied computer programs and development of a rather perfect mathematical model of electrode melting [5] make it possible to start the solution of problem of construction of a mathematical model of product penetration at the higher level.

The aim of the present work is to develop a model for calculation of depth of penetration in CO_2 surfacing and welding of butt joints without a zero gap edge preparation using a reverse polarity current.

To obtain experimental data, a series of experiments on surfacing of beads on 12 mm plates of steel St.3 (killed) in CO_2 (15–16 l/min consumption) was performed. Surfacing (welding) was realized from converter PSG-500 with a rigid volt-ampere characteristic in the 28–43 V range of voltages and 120–500 A range of currents. Surfacing rate was changed by steps from 17.6 to 38.5 m/h. Welding wires Sv-08G2S of a rated diameter d_e = 1.0, 1.2, 1.4, 1.6 and 2.0 mm were used as an electrode. For further calculations the sizes d_e, such as 0.97, 1.16, 1.4, 1.57 and 1.97 mm were taken. The wire feed speed in the process of welding was changed in the range from 165 to 650 m/h. Distance from the current-carrying nozzle end to the plate surface was 18, 20 and 22 mm, the current-carrying nozzles were made from copper of MO grade. The deposited plates were cut across the beads in two places. Macrosections were made, in which the geometrical sizes of welds were measured at an accuracy of not more than ± 0.1 mm.

For static processing four values of each measured parameters without their averaging were used. Such approach makes it possible to obtain the high accuracy in further mathematical processing of experimental data, as the root-mean-square characteristics reflect more accurately the regularities being studied than their arithmetic mean values.

For the model design a method of a multifactor regression analysis, realized in applied program «Statistika» was used. Arc voltage U_a, rate of electrode

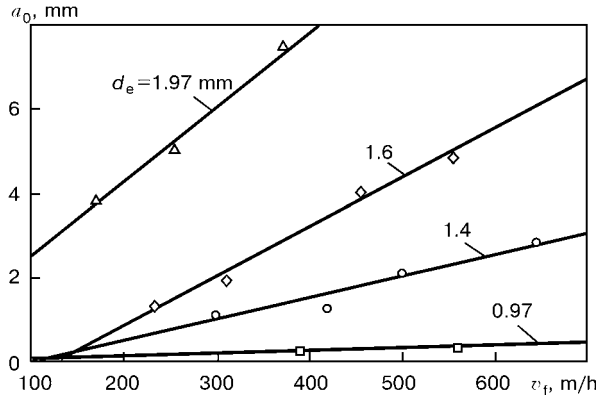

Figure 2. Dependence of constant constituent of penetration depth a_0 on electrode wire feed rate at its different diameters

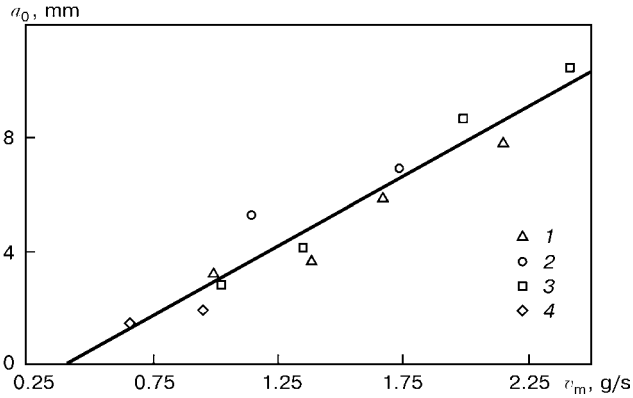

Figure 3. Relationship of value a_0 and mass rate of electrode wire feed for d_e = 1.0 (*1*), 1.4 (*2*), 1.6 (*3*) and 2.0 (*4*) mm

wire feed (by mass) v_m and welding speed v_w were used as independent variables for calculation of a depth of penetration.

Coming from the classical conceptions about the laws of product penetration and experimental data obtained, the following form of unknown formula for calculation of the penetration depth was preset

$$a = b_0 + b_1 v_m + b_2 U_a + b_3 v_w, \quad (1)$$

where a is the depth of penetration, mm; b_0, b_1, b_2 and b_3 are the empiric coefficients.

To determine the values of coefficients of equation (1) using method of a least-square method the linear relationships $a = f(U_a, v_w)$ were constructed at fixed values d_e and v_f, one of which is presented in Figure 1. At zero values U_a and v_w the obtained plane intersects the axis of predicted values in point a_0, whose value is different in each case, but dependent linearly on the electrode wire diameter and rate of its feeding (Figure 2).

To determine value a_0, it was suggested to consider its dependence not on the linear rate of wire feed v_f, but on its mass rate of feeding v_m (Figure 3). It was established that a_0 does not almost depend on diameter and increases with increase in v_m. Using the linear approximation the following relationship was obtained:

$$a_0 = -2.04 + 4.95 v_m. \quad (2)$$

Thus, we determined the values of coefficients b_0 and b_1 from (1): b_0 = 2.04 mm, b_1 = 4.95 mm·s/g.

Substituting b_0 and b_1 into equation (1), the values of coefficients b_2 and b_3 for different v_w were determined by experimental data using a least-squares method. Coefficients b_2 and b_3 can be described by the following relationships:

$$b_2 = -1.5 \cdot 10^{-4} v_w^2 + 6.1 \cdot 10^{-3} v_w - 4.68 \cdot 10^{-2}; \quad (3)$$

$$b_3 = \frac{6.4 \cdot 10^{-3} v_w^2 - 0.25 v_w + 3.72}{v_w} + \frac{6.8 \cdot 10^{-3} v_w^2 + 0.52 v_w - 15.41 - \dfrac{115.5}{v_w}}{v_w} v_m. \quad (4)$$

Determination of all the coefficients of equation (1) allowed the unknown relationship to be described with a sufficient accuracy for the practical purposes (coefficient of correlation with experimental data is 0.92). The obtained model is non-linear as regards to welding condition parameters (Figure 4).

The appearance of a region of growth of the penetration depth with welding speed increase contradicts some existing models of calculation of the penetration depth. However, this result is confirmed by investigations in the field of effect of liquid layer thickness under the arc on the penetration depth [6, 7].

Growth in penetration depth with increase in welding speed in a definite range is explained by the

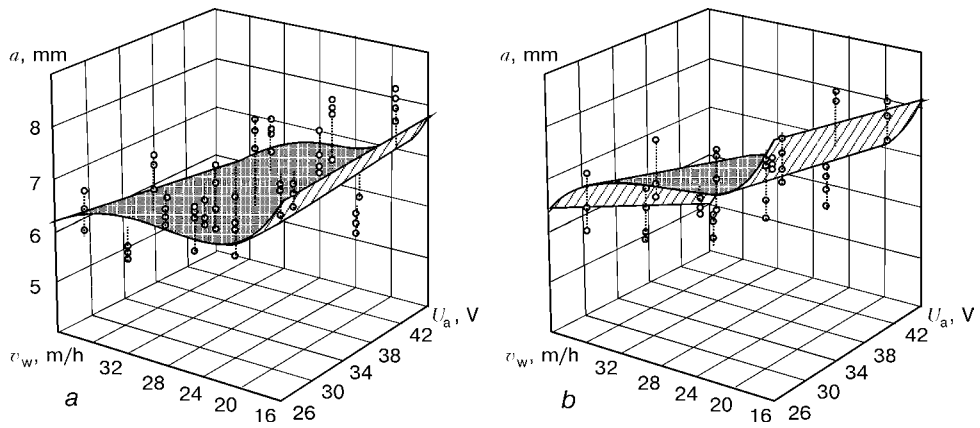

Figure 4. Dependence of penetration depth on arc voltage and welding speed: *a* — d_e = 1.6 mm, v_f = 2.4 g/s; *b* — d_e = 1.97 mm, v_m = 2.5 g/s (○ — experimental data)

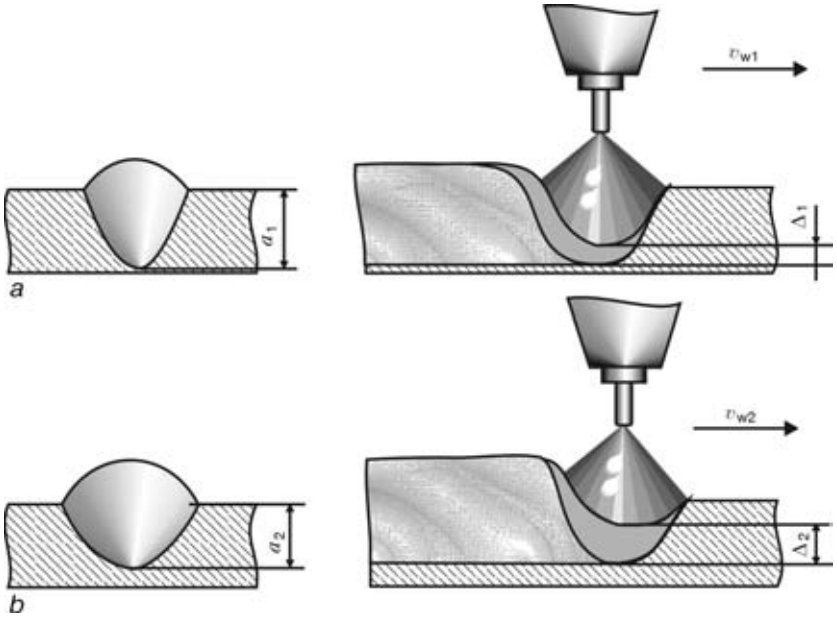

Figure 5. Effect of thickness of a liquid layer Δ under the arc on depth of penetration in changing welding speed ($v_{w1} > v_{w2}$)

fact that the pool molten metal is forced out by the arc pressure in a tail part and has no time to flow under the arc due to a natural mass. Thus, the arc energy is consumed mainly for melting the parent metal, but not for overheating the molten metal (Figure 5).

The model obtained was compared with the known Akulov's model. Comparison was made for d_e = 1.4, 1.6 and 2.0 mm at different parameters of the welding conditions. The conformity of results of calculations to experimental data was used as a criterion of evaluation of accuracy of the calculation models.

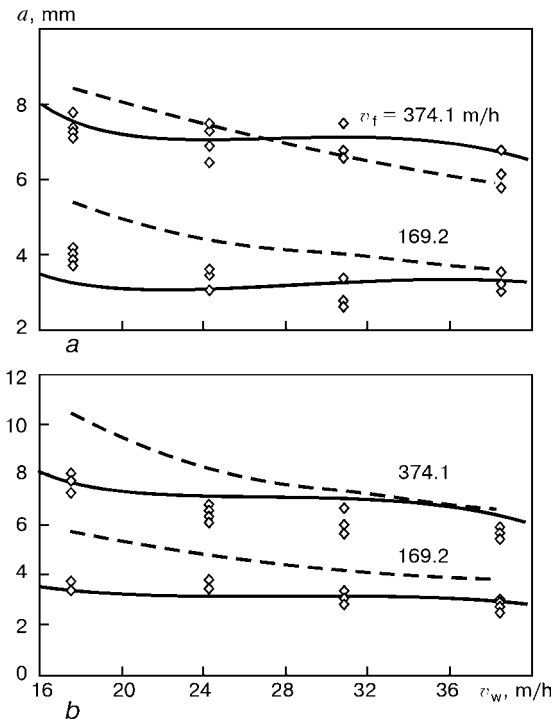

Figure 6. Dependence of penetration depth on welding speed for d_e = 2.0 mm and U_a = 30 (*a*) and 40 (*b*) V (solid curves — result of calculation by the model obtained, dashed curves — by the Akulov's model)

For clarity of representation the results of comparison were given in the form of graphs of dependences of penetration depth on welding speed at fixed values d_e, v_f, U_a. The behaviour of calculation models at different rates of electrode wire feed speed and values of arc voltage for d_e = 2.0 mm is shown in Figure 6.

As is seen in Figure 6 the dependence of penetration depth on welding speed, corresponding to the Akulov's model, has a form of a hyperbola. Non-adequate growth of penetration depth at small values v_w and tendency to some non-zero value at high welding speeds can be considered as a drawback of this description.

Calculations, performed using the Akulov's model, have a good correlation with experimental data within the range of welding speeds from 28 to 40 m/h. Increase in voltage and decrease in rate of the electrode wire feed leads to the error increase.

It can be concluded that the Akulov's model reflects adequately the real values of penetration depth only in rigid ranges of limits by welding speed, electrode wire feed speed and arc voltage.

Analysis of data of calculation using the model developed shows that at low welding speeds the arc voltage does not almost influence the depth of penetration. With increase in v_w the degree of U_a effect is increased, and here, with increase in arc voltage the depth of penetration is decreased. Increase in v_w leads firstly to an abrupt decrease in the depth of penetration and then to its little increase. At high welding speeds the depth of penetration begins to decrease again.

The model obtained makes it possible to conclude that at a definite arc voltage and/or welding speed the depth of penetration becomes equal to zero that is especially important in calculation of the welding condition parameters.

If to introduce the known dependence v_m on welding current I_w, stickout h_e, diameter and chemical composition of welding wire [5] to the formula (1), then the obtained formula can be used for the solution of a reverse problem, i.e. the welding current can be calculated by a preset value of depth of penetration, diameter and stickout of welding wire. So, the engineering calculations of the welding conditions can be simplified significantly.

The regularities, established during investigations, can be used in the development of automated systems of control of the depth of penetration of products during surfacing (welding) to account the effect of other materials of electrode wires and products, shielding media and conditions of surfacing (welding) on the penetration depth. For example, they can be used for description of welding process with edge preparation and with a gap between the elements welded.

CONCLUSIONS

1. The model has been developed for calculation of the penetration depth in CO_2 surfacing (welding) of butt joint with a square edge preparation.

2. Functional relationship between the depth of penetration and surfacing (welding) condition parameters is defined and described mathematically.

3. The empiric formula obtained provides the highest simplicity and accuracy of engineering and scientific calculations of penetration depth in a mechanized surfacing (welding) and allows its express evaluation.

1. Akulov, A.I., Belchuk, T.A., Demyantsevich, V.P. (1977) *Technology and equipment of fusion welding*. Moscow: Mashinostroenie.
2. Dubovitsky, S.V., Sergatsky, G.I., Kasatkin, O.G. (1980) Optimization of CO_2 welding conditions. *Avtomatich. Svarka*, **12**, 30–35.
3. Rykalin, N.N., Beketov, A.I. (1967) Calculation of thermal cycle of near-weld zone by contour of weld pool. *Svarochn. Proizvodstvo*, **9**, 22–25.
4. Krivosheya, V.E. (1981) Modelling of welding processes. In: *Automation of welding manufacturing in the light of decisions of XXVI Congress of CPSS*. Leningrad: F.E. Dzerzhinsky LDNTP.
5. Varukha, E.N., Doktorsky, R.Ya. (1991) Calculation of electrode fusion rate in mechanised welding. *Svarochn. Proizvodstvo*, **6**, 33–35.
6. Leshchinsky, L.K., Pavlov, I.V. (1975) Thickness of liquid interlayer under arc during hardfacing with strip electrode and wire. *Avtomatich. Svarka*, **3**, 75–76.
7. Chernychev, G.G., Rybachuk, A.N. (1969) About thickness of liquid interlayer under arc. In: *Technology and automation of welding and brazing processes*. Moscow: Mashinostroenie.

PECULIARITIES OF MELTING AND SOLIDIFICATION OF 20KhGS TYPE DEPOSITED METAL ALLOYED WITH PHOSPHORUS

Yu.M. KUSKOV, I.I. RYABTSEV, L.K. DOROSHENKO and **V.G. VASILIEV**
The E.O. Paton Electric Welding Institute, NASU, Kyiv, Ukraine

Processes of melting and solidification of deposited metal of 20KhGS type alloyed with 0.1–2.4 % of phosphorus were investigated using a method of a differential thermal analysis. It was established that phosphide eutectics, being hazardous from the point of view of susceptibility to hot cracks, are appeared in the deposited metal of this type at phosphorus content of more than 1 %.

Key words: *deposited metal, alloying with phosphorus, phosphide eutectics, solidification of deposited metal, differential thermal analysis*

In most cases the phosphorus is considered to be an undesirable impurity in steel. In solidification of steel ingots an intracrystalline liquation of phosphorus was observed leading to reduction in ductility and impact strength, at lower temperatures in particular. Phosphorus is one of the elements which is responsible for the steel temper brittleness [1]. Similarly it influences the properties of weld metal [2]. For this reason, its content in steels and weld metal is limited usually by 0.03 %.

However, there are steels and cast irons in which phosphorus is used as an alloying element. According to data of [3], phosphorus hardens steel at its content up to 0.6 %. In parallel with carbon and molybdenum it is one of the highest hardeners of as-normalized steel.

Phosphorus mass fraction of 1 % and more has a favourable influence on wear-resistance and antifriction properties of Fe-base alloys [4, 5]. Here, the phosphides of iron and some alloying elements in metal-to-metal friction fulfil the role of a dry lubrication [6]. Phosphorus has also a positive effect on the steel fluidity. As is follows from article [7], the phosphorus, as a surface-active substance, promotes the decrease in surface tension of a liquid iron, thus leading to its complete spreading over a hard substrate.

As the phosphorus has a positive effect on antifriction properties and steel fluidity, its use as an alloying element in some surfacing materials can be

Table 1. Chemical composition and hardness of deposited metal samples being investigated

Number of alloy sample	Mass fraction of elements in deposited metal, %					Hardness of deposited metal, HV
	C	Mn	Si	Cr	P	
I	0.22	1.15	0.88	1.10	–	220
II	0.23	1.13	0.93	1.20	0.11	229
III	0.23	1.23	0.98	1.15	0.31	229
IV	0.22	1.20	0.90	1.25	0.57	321
V	0.24	1.14	0.96	1.23	1.00	320
VI	0.23	1.08	0.90	1.18	1.28	341
VII	0.21	1.20	1.00	1.27	1.98	363
VIII	0.22	1.18	0.92	1.21	2.38	413

Table 2. Temperature of melting and solidification of test alloys

Number of alloy sample	Temperature of melting and solidification of test alloys, °C			
	Matrix		Eutectic	
	Melting	Solidification	Melting	Solidification
I	1440	1500	Eutectic was not observed	
II	1430	1525	Same	
III	1370	1460	»	»
IV	1380	1470	»	»
V	1460	1480	»	»
VI	1360	1460	990	920
VII	1360	1400	1000	920
VIII	1300	1370	980	900

promising, for example, in flux-cored or solid wires, providing deposited metal of type of steels 18KhGS and 30KhGSA. These wires are used widely in different branches of industry for restoration and hardening of parts operating under the conditions of metal-to-metal friction [8].

The application of phosphorus as an alloying element in the surfacing materials can prevent the formation of fusible phosphide eutectics which increase the susceptibility of steels to hot cracks in welding and surfacing.

Taking into account the possible negative effect of phosphide eutectics on the susceptibility of the deposited metal to hot cracks, the processes of melting and solidification of samples of the deposited metal of 20KhGS steel type with a different content of phosphorus were investigated (Table 1).

Processes of melting and solidification of test samples of deposited metal were studied using a method of differential thermal analysis (DTA) in unit VDTA-8M. Test samples were cut from 4–6th layer of metal deposited by flux-cored wires, whose charge contained different amounts of phosphorus in the form of a ferrophosphorus. The work [9] shows that with use of DTA method it is possible to record even small

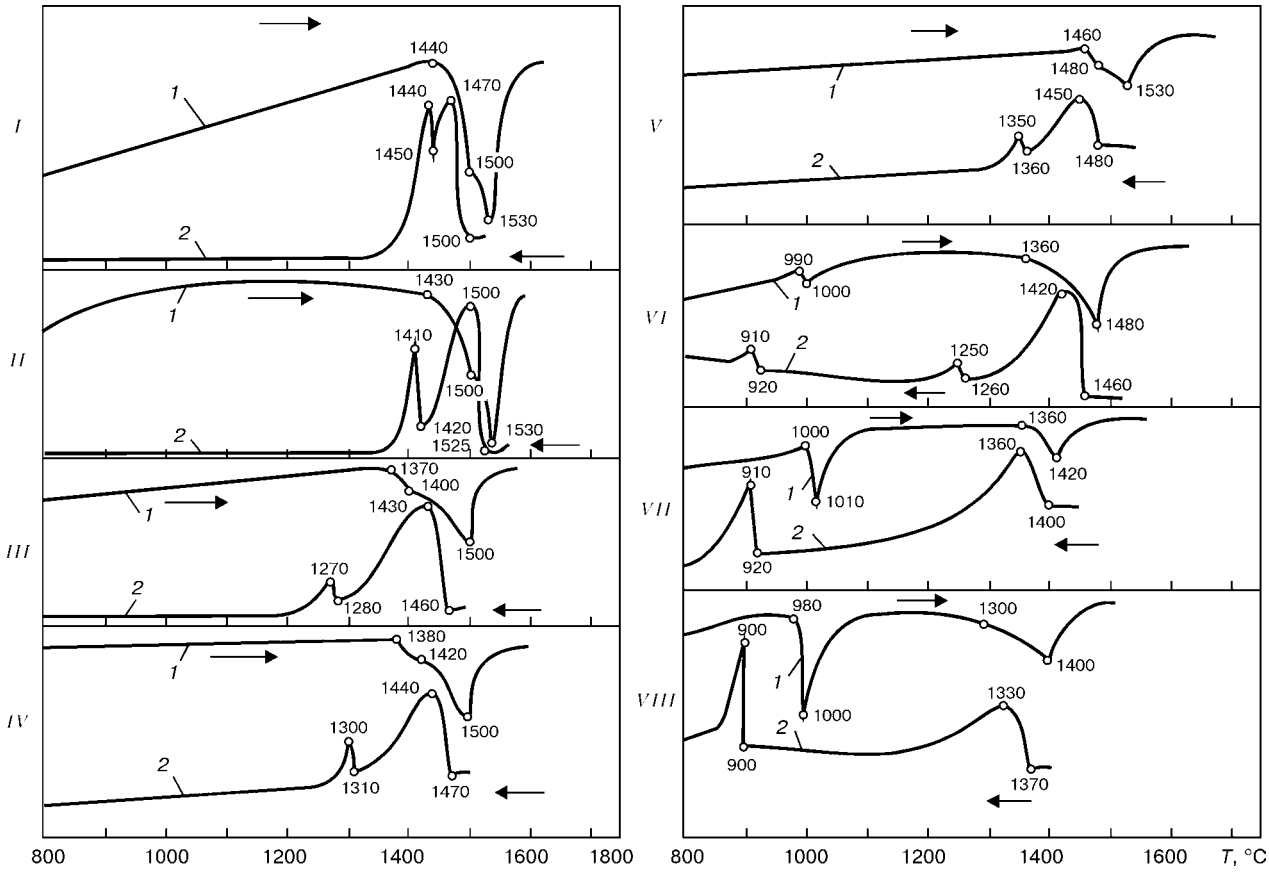

Figure 1. Differential thermal curves of heating (*1*) and cooling (*2*) of samples of steel 20KhGS with different content of phosphorus, %: *I* — without phosphorus; *II* — 0.11; *III* — 0.31; *IV* — 0.57; *V* — 1.0; *VI* — 1.28; *VII* — 1.98; *VIII* — 2.38

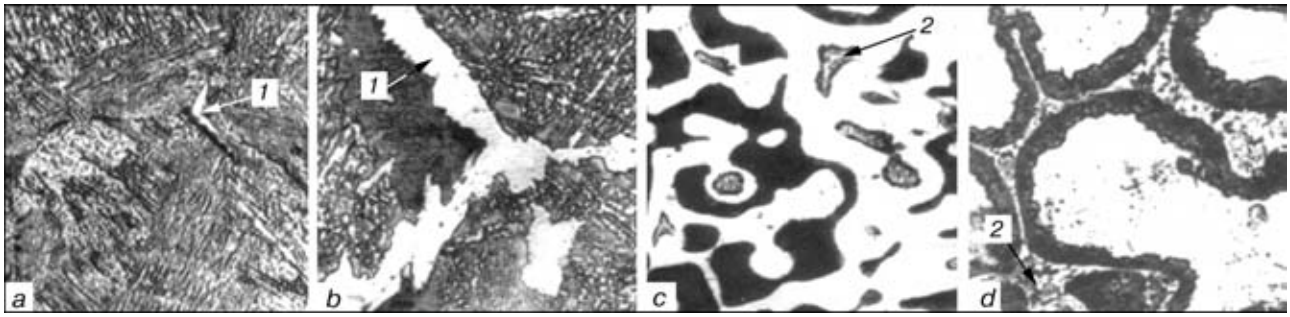

Figure 2. Microstructure of steel 20KhGS with different content of phosphorus, %: *a* — without phosphorus; *b* — 0.11; *c* — 1.28; *d* — 1.98; *1* — ferrite; *2* — phosphide eutectic (electrolytic etching in 20 % solution of chromous acid) (×500)

changes in a phase composition of material, for example, presence or absence of eutectics.

Heating and cooling of samples of the deposited metal were performed in helium at 0.05 MPa pressure at 80 °C/min rate using an aluminium oxide crucible.

In case of use of the DTA method the values of temperature of beginning and end of melting and solidification of materials examined are determined from curves of their heating and cooling using a graduation graph of melting and solidification of the reference sample under the same conditions. A sample of pure tungsten was used in experiments as a reference sample. Mass of test and reference samples was about (1 ± 0.1) g.

Stages of phase transformations, melting and solidification of the alloy are indicated by deviation from a straight running of curves of heating or cooling, thus proving the proceeding of endo- and exothermal processes. Degree of these deviations depends on chemical composition of the material being examined.

Figure 1 shows curves of heating and cooling of samples of test compositions of the deposited metal, and Table 2 indicates the temperatures of their melting and solidification. According to the DTA method the beginning of melting is determined from the curve of heating, and the temperature of the beginning of solidification — from the cooling curve.

As the experiments showed (Figure 1, samples *I*–*V*, curves *1*) two bends are observed on the curves of heating in a high-temperature region at phosphorus content up to about 1.0 % in the deposited metal of 20KhGS steel type. Analysis of state diagrams of steels of this class [10–12] could explain the nature of proceeding transformations. First bends on curves of heating samples (sample *I*, curve *1*, 1440–1500 °C; sample *II*, curve *2*, 1430–1500 °C; sample *III*, curve *1*, 1370–1400 °C; sample *IV*, curve *1*, 1380–1420 °C; sample *V*, curve *1*, 1460–1480 °C) are associated with the beginning of melting of a solid solution and a probable proceeding of a peritectic reaction. The second bend (at higher temperatures) indicates melting of the solid solution remnants.

At a high content of phosphorus (Figure 1, samples *VI*–*VIII*, curves *1*) the bends are observed firstly on curves of heating, which correspond to melting of a phosphide eutectic at 980–1000 °C and then the alloy matrix is melted under the higher temperature conditions. At such content of phosphorus the nature of melting of the alloy matrix is changed (curves of melting have only one bend). It should be noted that with increase in phosphorus content an amount of the phosphide eutectic is increased that is proved by an increase in peaks on the curves of heating corresponding to melting of the phosphide eutectic.

The first (high-temperature) peak on the curves of cooling steels with a relatively small content of phosphorus corresponds to the beginning of solidification of the solid solution, while the second — to a peritectic reaction, which according to [10] is proceeding almost at constant, but different for each of the test materials, values of temperature (Figure 1, samples *I*–*V*, curves *2*). For these steels the solidification is started from the formation of α-solid solution. The peritectic reaction results in a formation of the α-phase.

At phosphorus content 1.98 and 2.38 % one peak was observed on the curves of cooling in the high-temperature region (Figure 1, samples *VII, VIII*, curves *2*), that proves the absence of phosphorus of a peritectic transformation in steel. Solidification of matrix of these steels occurs directly after formation of γ-phase.

It can be concluded from the data of Table 2 that with increase in phosphorus content the values of temperature of beginning of melting and solidification of steel 20KhGS are prone to decrease.

Metallographic examination of 20KhGS steel samples with a different content of phosphorus was performed. The deposited metal of 20KhGS steel type without phosphorus has a bainitic structure with a small amount of ferrite (Figure 2, *a*). Adding of phosphorus as an element-ferritiser increases the amount of the ferritic phase (Figure 2, *b*). The further increase in phosphorus content leads to the change in ratio between these phases, however the areas of the phosphide eutectic in the structure of these steels were not observed.

The appearance of the phosphide eutectic was observed at 1.28 wt.% of phosphorus (Figure 2, *c*). These data confirm the DTA results: the first peak corresponding to melting of a phosphide eutectic was observed on a curve of heating sample of this steel (Figure 1, sample *VI*, curves *1, 2*). At phosphorus content of about 2.0 % and more a complete network of the phosphide eutectic, which fringes the grains of

the alloy matrix, is formed in the steel 20KhGS structure (Figure 2, *d*).

Thus, it was stated during investigations using DTA method that the phosphide eutectics are appeared in the deposited metal of 20KhGS type at phosphorus content of more than 1 % and they are hazardous from the point of view of susceptibility to hot cracks. This fact should be taken into consideration in the development of surfacing materials designed for restoration and strengthening of parts operating under the conditions of metal-to-metal friction.

1. Muchnik, S.V. (1979) Chemistry and technology of phosphorus-containing alloys. Phosphorus-containing alloys. In: *Chemistry and technology of phosphides and phosphorus-containing alloys*. Kyiv: IPMS.
2. Alekseev, A.A., Yavdoshchin, I.R., Vojtkevich, V.G. et al. (1989) Influence of phosphorus on structure and properties of weld metal in welding of low-alloy steels. *Avtomatich. Svarka*, **4**, 7–10.
3. Spretnak, J.W. (1961) Phosphorus in metallurgy. Phosphorus and its compounds. In: *Technology, biological functions and application*. Vol. 2.
4. Kachko, M.O., Markovsky, E.A., Ilchenko, V.D. (1998) Antifriction alloys of iron with dry lubricant phases. *Metaloznavstvo ta Obrobka Metaliv*, **3**, 17–21.
5. Markovsky, E.A., Ilchenko, V.D., Butenko, L.I. et al. (1999) Influence of composition and structure of iron antifriction alloy on its wear resistance. *Protsessy Litia*, **2**, 60–64.
6. Bakfart, F.G., Daniel, S.G. (1967) New information about lubricants. In: *Proc. of Int. Conf. on Lubricants*, Washington, 1964. Moscow: Khimiya.
7. Samsonov, G.V., Panasyuk, A.D., Borovikova, M.S. (1977) Influence of phosphorus on adhesion of liquid metals to refractory joints. In: *Production, properties and application of phosphides*. Kyiv: Naukova Dumka.
8. Ryabtsev, I.A., Kondratiev, I.A. (1999) *Mechanised arc surfacing of metallurgical equipment parts*. Kyiv: Ekotekhnologiya.
9. Wendlandt, U. (1978) *Thermal methods of analysis*. Moscow: Mir.
10. Gulyaev, A.P. (1977) *Physical metallurgy*. Moscow: Metallurgiya.
11. Gudremon, E. (1960) *Special steels*. Moscow: Metallurgiya.
12. Khansen, M., Anderko, K. (1962) *Structures of binary alloys*. Moscow: Metallurgiya.

THERMAL COATINGS CONTAINING DRY LUBRICANTS FOR OPERATION UNDER CONDITIONS OF DRY FRICTION AND ELEVATED TEMPERATURES

A.Yu. TUNIK
The E.O. Paton Electric Welding Institute, NASU, Kyiv, Ukraine

Results of investigation of composite powders with dry lubricants of FeCr–TiC–Mo–C and Cr_2O_3–TiO_2–CaF_2 systems, as well as thermal coatings of a tribotechnical purpose, are presented. Conditions of thermal spraying are defined, providing dense coatings with a high adhesion and cohesion strength at a sufficiently uniform distribution of a dry lubricant across the section.

Key words: *thermal coatings, structure, phase transformations, dry lubricants, friction coefficient, wear resistance, friction without lubrication*

More than 80 % of funds, spent for the equipment repair, is used for the restoration of friction components. Their repair-free service life depends directly on the material selected and design of the components.

The important trend in the advanced engineering became the creation of antifriction materials which are capable to operate without lubrication, as its refusal simplifies significantly the design of machines, makes their maintenance easier, in particular, in the range of low and high temperatures, and increases the reliability.

One of the effective methods of solution of the above-mentioned problem is the use of protective coatings with antifriction properties. In this case a combined material is developed, which should combine the required strength properties of the base material and a high service life of external layer (coating) under conditions of effect of environment and contact loads.

The thermal spraying (TS) is a promising method of deposition of coatings with antifriction properties, whose peculiar feature is a feasibility of control of composition, structure and properties of the coating using different powder compositions in the form of mechanical mixtures or composite powders (CP) including metals, alloys, oxides, oxygen-free refractory compounds and dry lubricants (graphite, boron nitride, molybdenum disulphide, calcium fluoride, etc.) [1–3].

The article describes the investigations of CP, which include dry lubricants, and also results of development and study of multicomponent coatings from these powders of a tribotechnical purpose.

During investigations were used: metallography, microdurometry, X-ray diffraction phase analysis (XDPA), X-ray microanalysis (XMA), Auger-spectroscopy. Values of microhardness are an integral characteristic of the coating material, as it is impossible in some cases to measure microhardness of separate structural constituents due to their small sizes.

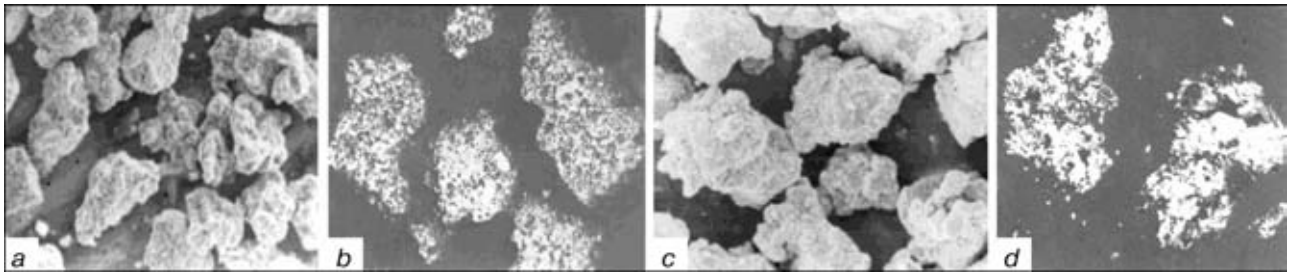

Figure 1. Appearance (*a, b*) (×300) and microstructure (*c, d*) (×400) of CP particles of FeCr–TiC–Mo–C (*a, b*) and Cr_2O_3–TiO_2–CaF_2 systems (*c, d*)

Information about phase composition and uniformity of distribution of the dry lubricant over the coating volume is obtained by comparison of the results of XDPA and XMA.

The examination of antifriction properties of the coatings were made in a tribotechnical complex, which is an analogue to a foreign «pin-on-disk» according to ASTM 99–90. Graphite and calcium fluoride were selected as dry lubricating materials. Graphite is the traditional material with a lamellar structure. It is not melted in the TS conditions, it sublimates easily and burns out, therefore, it can be added to the coating volume only in the CP composition [4]. Calcium fluoride is the corrosion-resistant material designed for operation at elevated temperatures [5, 6]. It is the most technological dry lubrication for deposition using TS method as it is melted at 1418 °C without decomposition and not subjected to active oxidizing with the formation of undesirable products and can be used both in the composition of mechanical mixtures and in the form of CP.

CP, whose composition has dry lubricants, were manufactured using a method of a self-spreading high-temperature synthesis. Table 1 presents compositions of these materials and their phase composition.

In CP of FeCr–TiC–Mo–C system, containing graphite as a dry lubricant, FeCr plays a role of a plastic component, TiC is a refractory hard addition, molybdenum was added for increasing adhesion strength. In CP of Cr_2O_3–TiO_2–CaF_2 system, containing CaF_2 as a dry lubricant, oxides of chromium and titanium played a role of a wear-resistant matrix. In addition, titanium oxide was added for making the composition plastic. The appearance and microstructure of CP particles are presented in Figure 1.

Coatings were deposited by methods of detonation (DS) and supersonic air-gas plasma spraying (SAGPS), and also plasma spraying using argon-hydrogen plasma jet (PS-Ar+H_2). TS conditions of coating deposition are given in Table 2.

Table 1. Phase composition of composite powders

Composition of material sprayed	*Results of XDPA**
15FeCr–70TiC–3Mo–12C	TiC, FeCr, C, Mo
40Cr_2O_3–45TiO_2–15CaF_2	TiO_2 (rutile), Cr_2O_3, CaF_2, Cr (traces), Ti (traces)

*Here and in Tables 3 and 4 the phases and separate elements are arranged in a sequence of reducing intensity of reflection of X-rays.

Examination of coating from CP of FeCr–TiC–Mo–C and Cr_2O_3–TiO_2–CaF_2 systems produced by the above-mentioned methods showed the following. Detonation coatings of FeCr–TiC–Mo–C system are dense, without spallings, have a good adhesion and possess a laminar structure (Figure 2, *a*), which consists of particles of white (*1*) and grey (*2*) colour, and also inclusions of a dry lubricant (*3*) (black colour). Structural constituent is white, having a form of lamellas and particles of an oval shape, and consists of ferrochrome with inclusions of fine-dispersed particles TiC (Table 3). The second structural constituent is dark. These are titanium oxides alloyed with iron, molybdenum and chromium. The presence of the above-mentioned phases is confirmed by the results of XDPA and XMA.

Coatings deposited using SAGPS are differed from those of DS by the more non-homogeneous and coarse-grained structure, but with a sufficiently uniform distribution of graphite inclusions (Figure 2, *b*). As to the adhesion strength the first coatings are not inferior to the second ones, however, in this case a scattering of microhardness values is observed due to higher degree of structure non-homogeneity.

Both in DS and SAGPS of CP of FeCr–TiC–Mo–C system in air a great oxidizing of titanium carbide is occurred with the formation of oxide phases. The part of the titanium carbide is remained both in the form of grains (5–10 μm size) in a metallic (ferrochrome) matrix and also in the form of fine-dispersed precipitations in oxide phase.

In deposition of the above-mentioned composition using argon-hydrogen plasma jet the new phases are not formed, if the appearance of traces of titanium oxide is not taken into account. The coating is characterized by a high degree of porosity and non-homogeneity (Figure 2, *c*). As to hardness and adhesion strength with a base material it is not inferior to coatings deposited by SAGPS and DS. According to the results of metallographic examinations the amount

Table 2. Thermal spraying conditions

Method of spraying	*Operating gas*	*Gas consump. m^3/h*	*Current, A*	*Voltage, V*	*Distance, mm*
DS	C_3H_8	0.5			100
	O_2	2.0			
SAGPS	Air	12	200–300	300–450	230
	P = 0.4 MPa				
PS-Ar+H_2	Ar	2.3	450–500	60–65	130
	H_2	0.1			

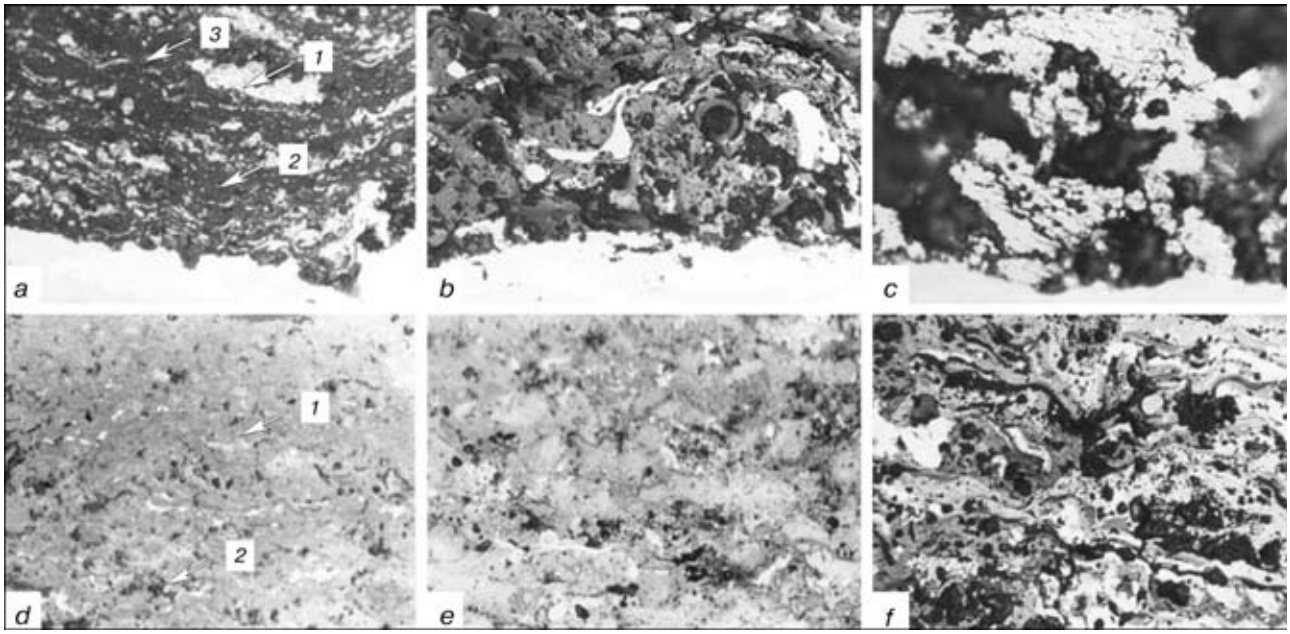

Figure 2. Effect of methods of spraying on structure of coatings from CP of FeCr–TiC–Mo–C (*a–c*) and Cr_2O_3–TiO_2–CaF_2 (*d–f*) systems: *a, d* — DS; *b, e* — SAGPS; *c, f* — PS-Ar+H_2 (×400)

of a dry lubricant in coatings is about 17 vol.% as compared to 25 vol.% (12 wt.%) in the initial powder. It was established during examination of fracture surface of detonation coatings using Auger-spectroscopy that about 30 at.% of carbon is bound into titanium carbide, while the rest is the fraction of a free graphite. Metallographic analysis and Auger-spectroscopy testify about the fact that during spraying of CP of FeCr–TiC–Mo–C system the losses in carbon are observed. For DS they are 30–32 % on average.

In DS of coatings from CP, based on titanium and chromium oxides with calcium fluoride, the dense coatings are formed with the highest adhesion strength as compared with other methods in which a complex titanium-chromium oxide $Ti_2Cr_2O_7$ (*1*), integrated oxides Ti–Cr–Ca–O (*2*) and TiN are observed, thus proving the proceeding processes of interphase interaction both in particles themselves and also between the components of the material sprayed and oxygen of the ambient air (Figure 2, *d* and Table 3).

In SAGPS of powders Cr_2O_3–TiO_2–CaF_2 the coatings are also formed representing an oxide matrix in which inclusions of a dry lubricant of black colour is located (Figure 2, *e*). The same as in DS, the coatings, except initial phases Cr_2O_3, TiO_2 and CaF_2, have also $Ti_2Cr_2O_7$, complex oxides Ti–Cr–Ca–O and also the new oxide $TiCrO_3$ (see Table 3). The coating is inferior as to the quality to the DS coating because the pores and spallings are observed in it, thus proving the decrease in its cohesion strength.

In plasma spraying of the same CP using Ar+H_2 as a plasma gas the coatings of higher hardness are formed (Table 3). Structure of the coating is dense,

Table 3. Characteristic of coatings deposited by thermal spraying

Composition of material sprayed	*Method of coating deposition*	σ_{adh}, *MPa*	*HV, GPa*	*Phase composition of coatings (from results of XDPA and XMA)*
15FeCr–70TiC–3Mo–12C	DS	42.4–45.5	5.71–6.16	TiC, FeCr, TiO_2, Ti_3O_5, complex oxides of system Ti–Cr–Fe–O, C, Mo (traces)
	SAGPS	36.5–39.5	2.21–7.07	TiC, Ti_3O_5, FeCr, complex oxides of system Ti–Cr–Fe–O, C, Cr
	PS-Ar+H_2	<12.0	2.87–3.60	TiC, FeCr, C, Ti_3O_5 (traces)
$40Cr_2O_3$–$45TiO_2$–$15CaF_2$	DS	39.5–42.5	2.94–4.90	Cr_2O_3, $Ti_2Cr_2O_7$, complex oxides of system Ti–Cr–Ca–O, TiO_2, CaF_2, Cr, TiN
	SAGPS	35.0–39.0	2.86–4.73	Cr_2O_3, TiO_2, $TiCrO_3$, $Ti_2Cr_2O_7$, TiO, complex oxides of system Ti–Cr–Ca–O, CaF_2
	PS-Ar+H_2	20.0–29.5	4.82–7.42	Cr_2O_3, $TiCrO_3$, $Ti_2Cr_2O_7$, TiO, complex oxides: Ti–Cr–Ca–O, CaF_2, Cr

Table 4. Phase composition of coating surface after tribotechnical tests at 400 °C

Composition of material sprayed	*Result of XDPA*
15FeCr–70TiC–3Mo–12C	TiO_2, TiC, FeCr, C, Mo (traces), Ti_3O_5 (traces)
$40Cr_2O_3$–$45TiO_2$–$15CaF_2$	Cr_2O_3, TiO_2, $Ti_2Cr_2O_7$, CaF_2, $Ca_9Cr_6O_{24}$, TiN (traces)

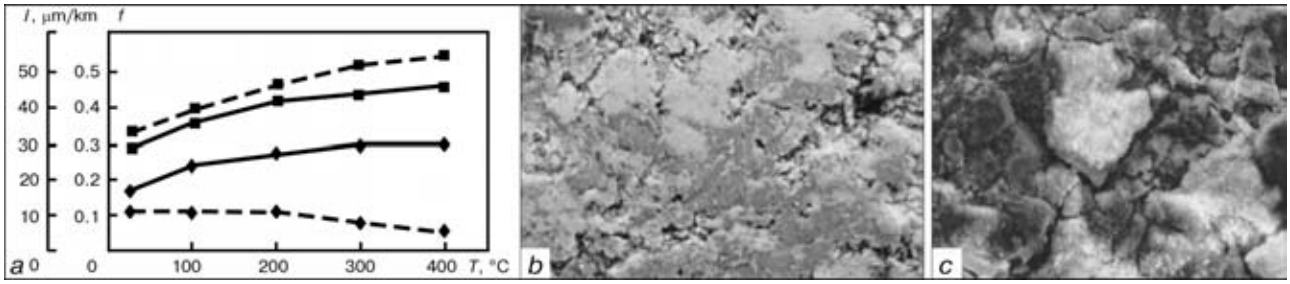

Figure 3. Dependence of friction coefficient f (solid curve) and wear I (dashed curve) on temperature (a) and appearance of friction paths of coatings from CP of Cr_2O_3–TiO_2–CaF_2(■, b) and FeCr–TiC–Mo–C (◆, c) systems (×750)

lamellar, the internal structure of lamellas is also characterized by heterogeneity (Figure 2, *f*). Except other oxides, the titanium oxide TiO was observed in the coating. Flakes-like inclusions of a dry lubricant (black colour) were distributed across the section of coating quite uniformly.

Integrated investigations of coatings resulted in determination of TS conditions providing dense coatings with a high adhesion and cohesion strength at a sufficiently uniform distribution of a dry lubricant across the section. From the point of view of coating quality (density, homogeneity of structure and maximum strength of adhesion with the base material) the coatings produced by DS method from powders of FeCr–TiC–Mo–C and Cr_2O_3–TiO_2–CaF_2 systems were selected for further tribotechnical tests under the conditions of a dry friction.

The investigations of antifriction properties of coatings were performed using the following parameters: T = 20–400 °C, P = 30 MPa, v = 0.5 m/s, 1000 m path of friction, Hertz's contact.

The test procedure was checked on samples at room temperature. It was established that the time of fitting surfaces of friction did not exceed 3 min after the test beginning. Results of tribotechnical tests of coatings deposited by TS from powders Cr_2O_3–TiO_2–CaF_2 and FeCr–TiC–Mo–C at elevated temperatures are presented in Figure 3, *a*. After the tests the phase composition (Table 4) and friction surface of coatings were studied (Figure 3, *b, c*).

With temperature increase from 20 to 200 °C the increase in friction coefficient at wear stabilizing was observed in coating FeCr–TiC–Mo–C. At further increase in temperature up to 400 °C the friction coefficient takes a constant value, not exceeding 0.3, while the wear is stabilized and somewhat decreased.

Photos of friction surfaces made with the help of the optical microscope and given in Figure 3 are typical of the following processes: smoothing of surface (most visible in edges of pores) accompanied by destroying of roughness ripples; filling of micropores with particles of wear, separated from the coating and mating body. Fracture of microprojections occurs until setting of an equilibrium roughness at which the friction process is characterized by optimum parameters for the given conditions of work. After examination of the friction path surface using XDPA method the formation of titanium oxides TiO_2, Ti_3O_5 and graphite film, protecting the base metal from environment effects and also the significant increase in values of antifriction characteristics of a tribopair was observed.

For coating Cr_2O_3–TiO_2–CaF_2 the noticeable increase in friction coefficient (up to 0.45) and wear (up to 55 μm) within the entire temperature range is occurred, being due to the fact that with temperature increase the complex oxides $Ti_2Cr_2O_7$ and $Ca_9Cr_6O_{24}$ are formed, cohesion strength is reduced, and this leads to spalling of the coating material and formation of a network of cracks (Figure 3, *c*). At the same time, this phenomenon was not observed in system FeCr–TiC–Mo–C containing a plastic component FeCr.

CONCLUSIONS

1. It was established that the quality of antifriction coatings, their structure, phase composition, hardness and tribotechnical properties depend on the method and conditions of TS, and also composition and structure of initial powder, size of particles.

2. In thermal spraying of CP the processes of interphase interaction of particles of the powder sprayed with environment and inside the particles themselves between its constituents are developed. In CP of FeCr–TiC–Mo–C system the oxidizing of TiC and FeCr and partial burning out of a dry lubricant was observed. In powder Cr_2O_3–TiO_2–CaF_2 the formation of complex oxides also inside the particles themselves is occurred.

3. Tribotechnical properties of TS with dry lubricants are defined by their phase composition and structure. Coatings from powder FeCr–TiC–Mo–C are characterized by the highest characteristics of antifriction properties both at room and high temperatures as they represent a quite plastic matrix consisting of oxide of titanium and ferrochrome strengthened with hard inclusions of the titanium carbide with uniformly distributed graphite across section which is used as a dry lubricant. The mentioned coatings are superior to the coatings from powder Cr_2O_3–TiO_2–CaF_2 consisting only from wear-resistant oxide phases with inclusions CaF_2 which are characterized by the lower cohesion strength.

1. Fedorchenko, I.M., Pugina, L.I. (1980) *Composite sintered antifriction materials*. Kyiv: Naukova Dumka.
2. (1997) *Encyclopedia of inorganic materials*. Kyiv: Ukr. Sov. Entsikl.
3. Braithwite, E.R. (1967) *Solid lubricants and antifriction coatings*. Moscow: Khimiya.
4. Vajnstejn, V.E., Troyanovskaya, G.I. (1968) *Dry-film lubricants and self-lubricating materials*. Moscow: Mashinostroenie.
5. Fedorchenko, I.M., Bondar, V.T., Shevchuk, Yu.D., et al. (1989) Influence of calcium fluoride on antitear layer in powder antifriction materials. *Trenie i Iznos*, **1**, 97–103.
6. Dzneladze, D.I., Shchegalyova, R.P., Golubeva, L.S. et al. (1978) *Powder metallurgy of steels and alloys*. Moscow: Metallurgiya.

FUSION WELDING OF TITANIUM TO STEEL (REVIEW)

L.S. KIREEV and **V.N. ZAMKOV**
The E.O. Paton Electric Welding Institute, NASU, Kyiv, Ukraine

Literature on fusion welding of titanium to steel by the electron beam and argon-arc tungsten-electrode methods is reviewed. It is shown that titanium cannot be directly joined to steel due to formation of brittle intermetallic phases. Therefore, the technology was suggested for joining these materials through intermediate barrier inserts. The use of intermediate inserts can be avoided by joining titanium to steel in a solid-liquid state. This joining is performed by projection resistance welding with programmed internal splashing and subsequent forging of the joining zone.

Key words: *fusion welding, electron beam welding, argon-arc tungsten-electrode welding, projection resistance welding, solid-liquid state joining, titanium, steel, intermetallic phases, intermediate barrier inserts, vanadium carbides, titanium–steel interface*

The problem of making titanium-steel welded structures has attracted attention of investigators since the end of the 1950s, with the beginning of commercial utilisation of titanium in industry. The interest was caused, on the one hand, by unique properties of titanium and alloys on its base and, on the other hand, by high cost of titanium semi-finished products. It was expected that the use of elements of titanium (where it was required by service conditions of a part) and steel in one structure would allow improvement of performance and cost effectiveness of this structure. However, all attempts to perform direct welding of titanium to steel failed to give positive results [1, 2] because of cracks formed in the welds. Investigations showed that they were caused by brittle intermetallic phases formed in fusion of titanium with iron and the majority of steel alloying elements [3], and that titanium could be joined to steel only through intermediate inserts well weldable to both metals. The first substantiation of selection of materials for the intermediate inserts was given in study [4].

Titanium forms continuous solid solutions with zirconium, hafnium, vanadium, niobium, molybdenum and tantalum. Therefore, it can be satisfactorily welded to these metals [4–7]. In turn, out of this group of metals, only vanadium can be directly joined to steel. However, ductility and toughness of metal of such welds depend upon the percentage of vanadium, iron and other steel alloying elements they contain. First of all, this is attributable to the fact that in the Fe–V system, at a weight content of vanadium ranging from 22 to 65 %, the brittle σ-phase is formed in metal [7]. The negative effect on ductility of the vanadium-steel welds is exerted by carbon (because of formation of vanadium carbide) [8] and steel alloying elements, such as nickel, manganese, silicon, etc., if their weight content of the weld is in excess of 18.0, 2.8 and 1.6 %, respectively [9]. To ensure satisfactory properties of the titanium-vanadium welds, they should have a certain titanium to vanadium ratio to form a thermally stable single-phase β-structure.

It should be once more emphasised that vanadium is the only metal which can be directly joined to steel by the fusion welding method. In all other cases there should be an intermediate insert between titanium and steel, consisting of two metals, e.g. tantalum or niobium and copper or copper-based alloys [4].

Two technologies are used at present to make titanium-steel structures by the fusion welding method. According to the first technology, welding is performed using multilayer inserts prefabricated by a pressure joining method (explosion, combined rolling, etc.). Metals that are at the ends of such inserts are titanium at one end and steel at the other. In this case we join similar metals (titanium to titanium and steel to steel) by the fusion welding method. According to the other technology, joining is performed using one (vanadium) or several intermediate metal inserts which are successively fusion welded to each other [1].

Electron beam welding. The technology for EBW of titanium alloy OT4-1 to steels of the VNS2, 12Kh18N12T and EP56 grades, ferritic chromium steels and iron is considered in studies [8–12]. Welding was performed using an insert of vanadium alloy VV8. Strong and sufficiently ductile welds between vanadium and steel were made by welding with a beam shifted towards steel to a distance of 1.1–1.3 mm from the joint. In welding alloy OT4-1 to vanadium the beam was shifted towards titanium to a distance of 0.5 mm from the joint. Welding was carried out at speed v = 45 m/h and accelerating voltage U = = 20 kV. The focusing current was I_f = 118 μA, and the beam current was 59 and 63 μA for the VV8 + VNS2 and VNS2 + OT4-1 welds, respectively. In welding under the above conditions the weight content of vanadium in the VV8 + VNS2 weld was not in excess of 15 %, while the main structural component of the weld metal was a lamellar ferrite alloyed with vanadium [11]. The weld metal with such a structure was characterised by a relatively high ductility, while strength of the welded joint was not inferior to that of the VV8 alloy. Similar results were obtained in welding titanium to steels of the 12Kh18N12T and EP56 grades.

In welding titanium to iron, low-carbon or ferritic chromium steel the weld metal should be additionally alloyed with 2–16 wt.% nickel, depending upon the concentration of carbon in the weld metal. This alloying provides tough fracture of the welds containing up to 0.06 wt.% carbon. At its higher concentration (independently of the nickel content) a brittle fracture was fixed in the vanadium–weld fusion zone [8].

Argon-arc tungsten-electrode welding. The main problem in arc welding of titanium to steel using a vanadium alloy intermediate insert is similar to that faced in EBW. It is necessary to produce welds of a certain chemical composition [12]. In the steel-vanadium weld the mass fraction of vanadium should not be higher than 15 %, whereas in the titanium-vanadium weld it should be not in excess of 25–30 %, which provides a thermally stable single-phase β-structure. To do that, welding of both welds was carried out by shifting the electrode to 0.8–1.0 mm relative to the joint. The welding speed should be not less than 30 m/h. It should be noted that welded joints between titanium and steel produced through the vanadium insert can have a reliable performance at increased temperatures within a range of 200–300 °C [13] and in aggressive environments [14]. At higher temperatures (500–600 °C) the joints rapidly lose ductility due to precipitation of the σ-phase and formation of vanadium carbides [8, 13].

Solid-liquid state joining of titanium to steel. The feasibility of producing joints between titanium and steel without intermediate inserts was formulated and experimentally proved in studies [15–23]. The joint in this case is formed using projection resistance welding with a programmed final internal splashing and subsequent forging of the joining zone.

As follows from [16], in projection resistance welding the joint is formed first in a liquid phase as a result of melting of billets under the effect of heat released in the weld zone as the current flows through it, and then, after splashing and forging, in the solid-liquid phase. The liquid to solid phase ratio may vary depending upon physical-mechanical properties of the materials joined and welding parameters (current, shape of projections, compression force). In the case of welding titanium to steel, it is desirable that the maximum possible amount of liquid metal of the nugget be removed from the welding zone as a result of splashing and forging, and that the joint be formed primarily in the solid phase. Studies described in [17] resulted in the formulation of necessary premises for formation of such joints between titanium and steel, identification of requirements to the projection shape in titanium and steel parts, shape of electrodes and welding conditions, development of a mathematical model to calculate temperature-time processes [19], and elaboration of a corresponding equipment for practical application of this technology.

It was experimentally established in welding steels 10 mm thick of the St.3, 12Kh13 and 10Kh18N10T grades to titanium alloys 2 mm thick of the VT1-0, OT4-1, VT5-1 and VT20 grades that (other conditions being equal) rupture strength of the weld nugget and fracture energy in impact bending decreased with an increase in alloying of steel [18]. All the joints had a diffusion interlayer 1–8 μm thick in the transition zone. Thickness of the interlayer being the same, strength of the nugget depends upon its chemical composition and contact surface area. Aluminium which gets into the weld from a titanium alloy decreases its strength in all the cases. Chromium, and to a greater degree chromium plus nickel, leads to some increase in strength properties (see the Table). Welded joints usually fracture because of a brittle cleavage. The centre of initiation of microcracks is as a rule a channel where the internal splash occurs, and fracture is accompanied by a partial tear out of the subsurface titanium layers.

Steel grade	*Titanium grade*	*Rupture force, kN*	*Fracture energy in bending, J*	*Bend angle, deg*
St.3	VT1-0	4.0	20.0*	60
	OT4-1	2.8	2.7	11
	VT5-1	2.7	2.7	10
	VT20	2.6	1.5	8
12Kh13	VT1-0	4.2	20.0*	60
	OT4-1	3.6	7.5	26
	VT5-1	3.2	–	–
	VT20	3.1	–	–
10Kh18N10T	VT1-0	5.9	20.0*	60
	OT4-1	4.9	20.0*	60
	VT5-1	4.7	13.1	35
	VT20	3.5	6.9	24

*Specimens did not fracture.

Therefore, performance of the titanium to steel welded joints made by projection resistance welding depends upon the chemical composition of the joining zone, as well as upon the shape and amount of remains of the cast nugget, i.e. upon the factors which are determined by completeness of splashing and character of physical-chemical processes occurring at the titanium–steel interface. This technological process and equipment for its realisation [22] are designed primarily for lining steel tanks with titanium plates.

As shown by the literature analysis, fusion welding of titanium to steel is feasible only in the case of using intermediate barrier layers. Such joints are characterised by satisfactory mechanical properties. However, they have low corrosion resistance and are insufficiently reliable in operation, especially at increased temperatures.

As far as joining titanium to steel in a solid-liquid state is concerned, this method has a very limited application so far.

1. (1979) *Metallurgy and technology of welding titanium and its alloys*. Ed. by S.M. Gurevich. Kyiv: Naukova Dumka.

2. Metzeg, G., Lison, R. (1976) Electron beam welding of dissimilar metals. *Welding J.*, **8**, 230–240.
3. Rykalin, N.N., Shorshorov, M.Kh., Krasulin, Yu.L. (1965) Physical and chemical problems of dissimilar metal joining. *Izv. AN SSSR, Series Inorganic Materials*, **1**, 29–36.
4. Gurevich, S.M., Zamkov, V.N. (1962) Welding titanium to steel. *Avtomatich. Svarka*, **8**, 21–26.
5. Rabkin, D.M., Ryabov, V.R., Gurevich, S.M. (1975) *Welding of dissimilar metals*. Kyiv: Tekhnika.
6. Ryabov, V.R., Rabkin, D.M., Kurochko, R.S. et al. (1984) *Welding of dissimilar metals and alloys*. Moscow: Mashinostroenie.
7. Larikov, L.N., Ryabov, V.R., Falchenko, V.M. (1975) *Diffusion processes in solid phase during welding*. Moscow: Mashinostroenie.
8. Gonserovsky, F.G. (1972) Influence of carbon on impact toughness of welded joints between vanadium and iron and ferritic steels. *Svarochn. Proizvodstvo*, **11**, 7–8.
9. Gonserovsky, F.G. (1972) Influence of alloying elements on impact toughness of welded joints between vanadium and stainless steel. *Avtomatich. Svarka*, **10**, 17–20.
10. Petrenko, V.R., Ryzhkov, F.N., Bashkatov, A.V. et al. (1974) Electron-beam welding of 0T4-1 titanium alloy to VNS-2 steel. *Svarochn. Proizvodstvo*, **10**, 19–20.
11. Gonserovsky, F.G. (1972) Peculiarities of production of vanadium-steel welded joints. *Ibid.*, **12**, 10–12.
12. Strizhevskaya, L.G., Starova, L.L., Kulikov, F.R. (1973) *Weldability and properties of welded joints between titanium and steel made using vanadium alloy. Lectures on welding of dissimilar metals*. Moscow: Znanie.
13. Strizhevskaya, L.G., Kulikov, F.R., Kurochko, R.S. (1983) High service life welded joints between titanium and steel. In: *Proc. of 8th All-Union Meeting on Welding of Dissimilar, Composite and Multilayer Materials*. Kyiv: PWI.
14. Gurevich, S.M., Kulikov, F.R., Druzhinina, I.P. (1983) Corrosion resistance of welded joints of titanium to steel. *Ibid.*
15. Bykovsky, O.G. (1984) Cladding of chemical production steel apparatuses with titanium. *Svarochn. Proizvodstvo*, **11**, 34–35.
16. Bykovsky, O.G., Pinkovsky, I.V., Minyajlo, S.N. et al. (1988) On the role of metal splashing in projection welding of titanium to steel. *Ibid.*, **7**, 4–5.
17. Bykovsky, O.G., Pinkovsky, I.V., Minyajlo, S.N. et al. (1988) Selection of parameters for projection welding of titanium to steel. *Avtomatich. Svarka*, **11**, 61–64.
18. Bykovsky, O.G., Pinkovsky, I.V., Minyajlo, S.N. et al. (1988) Influence of source materials on formation and properties of spot welded joints in titanium to steels and nickel. *Svarochn. Proizvodstvo*, **11**, 15–17.
19. Bykovsky, O.G., Gorbunov, A.D. (1990) Mathematical modelling of metal thermal state in resistance spot welding. *Ibid.*, **7**, 36–38.
20. Bykovsky, O.G., Pinkovsky, I.V., Ryabov, V.R. (1989) Fractographic examination of failure of titanium-steel welded joints. *Avtomatich. Svarka*, **8**, 5–8.
21. Pinkovsky, I.V., Bykovsky, O.G., Tkachenko, I.V. et al. (1987) Peculiarities of resistance welding of VT1-0 titanium to low-alloy steel. *Svarochn. Proizvodstvo*, **5**, 11–12.
22. Bykovsky, O.G., Pinkovsky, I.V., Minyajlo, S.N. et al. (1988) In site projection spot welding of titanium to steel. *Ibid.*, **12**, 4–5.
23. Ryabov, V.R., Bykovsky, O.G., Samojlov, V.E. et al. (1989) Wettability of titanium and steel with Ti–Fe system alloys in fusion welding. *Avtomatich. Svarka*, **11**, 10–13.

INTEGRATED MECHANISATION AND AUTOMATION OF MANUFACTURE OF WELDED HOPPER CARS

B.G. TSYGAN[1], **L.I. PIROGOV**[1], **A.V. DONCHENKO**[2] and **Yu.A. TRUBACHEV**[2]
[1]Kremenchug State Polytechnic University, Kremenchug, Ukraine
[2]Ukrainian State Research Institute of Car-Building, Kremenchug, Ukraine

The paper deals with advanced technological processes to manufacture welded metal structures of hopper cars, as well as process equipment, used for their implementation. Mechanisation and automation of the most labour-consuming operations allows a significant improvement of labour efficiency and reduction of the costs, which are related to manufacture of the cars. The described designs of process equipment may be widely used in many mechanical engineering plants during performance of assembly-welding operations.

Key words: *mechanisation, automation, welding, car-construction, technological process, processing equipment*

Cars with a hopper-shaped body (hoppers cars) are successfully operated in the railways of many countries of the world. They are used for bulk shipment of cargo, of which there are about 600 kinds. The cars can be of two types: roofed (for shipment of bulky cargo, requiring protection from atmospheric impact) and open (for the other kinds of cargo, namely coal, iron pellets, etc.).

Hopper cars, produced in Ukraine for transportation of cement, mineral fertilisers, peat, iron pellets, etc., are superior to their analogs from Russia, Germany, France and other countries by their most important parameters (empty weight-to-carrying capacity ratio, volume and weight of the transported cargo). Practically all the hopper cars have a standard all-welded metal structure of the body. On the other hand, they differ from each other by the design and number of hoppers, loading and unloading hatches, position of the latter relative to the track and unloading mechanisms. The highest level of mechanisation and automation of assembly-welding operations in manufacture of hopper cars in Ukraine was achieved in Company «Stakhanov Car-Building Works». An eight-wheel roofed self-dumping car (Figure 1) currently made in the Works is designed for shipment over the entire railway network of CIS countries (1520 mm tracks) of bulky granulated, coarse-grained, crystalline, non-caking non-corrosive mineral fertilisers, as well as bulky powderlike raw materials (apatite concentrate, phosphoric powder).

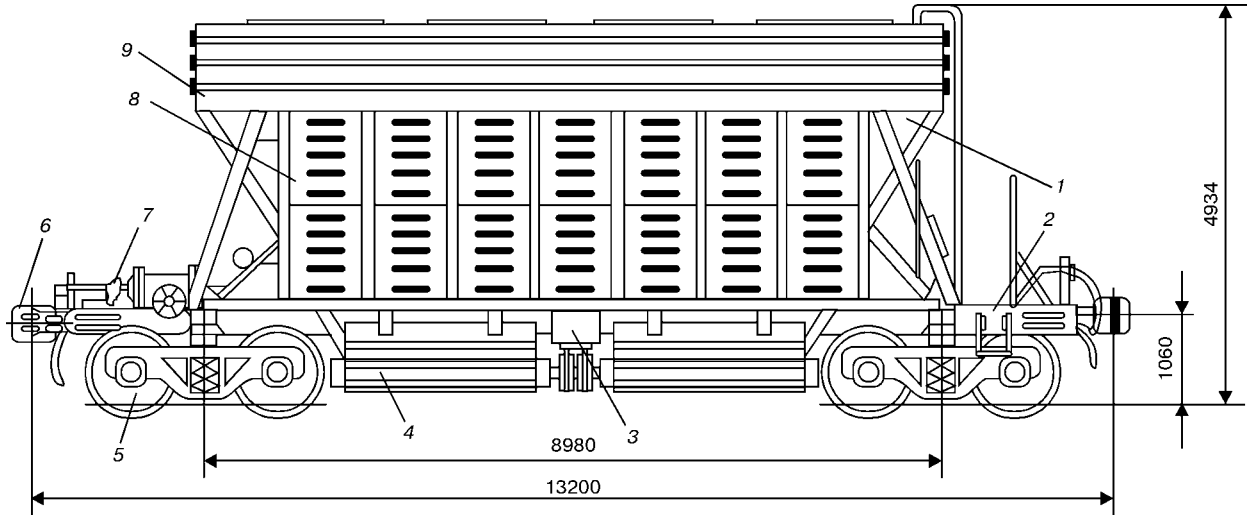

Figure 1. Hopper car for mineral fertilizers (19-923 model): *1* — body with hoppers; *2* — frame; *3* — dumping mechanism; *4* — unloading hatch covers; *5* — undercarriage; *6* — automatic coupling; *7* — automatic brake; *8* — side wall; *9* — roof with loading hatches

The carriage is an all-welded structure. Cargo is loaded through hatches, located in the roof. They are fitted with covers, providing a reliable locking and sealing to prevent moisture penetration inside the car. Located in the lower part of the body on both sides of the hopper are two slot unloading hatches, which are opened and closed by a pneumatically driven mechanism.

In order to set up the production of this car, the design-technology institutes developed technologies, which envisaged the use of the most advanced processing equipment and rigging, integrated flow lines with a rigid and soft constraint, object-closed shops and sections. Production runs in a closed cycle, unit welding and general assembly of the car are located in two bays of the assembly-welding shop. The main principle of the shop lay-out is provision of a direct-flow production process of making the frame, hoppers, roof, side and end walls and body.

The basic element of the car is the frame (Figure 2). It consists of main beam *1*, two bolster beams *4*, longitudinal *2* and transverse *5* ridges, lower *7* and front *6* sheets, lever bracket *3* and step bracket *8*. Technological process of frame assembly starts with manufacture of main beam, which is made of two beams of Z-section No.31, welded to each other by a longitudinal butt weld. Front rests of automatic coupling are mounted on end parts of the beam. A ridge

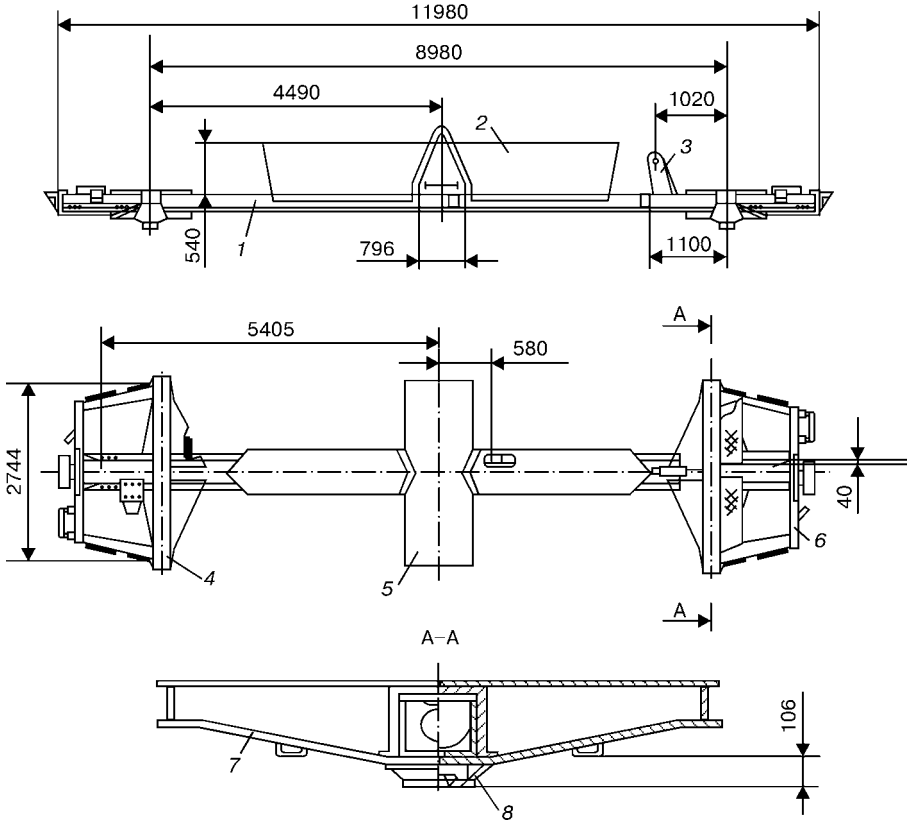

Figure 2. Frame of a car for mineral transportation (for designations see the text)

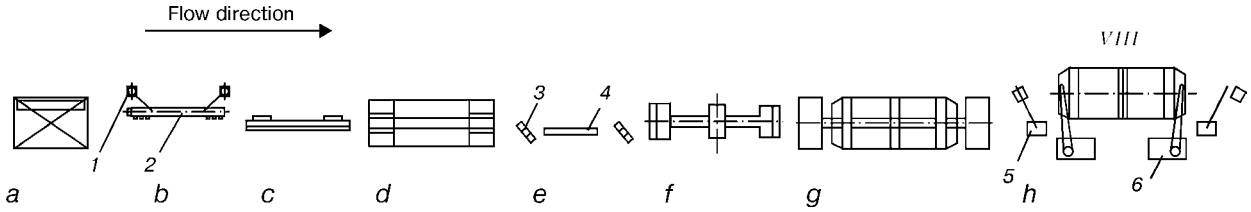

Figure 3. Schematic of a section for assembly and welding of frames of a car for mineral transportation: *a* — container for Z-section; *b* — bench for main beam assembly; *c* — automatic welding machine; *d* — two-sided drilling machine; *e* — tilting carriage for rest riveting; *f* — bench for frame assembly; *g* — trunnion welding positioner; *h* — bench for drilling and riveting the step brackets (for other designations see the text)

is welded on top, giving it additional strength and promoting better pouring off of the cargo. Assembly and welding of main beam are arranged in a specialised bay (Figure 3).

Z-sections are transported to the shop in containers (Figure 3, *a*), from where they are transferred piece by piece to the facility for their cutting to the required length, and then are placed into assembly bench *2* using pneumatic manipulators *1* (Figure 3, *b*). Automatic welding of a butt weld of the main beam is performed with two automatic welding machines A-1412 on a flux-copper pad (Figure 3, *c*). In order to achieve sound formation of the bead, the gaps formed in assembly, are filled with granulated metal fillers of Sv-08G2S (wt.%: 0.1C; 1.0Mn; 0.4Si; Fe — balance) wire of 2 mm diameter. In order to reduce the distortion, the beam is welded with application of its elastic out-of-plane bending with subsequent fastening and use of back-step technique, i.e. one automatic machine applies a weld from the beam beginning up to its middle and the second from beam middle to its end.

Final assembly of the unit, intermediate control, repair of defective sections of the weld and item acceptance by quality inspection personnel are performed in a welding positioner (Figure 3, *g*). Assembled (with front and rear rests) main beam is moved to a multihead two-sided drilling machine AM 15-411 (Figure 3, *d*). It is then laid on tilting carriage *4* (Figure 3, *e*), where riveting operation is performed by hydraulic rotating clamps *3*. Rivets are heated in an electric furnace, which provides a fast (during 20–25 min) heating of 20 rivets of 27–30 mm diameter up to the temperature of 850–900 °C, prevention of their overheating or formation of scale. Silicon carbide electrodes are used as heating elements, to which voltage is applied from welding current source TDF-1200.

Then the main beam is moved on and placed into a bench for assembly (Figure 3, *f*) with the elements of bolster beam, ridges (longitudinal and transverse) and other parts of the frame. All the assembled elements are tack welded to each other and the assembled unit is fastened in the welding positioner (Figure 3, *g*). Welded frame is mounted by bridge cranes in the drilling bench (Figure 3, *h*) to make holes by radial drilling machines *6* and subsequent riveting of pivots to it by suspended hydraulic clamps *5*. The frame is then assembled with pre-fabricated hoppers and is welded in the tilter with lifting centres. The finished item accepted by quality inspection department is transported by the transfer car to the bench for general assembly of the car body.

Side wall of the car for mineral transportation (Figure 4) is a frame structure, consisting of lower *1* and upper *2* ties, connected by vertical posts *3*. Braces *6* are mounted at the extreme posts to make the frame more rigid. Upper tie is made of formed channel section of open type, lower tie and braces of a square pipe 5 mm thick. Posts are made of double T-shape No.12. Sheathing *4* is made of channelled sheets 3 mm thick with intermittent corrugations. Sheathing is welded to posts by plug lap joints of 21 mm diameter with 110 mm spacing, and to upper and lower ties by

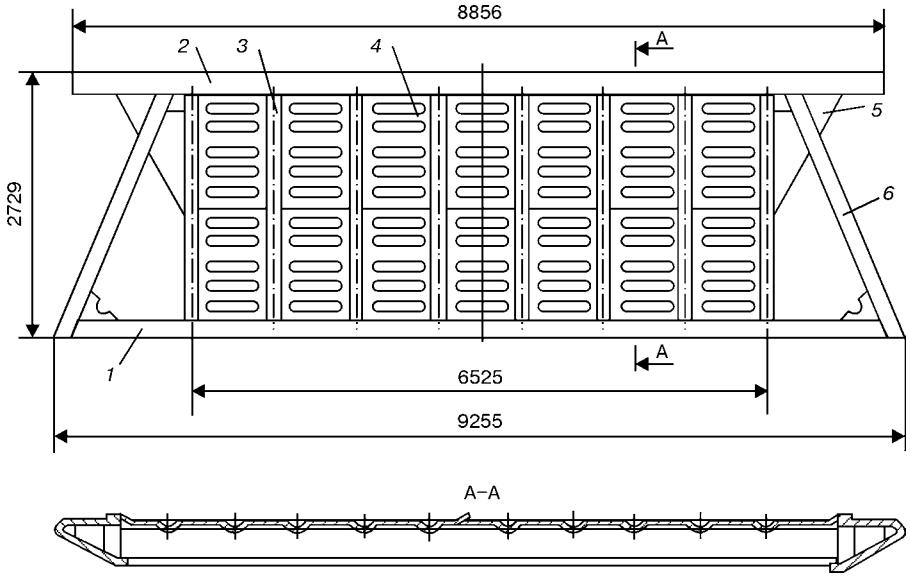

Figure 4. General view of the car for mineral transportation: *1* — lower tie; *2* — upper tie; *3* — post; *4* — sheathing sheet; *5* — end sheet; *6* — brace

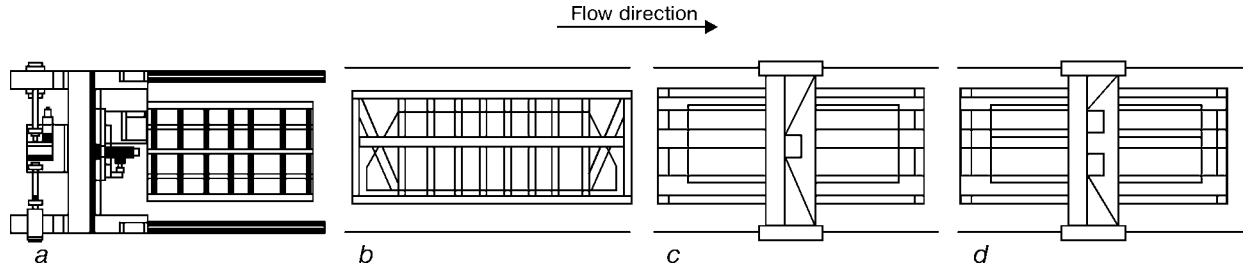

Figure 5. Schematic of a flow line for assembly and welding of the side wall of a car for mineral transportation: *a* — set up for sheathing panel assembly and welding; *b* — bench for assembly of the side wall with the panel; *c* — machine for ASW of the panel to the frame; *d* — machine for automatic welding of the panel to the ties

an overlap weld. Upper and lower ties, posts and knee braces are made of 09G2D steel, side wall boards of 10KhNDP (wt.%: 0.1C; 0.5Cr; 0.8Ni; 0.2Si; 0.3Cu; Fe — balance) or 09G2D (wt.%: 0.1C; 1.0Mn; 0.4Si; 0.3Cu; Fe — balance).

Side walls are manufactured in an integrated flow line, consisting of four work places and manufacture starts with assembly and welding of the sheathing panel in a specialised installation (Figure 5, *a*). Sheathing panel consists of two corrugated sheets, which form an overlap joint, welded from both sides by a fillet weld with 3 mm fillet. The sheets are laid with bridge crane into the bench by the rests and are fastened by side collets. A welding gantry is brought to the point of the start of welding at travel speed, and automatic CO_2 welding of the panel is performed with 2 mm wire at the speed of 80 m/h. Gaps in the overlap joint are prevented by pressing together the edges to be welded by a press-down roller, mounted on the gantry.

After the first weld has been made, the item is released, is tilted through 180° in the same work place by a bridge crane, and the second weld is made. The finished item is raised by a lifting roller conveyor, built into the bench frame, and is transferred to the bench for assembly with the side wall frame (Figure 5, *b*). Stay posts, upper and lower ties and sheathing sheets are laid by the rests on the panel, which has come to the bench for assembly. All the parts are connected to each other by electric arc tack welds, and the assembled unit is transferred by the roller conveyor to the machine for automatic arc spot welding (ASW) of the sheathing panel with the posts of the side wall frame (Figure 5, *c*).

The installation, shown in Figure 6, consists of bed *5*, gantry *3*, carrying A-1731 U4 machine *2* for twin-arc spot welding, rail track *4*, trestle *6* and stair platform *1*. The bed for the item is made in the form of a frame with supports, rests and pneumatic clamps. Platform *1*, used for inspection and maintenance of the gantry, is mounted at the end face of the bed. Gantry moves along the rail track, with limit switches placed along it to adjust the spot weld spacing. At the start of operation the gantry is brought into a position, providing free access to the bed. Bed grips and collets are opened. The position of the assembled side wall, coming in by the roller conveyor, is fixed by catches and fastened with pneumatic clamps against the rests. Then the gantry is brought at the travel speed of 6.6 m/h to the place of welding the first row of the arc spot weld, and the automatic welding machine is switched on, which during 5 s performs simultaneous CO_2 welding of two plug lap joints of 19 mm diameter with automatic welding up of the crater. After that the welding head is lifted by a pneumatic cylinder and the automatic machine moves along the guide rail, which carries microswitches, controlling the size of the step of the automatic machine displacement. Then the head is lowered and the next two plug lap joints are welded, etc. The spot weld is made at the working speed of 3.54 m/min. After completion of welding of the first

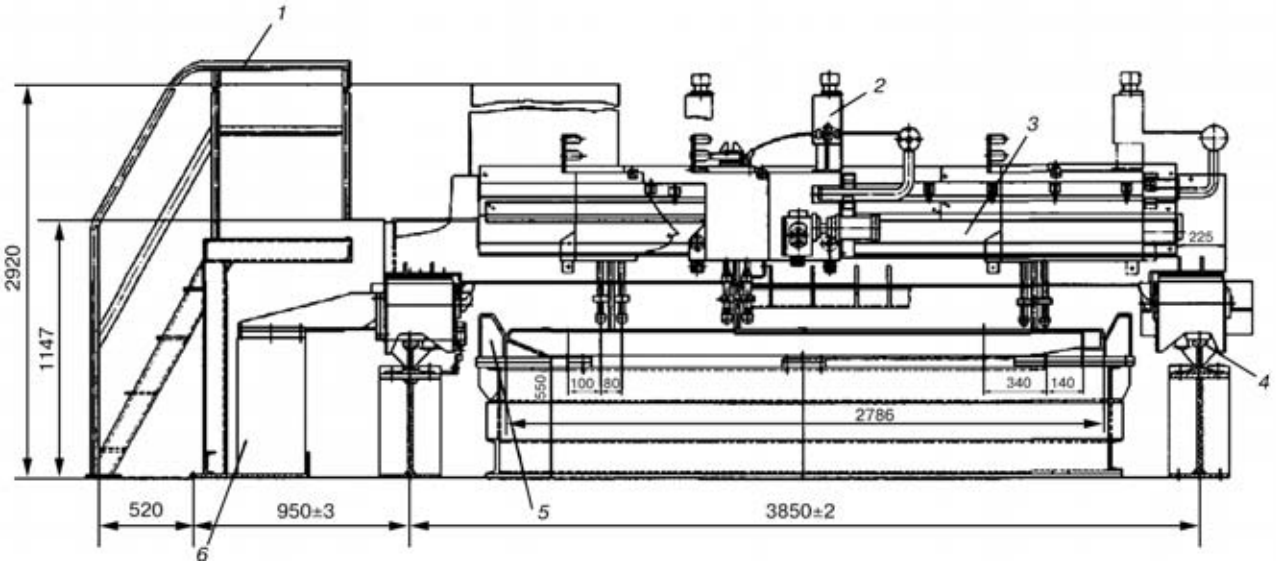

Figure 6. Installation for automatic ASW of the sheathing panel to the side wall frame (for designations see the text)

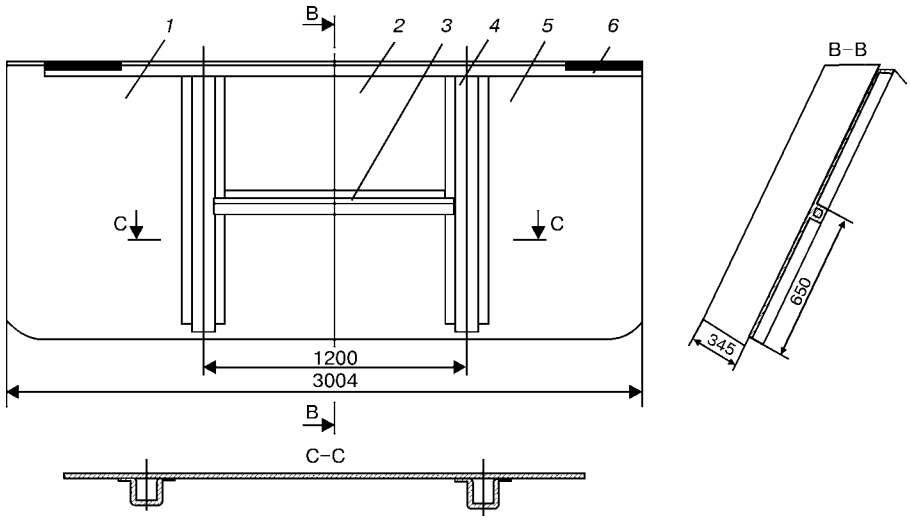

Figure 7. End wall of the car for mineral transportation (for designations see the text)

spot weld, the gantry in the automatic mode is moved to the next row, etc., up to completion of the technological operation. Then the item is released, tilted by the gantry crane through 180° and is transferred to the machine for welding the sheathing panel to the upper and lower ties (Figure 5, *d*). The machine allows automatic welding to be performed simultaneously with two welding heads, providing a close fitting of the edge of the panel being welded to the ties, and automatic guiding of the electrode along the butt axis. Welded side wall is transferred to the bench for general assembly of the car body.

The end wall of the car for mineral transportation (Figure 7) consists of three parts, namely sheathing sheet *2* and two extruded 4 mm sheets *1* and *5*, butt welded to it. Extruded parts are used to improve the sliding of the cargo and provide a bond in the form of butt joints between the side and end walls. Upper tie, made in the form of strip *6*, is welded to the upper part of the sheathing. Sheathing sheet is reinforced with two longitudinal posts *4* and girth *3* of omega-shaped profile. Production of end walls is organized in a specialized shop section, consisting of three work places.

Manufacture of the unit starts from assembly and automatic welding of two extruded and one middle sheet to each other with back weld formation in the installation (Figure 8), consisting of bench *5*, gantry *10*, moving along guide rails *9* and welding tractor *13*. Attached to base of bench *19* are two copper backings *4* and *8* with hinge rests *3* and *7*, pneumatic clamps *20* and specialized mechanized rammers *21* for bringing the edges of abutted sheets in contact with curvilinear edges. The gantry is used for displacement of the welding tractor into the welding zone and reliable pressing up of the butts being welded to the copper backing.

The sheets were placed into the bench by hinge rests *3* and *7*, so that the edges being welded were located above the copper gaskets with 5 mm gap, and were fastened by pneumatic clamps *20*. After that the gantry is moved into the welding zone and pneumatic centralisers are used to mount it with respect to rest *6*. The gap between the edges of the sheets being welded is filled with flux for sound formation of the back side of the weld. Then rammer *21* is used to press together the edges of the abutted sheets, and one-side automatic butt welding is performed after their fastening by pedal pneumatic clamps *18*.

Welded sheathing is released, and the bridge crane moves it to the position of sheathing assembly with

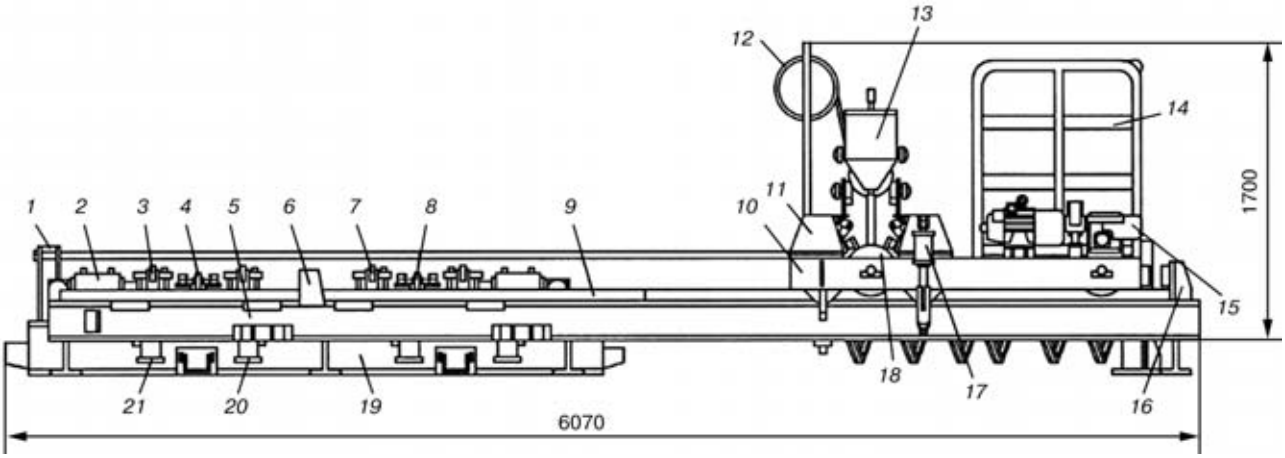

Figure 8. Installation for assembly and automatic welding of end wall sheathing: *1, 16* — rest; *2* — stop pneumatic cylinder; *3, 7* — hinge rests; *4, 8* — copper backing; *5* — bench; *6* — stationary rest; *9* — guide; *10* — gantry; *11* — pressure beam; *12* — power supply; *13* — welding machine; *14* — welder platform; *15* — electric drive; *17* — pneumatic centraliser; *18* — pedal pneumatic clamps; *19* — base; *20* — pneumatic clamp; *21* — rammer

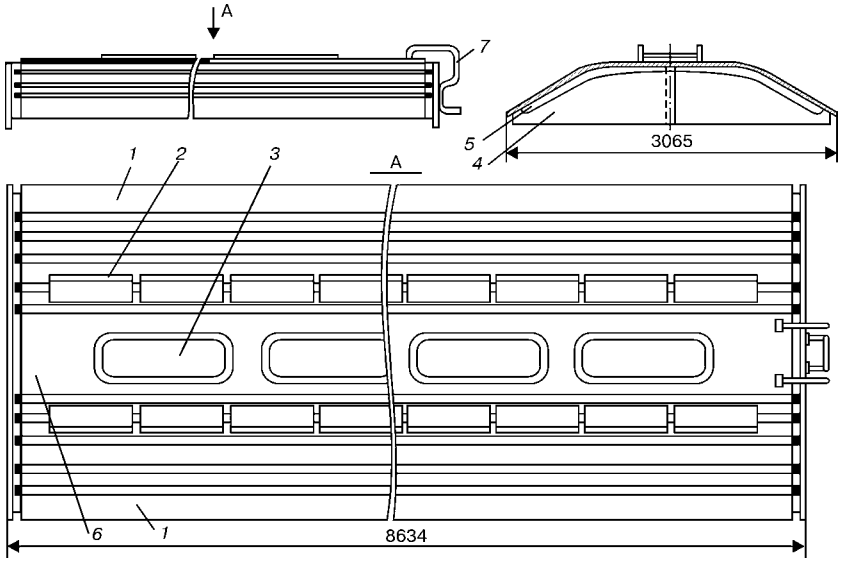

Figure 9. Roof of the car for mineral transportation: *1* — end sheet; *2* — roofing; *3* — loading hatch cover; *4* — transom; *5* — arc; *6* — middle sheet; *7* — hand rail

other elements. The assembled unit is placed on the manipulator table, where it is welded. Finished item is submitted to the staff of quality inspection department and is transferred to the general assembly of the car body.

Figure 9 shows the design of the roof of the car for mineral transportation. It is made in a closed integrally mechanized section, including three processing operations and one storage position. Roof sheets are initially laid out by the form of the panel, are tack welded to each other, and are placed in the as-assembled form into the bench, where automatic CO_2 welding of two overlap welds is performed simultaneously. Welded panel is laid onto arcs *5* first mounted and fastened in turner-bench.

The highest level of labour mechanisation and fitting of the technological process with equipment in manufacture of roofs of hopper-cars, and, in particular, of cement-carrying cars, was achieved in Kryukov Car-Building Works.

The roof of the cement-carrying car (Figure 10) consists of transverse arcs *5*, made of angle bars and covered with sheets *4* and *7* on top. Sheathing panel sheets have longitudinal corrugations, which impart rigidity to the roof and prevent service personnel from slipping on it. Welded to extreme arcs from both end faces of the roof are transoms *9*, used to join the roof to the end walls of the car. Four loading hatches *3* are located along the roof axis, which have covers with a spherical surface and are pressed down by

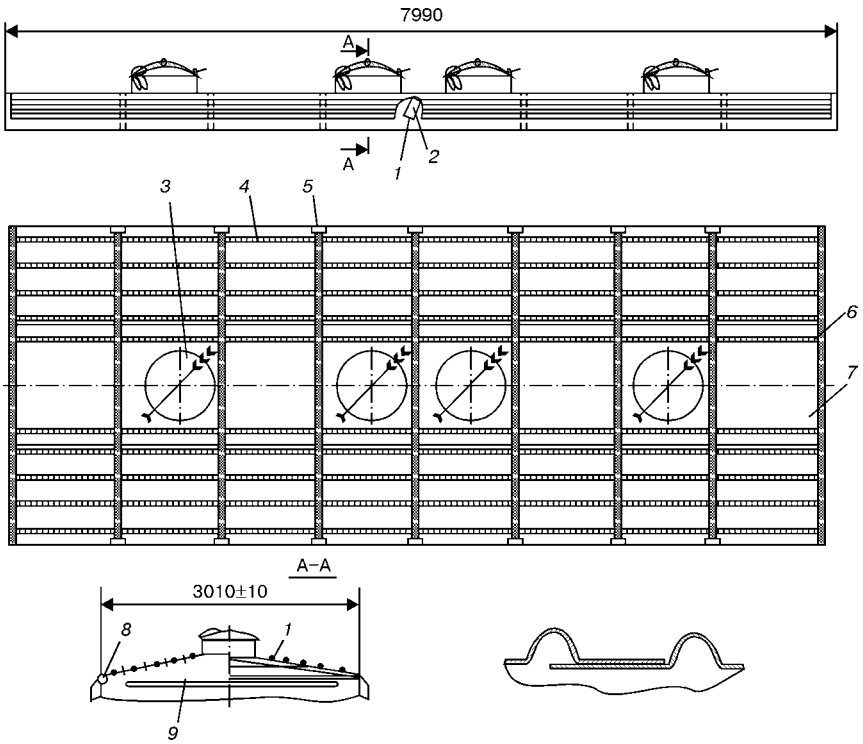

Figure 10. Roof of a cement-carrying car: *1* — compensator; *2* — strut; *3* — loading hatches; *4* — end sheet; *5* — arc; *6, 8* — plug; *7* — middle sheet; *8* — transom

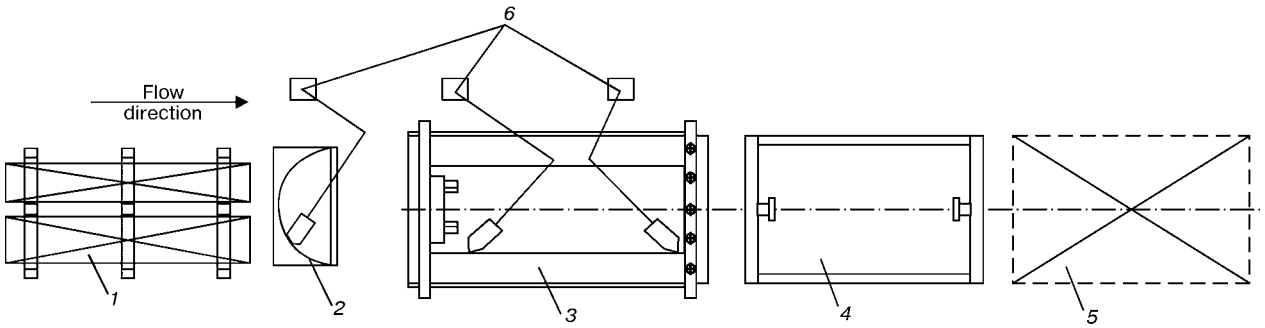

Figure 11. Layout of equipment in the line for roof manufacturing: *1* — storage position for sheet rolled stock; *2* — bench for assembly and welding of transoms; *3* — installation for assembly and welding; *4* — bench for testing welded joints tightness; *5* — storage position for finished items; *6* — two-arc consoles with feed mechanisms of semi-automatic welding machines

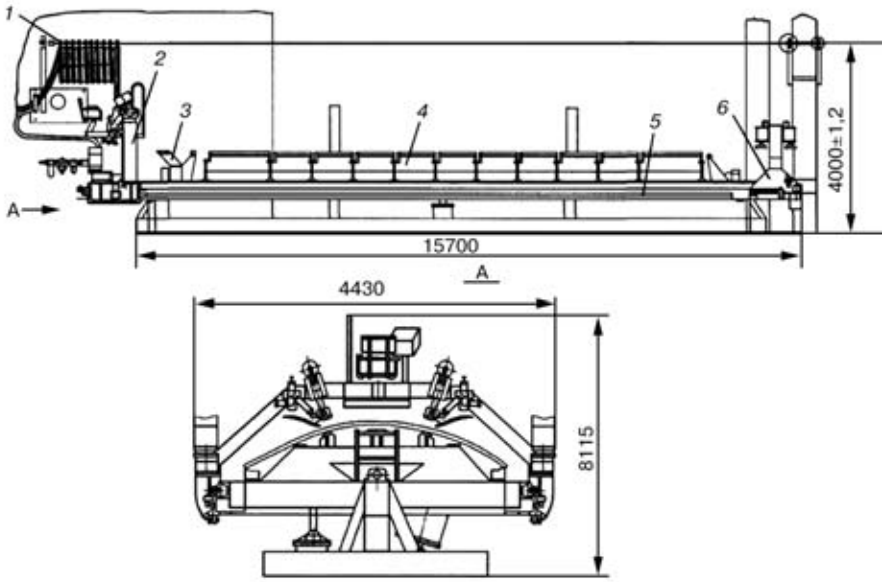

Figure 12. Installation for assembly and automatic welding of roof of the cement-carrying car: *1* — cable suspension; *2* — welding gantry; *3* — bracket; *4* — assembly bench; *5* — guides; *6* — assembly gantry

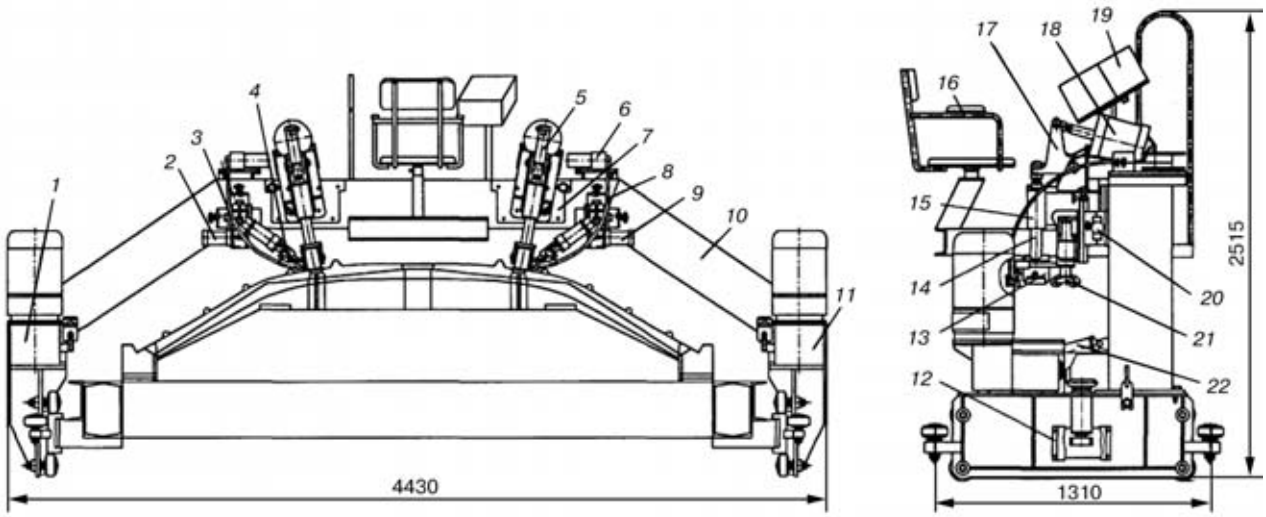

Figure 13. Welding gantry: *1, 11* — carriage; *2, 9* — tracer; *3, 8, 20* — corrector; *4* — welding torch; *5* — pneumatic clamp; *6* — A-1197S semi-automatic machine; *7* — flange; *10* — beam; *12* — casing; *13* — press-down roller; *14* — rod; *15* — bracket; *16* — chair; *17* — lever; *18, 22* — pneumatic cylinder; *19* — control panel; *21* — tracer rollers

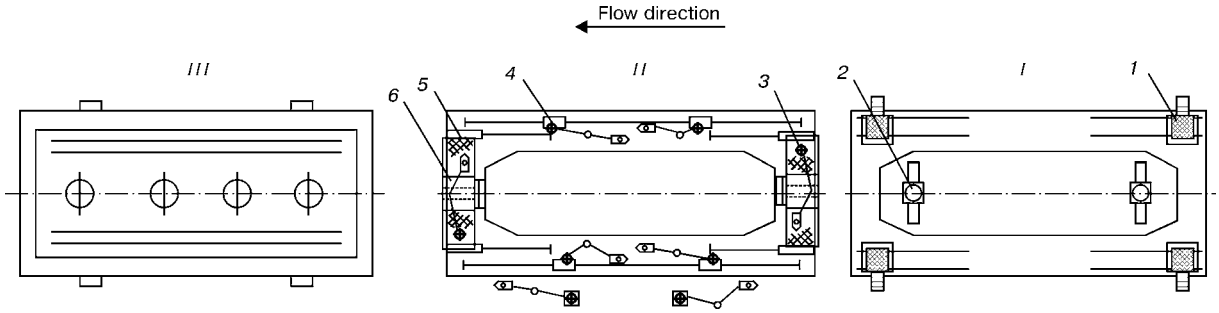

Figure 14. Schematic of equipment layout in the section of assembly of the car metal structure (for designations see the text)

spring-loaded levers. Mounted on the middle arc of the roof is a staircase, which is connected to the vertical sheet of the frame in its lower part. The staircase is designed for servicing the car inner part. Roof manufacturing is organized in a flow line, which consists of two operating positions and two storage positions. Equipment layout in the flow line is shown in Figure 11.

Roof assembly starts with manufacture in jig *2* of arcs and transoms, which are transferred to the assembly bench of installation *3*. Further assembly and automatic welding of the roof of cement-carrying car is performed in the installation (Figure 12), which consists of assembly bench *4*, welding *2* and assembly *6* gantries, and cable suspension *1*. Laid along the bench are longitudinal rack guides *5*, providing for displacement of the welding and assembly gantries. Roof assembly starts with sequential positioning by bench rests of the transoms and arcs, with their position being fixed by pneumatic cylinders. After that two end sheets are placed by bridge crane above the arcs, and are tack-welded to them by CO_2 arc process. Then the middle sheet is positioned to form an overlap joint together with the end sheets. Roof sheets are first spot welded to the arcs.

Turning in of the panel sheet and its close contact with the arcs in the points of their welding to it are provided by assembly gantry *6*, fitted with pneumatic clamps. Automatic CO_2 welding of two longitudinal overlap welds is made with Sv-08G2S wire of 1.2 mm diameter, using a gantry, which carries feed mechanisms of semi-automatic welding machines A-1197S. Welding gantry (Figure 13) provides a reliable pressing of edges of the sheets, joined by overlap welds. It consists of two carriages *1* and *11*, beam *10*, clamps *5*, tracers *2* and *9*, torch position correctors *3* and *8*, welder's chair *16* and control panel *19*. Carriages *1* and *11* move the gantry along the guides at welding and travel speed. Synchronous operation of carriage drives is provided by the control circuit. Connecting beam *10* is a box-shaped weldment, which carries the main assemblies of the gantry.

Minimal gaps in welding of an overlap joint of sheathing sheets are provided by using pneumatic clamps *5*, which have angular, transverse and height correction. Electrode guidance along the butt during welding is provided by mechanical tracer *9*, consisting of spring-loaded rollers *21* and welding torches *4*, rigidly coupled to them. Follower rollers with the torch are brought to the butt and withdrawn from it by a pneumatic cylinder. Preliminary positioning of welding torches along the butt axis is performed by correctors *3* and *8*. For operator comfort, chair *16* is mounted on the beam, and panel *19* for control of all the mechanisms of the unit is fastened near it. Finished item is transferred by the crane to the bench for testing the tightness of welded joints *4* (see Figure 11), using the kerosene sample and then to storage position *5*.

The car is an all-welded structure, consisting of a frame with hoppers, two side and two end walls, welded to the frame and to each other, and the roof, welded to the walls. General assembly and welding of the car metal structure is performed in a section, accommodating three working operations (Figure 14), using an electric bridge crane. A frame with hoppers is first placed on the mounting pins of elevating supports *2* of assembly bench (Figure 14, *I*). After straightening in the horizontal plane, which is performed by the method of regulation with measuring plates, the frame is fastened.

Position of side walls relative to the fastened frame is determined by lower catches. Vertical fastening of the side element is performed with a rigging screw. Side and end walls are abutted to each other with screw braces, and edges are aligned, using screw clamps. Work on assembly of the upper part of the car body is performed from carriages *1*, moving along the rails, which are laid along the entire length of the bench. Enclosed elevating platforms for assembly workers are mounted on carriages. Car metal structure assembled with electric arc tack welds is mounted in trunnion positioner (Figure 14, *II*), allowing the item to be rotated through 90° to both sides and the most convenient position for welding operations performance to be selected. Positioner is made in the form of two separate posts. Post *3* is stationary, and post *5* is mobile. Rotary consoles *6* with semi-automatic welding machines are mounted on the post platforms. Laid from both sides of the positioner are rails, along which electrically driven welding consoles *4* move. After welding the body is transferred to the next bench (Figure 14, *III*), where its mounting and welding of the roof to it are performed, and further on to the specialized line of metalwork assembly of the car.

Application of the means of integrated mechanisation and automation in fabrication of welded metal structure of hopper cars allowed Company «Stakhanov Car-Building Works» ensuring a high quality of manufactured items, their operational reliability and improving labour efficiency. In this case, the number of workers was reduced by 10 persons.

In view of the above, we believe it is possible to recommend to engineering-technical staff dealing with the issues of fabrication of various welded metal structures of frame type, beams, sheet panels, etc. to consider the rationality of applying in their enterprises the technology and equipment, introduced in the «Stakhanov Car-Building Works».

METHOD FOR INVESTIGATION OF LONGITUDINAL RESIDUAL STRESSES IN BEAD ON NICKEL ALLOY PLATE WELDING

N.O. CHERVYAKOV and **K.A. YUSHCHENKO**
The E.O. Paton Electric Welding Institute, NASU, Kyiv, Ukraine

It is shown that maximum longitudinal tensile stresses induced in bead on nickel alloy plate welding amount to yield stress of the base metal. In the case of welding with preheating to 900 °C residual stresses decrease by 30 %.

Key words: *high-strength nickel alloys, residual stresses, net method, yield stress, preheating*

Strain-hardening nickel alloys reinforced by the γ-phase are widely applied for manufacture of heavy-loaded components and parts operating at high temperatures. However, these alloys have unsatisfactory weldability, which is attributable to their susceptibility to cracking in fusion welding and postweld heat treatment.

High-temperature preheating has an increasingly wide use as an accompanying operation in the manufacture of gas turbine parts to decrease sensitivity to formation of defects in welding and ensure required properties of welded joints. The role of preheating in cracking of fusion welded joints has been insufficiently studied. The positive effect of preheating is related to relaxation processes occurring during welding and cooling.

It is of practical interest to study the character of distribution of residual welding stresses in welding with preheating and at room temperature.

Experimental mechanical methods based on measurement of displacements caused by removal of clamps from structural members containing residual stresses are most often used to evaluate welding stresses. These methods provide a better measurement accuracy, compared with physical ones based on relationships between residual stresses and some physical properties of materials [1, 2].

Mechanical devices, such as strain gauges and resistive-strain sensors, as well as different types of dividing grids and brittle coatings are employed to measure displacements. Baseline holes are drilled in a plate when using the strain gauges (according to their design). In view of difficulties associated with machining of nickel alloys and peculiarities of their structural state the use was made of the net method [3] to determine residual stresses.

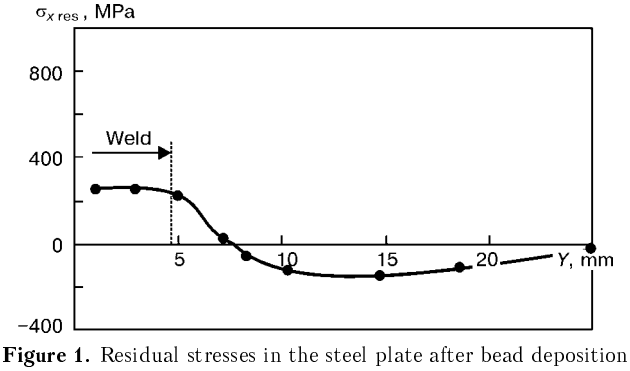

Figure 1. Residual stresses in the steel plate after bead deposition

The point of this method is that a net with assigned parameters is deposited on the material surface. During deformation of a sample the net is distorted, copying distortion of the surface. The value of deformation of an object studied can be estimated by measuring distortion of the net cells and processing the results obtained. The advantages of this method are clearness, credibility and simplicity.

The net of a system of mutually perpendicular lines, the directions of which coincide with directions of the selected coordinate axes, was used for the studies. The net was applied to two sides of the plate using a diamond tool to ensure thickness of the lines equal to 0.01 mm. Prior to bead deposition, the plate surface was polished, and then the net was applied to it, the distance between the lines being 2 mm on the gauge area of 50 mm. The distance between the net lines along axes $0X$ was carefully measured before and after cutting using the toolmaker's microscope BMI-1 with a sample stage moving in longitudinal and transverse directions and with micrometer screws having a scale division of 0.005 mm. The measurement error over the selected gauge area was not more than 10 %. The ×10 magnification was used. The plate was cut using the CNC electrical discharge cutting machine (model 4532F3). Tap water with anticorrosive additives was used as a working fluid.

The procedure for investigation of longitudinal residual stresses was optimised on a plate (140×50×4 mm in size) of high-alloy steel with yield stress of 250 MPa. Automatic TIG welding of a bead on a central part of the plate in the unclamped position was performed under the following conditions: I_w = = 80 A, U_a = 25–26 V and v_w = 4 m/h. After welding with penetration and complete cooling, the plate was cut using the electric discharge cutting machine, which provided minimum induced strains and heating. The cut width was 1–1.5 mm.

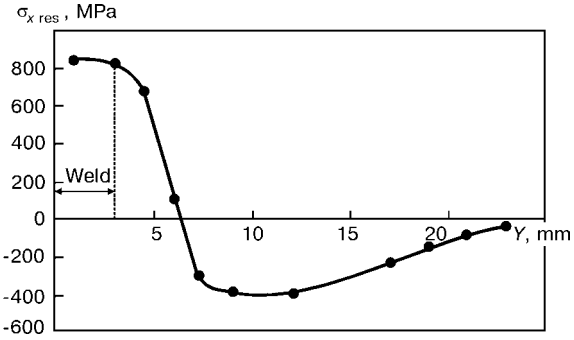

Figure 2. Residual stresses in the nickel alloy plate after bead deposition

Difference between sizes of the net cells before and after cutting the plate yields an elastic component of the strain $\varepsilon = \varepsilon_{el}$. Given that studied were the plates of small width and thickness, the effect of stress σ_y was assumed to be insignificant, and longitudinal residual stresses for a case of the uniaxial stressed state were calculated from formula

$$\sigma_{x\ res} = \varepsilon_x E = \frac{n_1 - n_2}{G} E,$$

where $n_1 - n_2$ is the difference between the net sizes in a longitudinal direction before and after cutting the plate; E is the elasticity modulus of the material; and G is the gauge area.

Maximum tensile stresses which are approximately equal to yield stress of the base metal are formed in the weld and in adjacent regions (Figure 1). These stresses gradually decrease, change the sign and become compressive with transition from the weld to the HAZ.

Residual stresses in the plate of nickel of the Cr–Co–W–Al–Ti alloying system with a yield stress of 850 MPa were determined by the above procedure. TIG welding without a filler on the nickel alloy plate 105×50 mm in size and 3 mm thick was performed under the following conditions: $I_w = 60$ A, $U_a = 10.5$ V and $v_w = 6$ m/h. The maximum tensile stresses reaching the yield stress value are formed in the weld and adjacent regions (Figure 2).

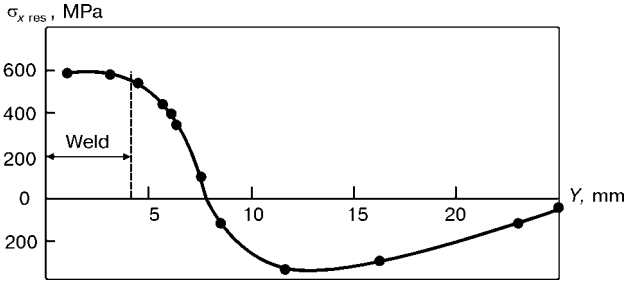

Figure 3. Residual stresses in the nickel alloy plate in welding with preheating

In welding with preheating, the nickel alloy plate of the above sizes was heated in a furnace to a temperature of 900 °C (this temperature favours improvement of ductility characteristics of the alloy investigated), held in the furnace for half an hour, removed and welded. Then the plate was polished and the net was applied to it. After that the plate was cut and stresses were calculated from the formula. Figure 3 shows that the use of preheating results in decrease of 30 % in the level of maximum tensile stresses and extension of the zone affected by them.

CONCLUSIONS

1. Procedure for evaluation of residual stresses in a nickel alloy was optimised using the net method.

2. Maximum tensile stresses induced in TIG welding of a bead on the nickel alloy plate were found to reach yield stress of the base metal. The use of preheating results in decrease of 30 % in longitudinal residual stresses.

1. Nedoseka, A.Ya. (1998) *Principles of calculation and diagnostics of welded structures*. Kyiv: INDPROM.
2. Masubuchi, K. (1980) *Analysis of welded structures: residual stresses, distortion and their consequences*. Pergamon Press.
3. Kasatkin, B.S., Kudrin, A.B., Lobanov, L.M. et al. (1981) *Experimental methods of study of strains and stresses*. Refer. Book. Kyiv: Naukova Dumka.

SOME PECULIARITIES OF DELAYED FRACTURE OF HAZ METAL IN STEEL M76 AFTER CLADDING USING AUSTENITIC WIRE

Ya.P. CHERNYAK, G.V. BURSKY and **V.K. KALENSKY**
The E.O. Paton Electric Welding Institute, NASU, Kyiv, Ukraine

Increase in heat input in cladding samples of steel M76 using wire of the PP-Np-06G13Kh13N2MF type has been found to cause increase in the HAZ metal fracture energy. Accordingly, this leads to increase in resistance of the HAZ metal to cold cracking.

Key words: *cladding, heat-affected zone, heat input, thermal cycles, cold cracks*

Repair cladding of worn out lateral surfaces of steel M76 girder rails using austenitic wire without preheating caused cracks of the cleavage type formed beneath the first deposited bead at the fusion boundary or in the HAZ metal (near this boundary). Formation of these cracks was eliminated by depositing the first bead at an increased heat input [1]. To substantiate the requirement for this peculiarity of the rail cladding technology, it was necessary to quantitatively estimate resistance of the HAZ metal of steel M76 to cold cracking after cladding using austenitic wire at different levels of heat input.

Different test methods are employed to estimate resistance of the HAZ metal to cold cracks (including of the cleavage type). The premise of these methods is that cold cracks initiate and develop with time, i.e. they have the character of delayed fracture on steels subjected to the effect of the welding thermal cycle. The methods include LTP-2, RRC [2], implants [3], etc.

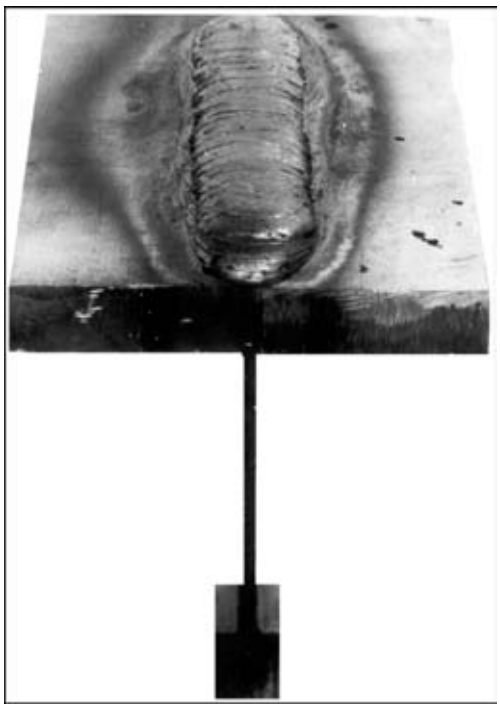

Figure 1. Sample with two deposited beads

The improved implants method [4–7] developed by the E.O. Paton Electric Welding Institute and successfully used in practice was employed to perform the task posed. Investigations were conducted using the system [5, 7] consisting of a loading unit, device for measuring the load on an implant, unit for recording and measurement of displacements in the HAZ metal after application of the external load, unit for registration of acoustic emission (AE) signals, electric signal matching unit and recorder.

Flat polished implants of steel M76 (yield stress $\sigma_y = 610$ MPa) were used. Tabs with rectangular holes to install an implant were made from the same steel. The assembled tabs and implants were placed in the jig to ensure their rigid fixation, then followed cladding on the assembled sample. Cladding was performed by the submerged arc method using flux AN-26P and an experimental flux-cored wire PP-Np-06G13Kh13N2MF at a DCRP. Two beads were successively deposited one upon the other on the sample under different cladding conditions (Figure 1). Chemical compositions of the steel M76 samples and deposited metal are given in Table 1. Thermal cycles were fixed by the KSP-4 recorder using chromel-alumel thermocouples calked into the base metal at a level of the expected fusion boundary.

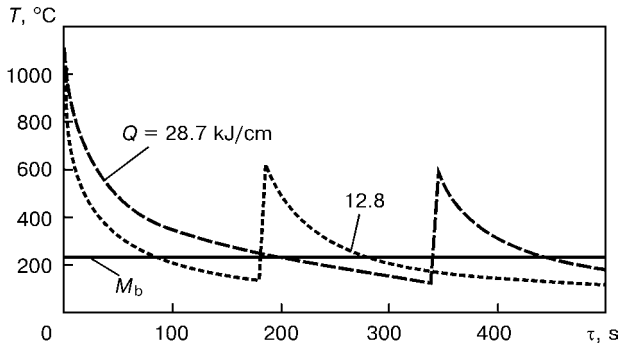

Figure 2. Thermal cladding cycles with different values of heat input

Table 1. Chemical composition of steel M76 and metal deposited with wire PP-Np-06G13Kh13N2MF

Material	Q, kJ/cm	Content of elements, wt.%								
		C	Si	Mn	Cr	Ni	Mo	V	S	P
Steel M76		0.76	0.33	0.80	–	–	–	–	0.021	0.017
Lower bead	12.8	0.453	0.52	9.42	10.34	1.35	0.44	0.26	0.026	0.032
Lower bead	28.7	0.440	0.56	9.38	10.02	1.25	0.37	0.21	0.026	0.030
Upper bead	12.8	0.310	0.64	13.05	13.52	1.71	0.53	0.29	0.028	0.024

Table 2. Effect of cladding parameters on delayed fracture resistance of steel M76 samples

Sample	Bead	v_{cl}^{*}, m/h	Q, kJ/cm	$w_{3/2}$, °C/s	P_{sp}, MPa	$A_{c.i}$, J/m^2	A_{sp}, J/m^2
1	Lower	36.8	12.8	2.5	380	9.1	39.9
	Upper	36.8	12.8	1.4	$(0.62\sigma_y)$		
2	Lower	17.2	28.7	1.2	380	13.7	No fracture
	Upper	36.8	12.8	1.1	$(0.62\sigma_y)$		
3	Lower	17.2	28.7	1.2	537	48.3	112.4
	Upper	36.8	12.8	1.1	$(0.88\sigma_y)$		

*The rest of the cladding parameters were as follows: I = 400–425 A, U = 32 V.

As established in [1], the temperature of beginning of martensitic transformation for steel M76 is M_b = = 230 °C. It is shown that the rate of cooling the steel after cladding should be decreased to ensure a relatively favourable structure of the HAZ metal with a microhardness of about HV 350 (P = 1 kgf, t = 10–15 s). This can be achieved by extending the time to reach the M_b temperature of the HAZ metal to 150–250 s. Based on these data, the lower beads were deposited in two modes. Judging from the recorded thermal cycles (Figure 2), the first mode with heat input Q = 12.8 kJ/cm after cladding provided cooling of the HAZ metal to the M_b temperature within 90 s, and the second (Q = 28.7 kJ/cm) — within 200 s. The upper beads required for the HAZ to be partially tempered were deposited at a low heat input Q = = 12.8 kJ/cm (Figure 2). It was calculated from the following formula:

$$Q = \frac{IU60}{1000 v_{cl}} \text{ kJ/cm},$$

where v_{cl} is the cladding speed, cm/min.

After deposition and cooling in air to 60–70 °C, each sample with a piezotransducer fixed on the implant was loaded into the testing machine and subjected to the permanent effective tensile specific loading P_{sp}. The samples were held under the load to fracture. If they did not fracture, the load was removed after 24 h. The recorder yielded experimental data in the form of delayed fracture curves in the displacement–time coordinates (Figure 3). The curves fix elongation of the samples caused by microplastic deformations and individual AE pulses of an increased amplitude which indicate to an instantaneous release of the elastic energy as a result of formation and growth of microcracks [8]. Table 2 gives systematised experimental parameters and results.

It can be seen from Figure 3 that microcracks in the samples are formed under the effect of loading after different plastic deformation. Specific energy spent for deformation of metal to the moment of crack initiation, $A_{c.i}$, for the samples deposited at a heat input of 12.8 and 28.7 kJ/cm is 9.1 and 13.7 J/m^2, respectively. Low values of $A_{c.i}$ and specific fracture energy A_{sp} (energy spent for microplastic deformation, initiation and growth of microcracks to the moment of the fracture centre formation) are indicative of a low plastic deformability of the HAZ metal. The

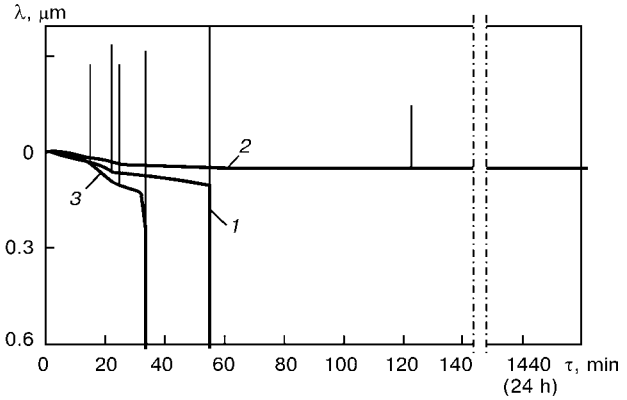

Figure 3. Curves of delayed fracture of samples: *1* — deposition of a lower bead at heat input Q = 12.8 kJ/cm at P_{sp} = 380 MPa; *2* — same at Q = 28.7 kJ/cm and P_{sp} = 380 MPa; *3* — same at Q = 28.7 kJ/cm and P_{sp} = 537 MPa

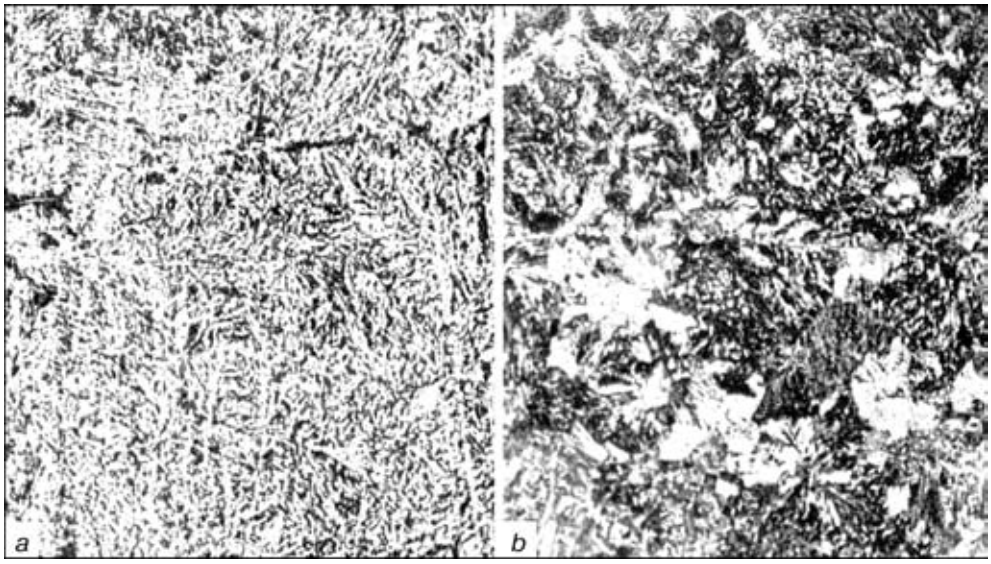

Figure 4. Microstructure of the HAZ metal in cladding using wire PP-Np-06G13Kh13N2MF: *a* — Q = 12.8 kJ/cm; *b* — Q = 28.7 kJ/cm (×500)

rate of cooling the HAZ metal in sample 1 within a range of 300–200 °C ($\omega_{3/2}$) in deposition of the lower bead is 2.5 °C/s. In this case the HAZ metal structure consists of tempered martensite (Figure 4, *a*). Its microhardness amounts to *HV* 408 (P = 1 kgf, t = 10–15 s). Specific energy of fracture of the HAZ metal (under a load of $0.62\sigma_y$) is 39.9 J/m^2. Increase in heat input to 28.7 kJ/cm in deposition of the lower bead leads to decrease (samples 2 and 3) in the cooling rate within a range of 300–200 °C to 1.2 °C/s, and decrease in the maximum microhardness to *HV* 351. A structure consisting of bainite and pearlite is formed in the HAZ metal (Figure 4, *b*). The load equal to $0.62\sigma_y$ turned out to be insufficient to cause fracture of the sample, as microplastic deformations and formation of microcracks resulted in relaxation of stresses. The sample fractured under the load increased to $0.88\sigma_y$, and the fracture energy was 112.4 J/m^2.

Therefore, deposition of the lower bead at a heat input of 28.7 kJ/cm leads to increase of almost 3 times in the fracture energy of the HAZ metal in samples treated using wire PP-Np-06G13Kh13N2MF. This confirms conclusions made in study [1] and suggests that increase in the heat input in deposition of the lower bead leads to a substantial increase in the level of resistance of the steel M76 HAZ metal to cold cracks of the cleavage type.

1. Kalensky, V.K., Chernyak, Ya.P., Vasiliev, V.G. et al. (2001) Heat input influence on formation of tears in high-carbon steel building-up with austenitic wires. *The Paton Welding J.*, **11**, 9–12.
2. Compilation of cold cracking test. *Doc. IIW IX 779–72.*
3. Granjon, H. (1969) The implant method for studying weldability of high strength steel. *Metal Constr. and Brit. Weld. J.*, **11**, 509–515.
4. Sterenbogen, Yu.A. (1986) Some factors determining the HAZ metal resistance of martensitic steels to cold crack formation. *Avtomatich. Svarka*, **6**, 5–8.
5. Bursky, G.V., Savitsky, M.M., Olejnik, O.I. (1999) Improved method of estimation of HAZ metal resistance to delayed fracture. *Ibid.*, **4**, 31–34.
6. Sterenbogen, Yu.A., Bursky, G.V. (1987) Method for estimation of resistance of HAZ metal of high-strength steel welded joints to cold crack formation. *Ibid.*, **3**, 1–5.
7. Sterenbogen, Yu.A., Bursky, G.V. (1990) Estimation of resistance of HAZ metal of medium-alloy high-strength steels to delayed fracture. *Ibid.*, **8**, 33–35.
8. Bartenev, O.A., Kutanov, Yu.I., Khamitov, V.A. et al. (1988) Acoustic emission inspection of laser welded joints. *Ibid.*, **9**, 71–73.